Helena Olivia Karlsen Ramsvik

Tailoring Magneto-Plasmonic Nanoparticles for Biosensing Applications

June 2021

NTNU
Norwegian University of
Science and Technology

Master's thesis

NTNU
Norwegian University of
Science and Technology
Faculty of Natural Sciences
Department of Physics

Master's thesis

Master's thesis
2021

Helena Olivia Karlsen Ramsvik

NTNU
Norwegian University of
Science and Technology

NTNU
Norwegian University of
Science and Technology

Tailoring Magneto-Plasmonic Nanoparticles for Biosensing Applications

Helena Olivia Karlsen Ramsvik

Applied Physics and Mathematics
Submission date: June 2021
Supervisor: Catharina de Lange Davies
Co-supervisor: Sulalit Bandyopadhyay
Katharina Zürbes

Norwegian University of Science and Technology
Department of Physics

Abstract

Today, biosensors are ubiquitous in a wide range of biomedical applications, including clinical diagnostics. Several viruses, including the human immunodeficiency virus (HIV), hepatitis B virus and the measles virus, have already been successfully detected using biosensing technology. The outbreak of coronavirus disease (COVID-19), is an excellent example on how early detection of infection is crucial in preventing the spread of a virus. However, the applications of many of today's biosensors are restricted due to the sensor's level of sensitivity and selectivity to the target molecule, as well as being time-consuming processes. Nanomaterial-based biosensors can be a good alternative in order to overcome these challenges.

Magneto-plasmonic nanoparticles (NPs) are particles composed of one magnetic and one plasmonic material combined together into a single nanoparticle through solid-solid interfaces. Due to their dual nature, these particles exhibit both a local surface plasmon resonance (LSPR) and superparamagnetic behavior.

In this work, anisotropic magneto-plasmonic particles have been synthesized by seed-mediated growth of gold on different iron-containing NPs. By varying the properties of the seed and the reaction conditions of the synthesis, the physico-chemical properties of the resulting particles were tuned to be optimal for use in biosensing applications. It was found that the cetyltrimethylammonium bromide capped iron oxide (IO-CTAB) NP seeds, used in a growth solution with a low silver nitrate content combined with a high pH, resulted in the anisotropic magneto-plasmonic NPs most suitable for biosensing applications.

Graphical Abstract

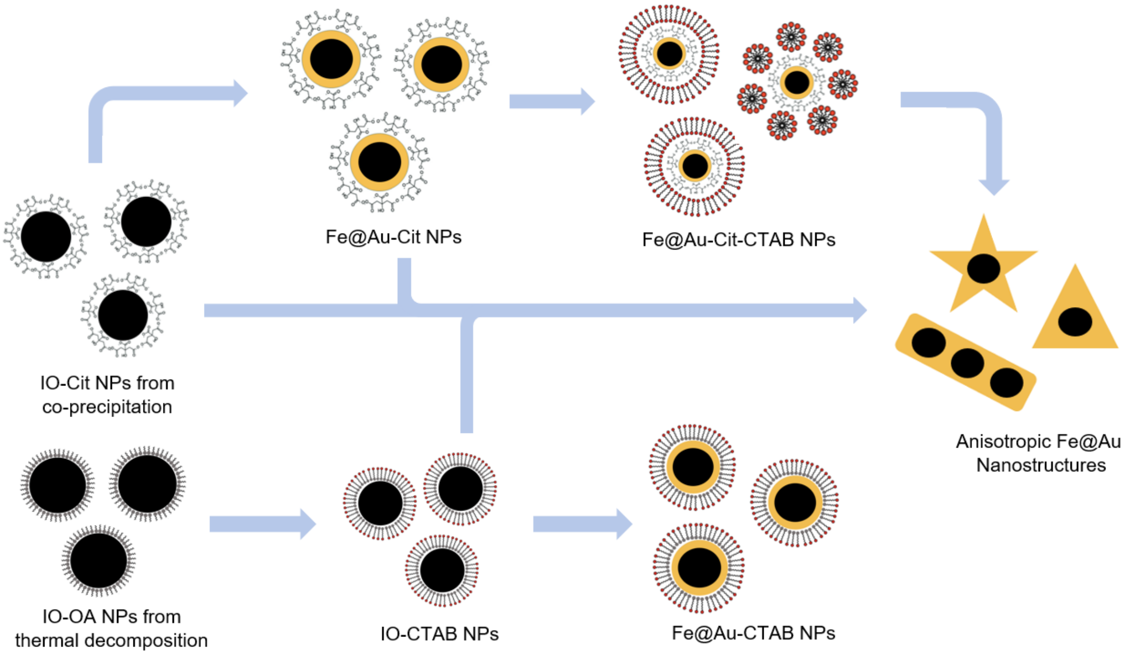

Sammendrag

Biosensorer er i dag uerstattelige verktøy i svært mange biomedisinske felt, inkludert klinisk diagnostikk. Flere virus, som blandt annet humant immunsvikt virus (Hiv), hepatitt B-virus (HBV) og morbillivirus (meslingevirus), kan identifiseres ved bruk av biosensor-teknologi. Utbruddet av koronaviruset (COVID-19) er et utmerket eksempel på hvordan tidlig påvisning av en virusinfeksjon er avgjørende for å forhindre spredning av sykdommen. Dagens biosensorer begrenses av både sensitiviten og selektiviteten på biomolekylet som skal detekteres, i tillegg til at selve deteksjonen ofte er en tidskrevende prosess. Å lage biosensorer ved bruk nanoteknologi, kan bidra til å øke kvaliteten på biosensorer betraktelig.

Magneto-plasmoniske nanopartikler (NP) er partikler bestående av et magnetisk og et plasmonisk materiale fusjonert sammen til én nanopartikkel. Grunnet deres to-delte natur, har disse partiklene både en lokal overflate plasmon resonansfrekvens (LSPR) og superparamagnetisk oppførsel.

I løpet av dette arbeidet har anisotrope magneto-plasmoniske partikler blitt syntetisert gjennom heterogen vekst av gull på forskjellige typer jern-holdige NP kjerner. Ved å variere egenskapene til kjernene og reaksjonsbetingelsene for syntesen, ble egenskapene til de resulterende partiklene justert til å være optimale til bruk i biosensor-teknologi. Det ble funnet at det å bruke cetyltrimetylammoniumbromid dekte jern-oksid (IO-CTAB) NP kjerner, i en vekstløsning med lavt sølvnitratinnhold kombinert med en høy pH, resulterte i de anisotrope magneto-plasmoniske NP som var mest egnet til bruk i biosensing.

Preface

This thesis marks the end of my master's degree in Biophysics and Medical Technology, completed June 2021 at the Norwegian University of Science and Technology, NTNU. It was performed in collaboration with the Department of Chemical Engineering with the Particle Engineering Research Group, under the supervision of Dr. Sulalit Bandyopadhyay. The work was based on results obtained from my specialization project titled "*Synthesis and Functionalization of Heterodimeric Nanoparticles for Biomedical Applications*" that was completed in December 2020.

The experimental work of the thesis was performed in the lab facilities of the Environmental Engineering and Reactor Technology Research Group at Department of Chemical Engineering and in the cleanroom facilities of NTNU NanoLab.

Acknowledgments

First, I want to express my gratitude to my supervisor, Dr. Sulalit Bandyopadhyay, Associate Professor with the Department of Chemical Engineering (NTNU), for his time and guidance throughout this thesis. I thank Katharina Zürbes, PhD candidate at the Department of Chemical Engineering (NTNU), for being my co-supervisor and for many helpful discussions, feedback and practical tips useful in the many experiments conducted throughout the semester. I want to thank Muhammad Bilal, M.Sc student in Biotechnology (NTNU), for a fruitful cooperation, sharing both experiences and samples in the labs. A special thanks go to Anuvansh Sharma, PhD Candidate with the Department of Materials Science and Engineering (NTNU), for all the help and support he has provided, for being so patient, generous and a really good friend. And to the rest of the Particle Engineering Research Group, thank you for including me in your team, for sharing your thoughts, experiences and helpful advice. I also want to thank Dr. Ruth Catharina de Lange Davies, Professor with Department of Physics (NTNU), for being my internal supervisor from the Department of Physics allowing me to perform my master's thesis with the Department of Chemical Engineering.

Finally, I want to thank my family, especially my mom and dad for always believing in me, encouraging me to do what is right for me, and supporting my decisions.

Helena Olivia Karlsen Ramsvik
Trondheim, June 24, 2021

Contents

Table of Figures

Acronyms and Abbreviations

a.u	Arbitrary unit
AsA	Ascorbic acid
BP	Bottom product
C	Concentration
C*	Solubility
Cit	Citrate
CTAB	Cetyltrimethylammonium bromide
DLS	Dynamic light scattering
DNA	Deoxyribonucleic acid
FeOl	Iron oleate
G	Gibb's free energy
$\mathbf{H}_d$	Hydrodynamic diameter
IO	Iron oxide
LPS	Lipopolysaccharides
LSPR	Local surface plasmon resonance
$\mathbf{M}_S$	Saturation magnetization
MQ water	Destilled de-ionized water
MNP(s)	Magnetic nanoparticle(s)
N.A	Not applicable
NaCit	Sodium citrate
NIR	Near infrared, 650-900 nm
NP(s)	Nanoparticle(s)
NR(s)	Nanorod(s)
OA	Oleic acid
PDI	polydispersity index
rpm	Rounds per minute
S	Supersaturation
S(T)EM	Scanning (transmission) electron microscope
TP	Top product
UV-vis	Ultra violet-visible
VSM	Vibrating sample magnetometer
ZP	Zetapotential

Units, Constants and Symbols

$\sim$	approximately
%	percent
°	degree
°C	degree Celsius
g	gram
n	refractive index
N	Newton
nm	nanometre
min	minute(s)
ml	milli litre
mM	milli molar, $^{\mathrm{mmol}}/_{\mathrm{L}}$
mV	milli volt
pH	negative decadic logarithm of the hydrogen ion activity
Δ	change in
θ	contact angle
λ	wavelength

Chapter 1

Introduction

A biosensor can be defined as a device that detects the presence of a target molecule by using a biological recognition element which converts that biochemical interaction into a quantifiable signal that can be measured[1]. The applications of such a device are many, including clinical diagnosis, biomolecular engineering, drug design and detection, environmental monitoring and food quality control[2]. Some well-known inventions using biosensing technology today are the pregnancy test, blood glucose meter and cholesterol meter. The role of biosensors in such important fields have led to an impressive technological advancement since the first biosensor device was introduced by Clark and Lyons in 1962[3]. In fact, there exists a wide range of techniques that can be used for the development of biosensors, and recently, there has been a growing interest in using nanomaterials for this purpose.

With regards to biomedical applications in general, there are especially two classes of nanomaterials that have been extensively studied due to their characteristic properties and biocompatibility, namely plasmonic and magnetic nanoparticles (NPs). Plasmonic NPs are recognized for their optical properties, having a distinct local surface plasmon resonance (LSPR) frequency at which they absorb incoming light[4]. This is a property that has already been widely exploited in biosensing applications[2]. Magnetic NPs on the other hand, are recognized for their superparamagnetic behavior which allow for controlled NP magnetism. Controlled magnetism is a powerful property exploited in various biomedical applications including cellular therapy, tissue repair, hypothermia, targeted drug delivery and magnetic resonance imaging (MRI) contrast[5]. The possibility of combining these materials into a single nanoparticle has gained increasing research interest due to its multifunctional properties. The resulting magneto-plasmonic nanoparticle would exhibit both a characteristic LSPR and superparamagnetic behavior.

1.1 Motivation

Today, biosensors are ubiquitous in biomedical diagnosis as well as a wide range of other areas such as point-of-care monitoring of disease and treatment progression, environmental monitoring, food control, drug discovery, forensics and biomedical research[6]. Blood glucose monitoring (BGM) is perhaps the most successful and widespread application of biosensing technology[7]. Such glucose biosensors are commonly used in clinical applications for diagnosis of diabetes mellitus. Diabetes mellitus is a chronic disease affecting more than 420 million people world-wide[8]. Although a cure does not yet exist for this condition, the lives of many patients have been greatly improved by the availability of inexpensive disposable biosensors for BGM. The ability to accurately determine glucose enables diabetics to control blood glucose levels and thereby minimize the health risks associated with the disease[9]. The glucose biosensor was in fact the first industrial biosensor on the market[6], and its success has inspired the use of biosensing technology in several other areas.

Clinical diagnostics, including virus detection, is one of the areas that has greatly benefited from the use of biosensors[10]. Several viruses, including the human immunodeficiency virus (HIV)[11], hepatitis B virus[12] and the measles virus[13], have already been successfully detected using biosensing technology. With the current outbreak of coronavirus disease (COVID-19), early detection of infection is crucial to prevent this virus from spreading. As of February 2021, there have been 111 593 583 confirmed cases of COVID-19 world wide, including 2 475 020 deaths, reported to the World Health Organization[14]. At the time of writing, there are two standard COVID-19 diagnostic tests in use; the real time - reverse transcription polymerase chain reaction (RT-PCR) test and the antigen test. Whereas the RT-PCR test is highly sensitive, it is also a time consuming process. The antigen test on the other hand, gives very rapid results, but have a higher false-negative rate than the RT-PCR test. In order to overcome these challenges, designing a test that is both sensitive and rapid, nanomaterial-based biosensors have gained increasing attention.

A third important biosensing application is the detection of Lipopolysaccharides (LPS). LPS are bacterial endotoxins that make up for $\sim 75\%$ of the outer membrane surface of Gram-negative bacteria[15]. Gram-negative bacteria, such as *Escherichia coli*, are widely used as a platform for manufacturing pharmaceutical products in which LPS is a common byproduct. However, even sub-nanomolar levels of LPS can cause sepsis, septic shock and multi-organ failure if entered in the human circulation[16]. Thus, detection and removal of LPS from pharmaceuticals is necessary to ensure the safety of the final product. The current standard test for LPS detection, the Limulus Amebocyte Lysate (LAL) assay, is sensitive but also limited in applications due to interference from other molecules[17]. Other disadvantages of the LAL assay are the complex sample preparation process, the time it takes to confirm the presence of endotoxins as well as its high sensitivity to changes in temperature and pH. In recent years, there has been a growing interest to use NPs in LPS detection as a way of overcoming the drawbacks of the LAL assay[18].

1.2 Aim of Project

The goal of this master's thesis has been to tailor magneto-plasmonic NPs, i.e. optimizing their physico-chemical properties, so that they are suitable for biosensing applications. The synthetic routes for making such magneto-plasmonic NPs are so-called seed-mediated processes, and can be divided in two parts. The first part consist of making the single-material NPs onto which the second material can grow in the second part of the synthesis. As it is the presence of the single-material NPs that promote the growth of the second material, they are usually referred to as seed NPs. Furthermore, due to the fact that the optical properties of the plasmonic material is dependent on light-interactions, it is the magnetic material that has been used as seeds in the seed-mediated synthesis of the magneto-plasmonic NPs performed throughout this project. Just like the seed-mediated synthesis protocol, this thesis will consist of two main parts; I) Synthesis of the seed NPs and II) the seed-mediated growth of anisotropic nanostructures.

Chapter 2

Theory

This chapter will elaborate on the existing literature and research on nanoparticles (NPs), starting with their physico-chemical properties and why they have received such increasing interest in the last decades. The established procedures for NP synthesis, as well as the existing theory behind NP formation will be presented, followed by a section on the role of surfactants and surface functionalization of NPs. Finally, the last part of this chapter will be regarding the potential applications of the NPs, with a special focus on their use in biosensing. Parts of the content of this chapter is adapted from previous work[19].

2.1 Nanoparticles and their Properties

Due to their nanometric sizes, typically 1-100 nm in at least one dimension, NPs exhibit exceptional structural and functional properties that do not exist in their parent bulk materials or discrete molecules[4,20]. There are especially two major classes of nanomaterials that have been extensively studied and used in a variety of fields, each of which exhibit well-defined and characteristic properties, namely magnetic and plasmonic NPs. The possibility to combine these two nanomaterials into a single heterodimeric nanoparticle have gained increasing research interest due to their ability to inherit multiple functionalities that can be utilized simultaneously. In addition to synergistic properties, heterodimeric nanostructures can exhibit new collective phenomena originating from the enhancement of the properties of one of its components or interactions between its two moieties[21].

2.1.1 Magnetic Nanoparticles

Nanomaterials consisting of magnetic elements, such as iron (Fe), nickel (Ni), cobalt (Co) etc., exhibit magnetic properties and are thus referred to as magnetic nanoparticles (MNPs). These magnetic properties originate from the spin and angular momentum of the orbiting electrons contained within the compound[22]. When the size of the MNPs is smaller than $\sim$ 50 nm[1], they are only composed of a single magnetic domain and thermal energy fluctuations can be sufficient to cause their magnetization to flip direction[23]. Such MNPs are said to be superparamagnetic, which means that they will magnetize strongly under an applied magnetic field, but will not retain

---

[1] Depending on the material in question

this property once the field is removed (see Figure 2.1). One of the great advantages of superparamagnetic NPs is that they avoid the induced aggregation associated with the residual magnetization of ferromagnetic NPs. This magnetic property makes the MNPs useful for many applications including data storage, spintronics, molecular and cellular isolation, magnetic resonance imaging (MRI) and hyperthermia treatment of cancer[20].

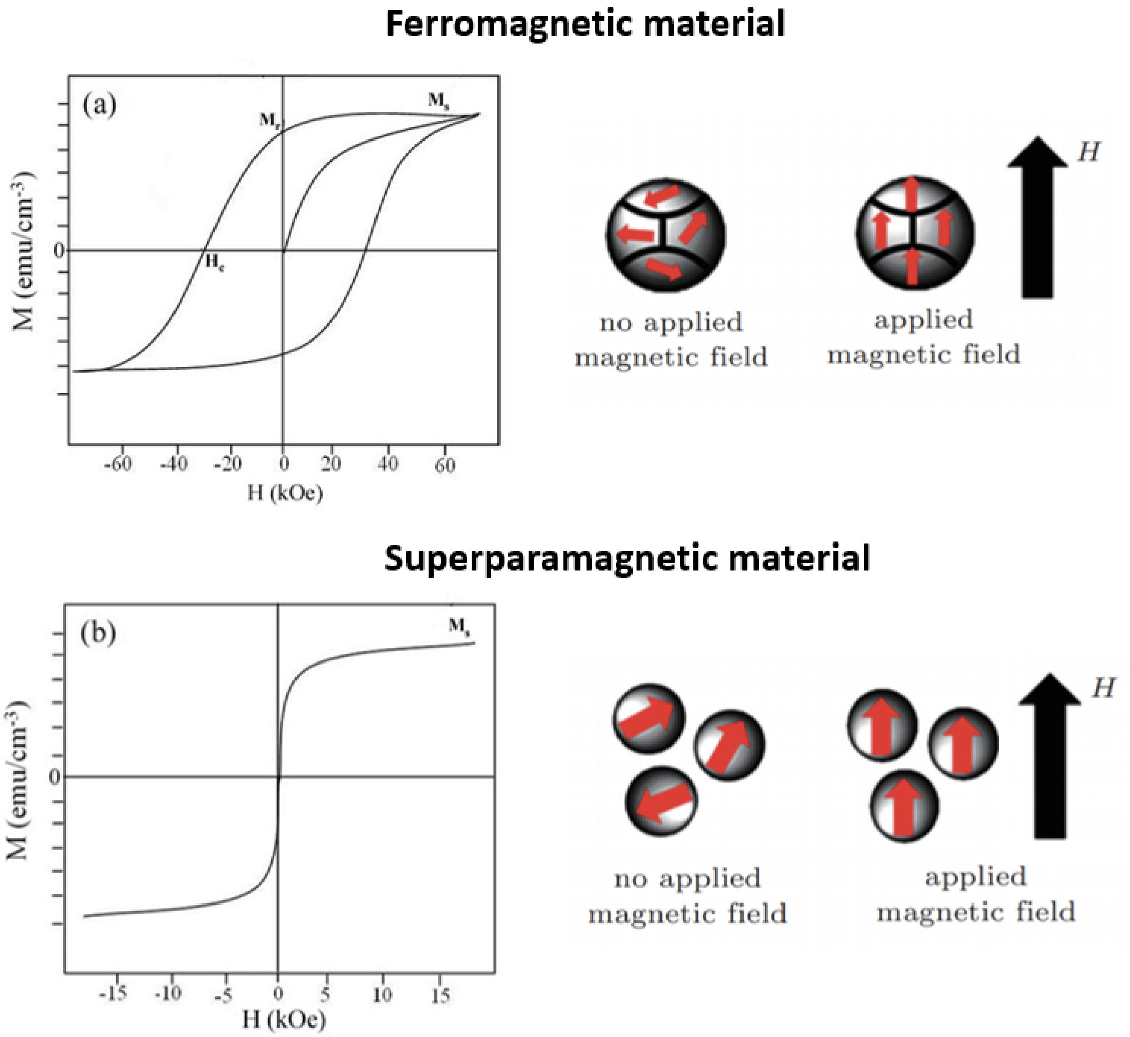

Figure 2.1: Magnetic hysteresis loop and corresponding magnetic domains of (a) ferromagnetic and (b) superparamagnetic material. *Illustrations adapted and modified from refs.* [24,25].

Among the MNPs, iron oxide nanoparticles (IO NPs) are the most frequently used as their magnetic properties can be greatly increased by clustering of a number of individual superparamagnetic NPs into bigger magnetic beads. The IO NPs can exhibit various structural phases, including akaganeite (β-FeOOH), hematite (α-Fe_2O_3), maghemite (γ-Fe_2O_3) and magnetite (Fe_3O_4). Each of the different phase structures give rise to specific magnetic properties[26]. Magnetite is a black ferromagnetic mineral containing both Fe(II) and Fe(III). When their diameter is smaller than ∼ 30 nm, these MNPs become superparamagnetic. Additionally, they are relatively easy to synthesize, biodegradable, stable and their magnetic properties can be tuned by changing their size and shape[20,27].

2.1.2 Plasmonic Nanoparticles

Plasmonic NPs are typically composed of noble metals, such as gold (Au), silver (Ag), platinum (Pt) etc., and are recognized for their remarkable optical properties. Such metals have highly mobile surface electrons, and as a result, they exhibit unique localized surface plasmon resonance (LSPR). LSPR is an optical phenomenon generated by a light wave that gets trapped within metallic NPs smaller than the wavelength of the light[4]. This light-matter interaction results in the collective oscillation of the surface electrons of the NPs in resonance with the oscillating electric field of the incident light[20]. The phenomenon is illustrated in Figure 2.2.

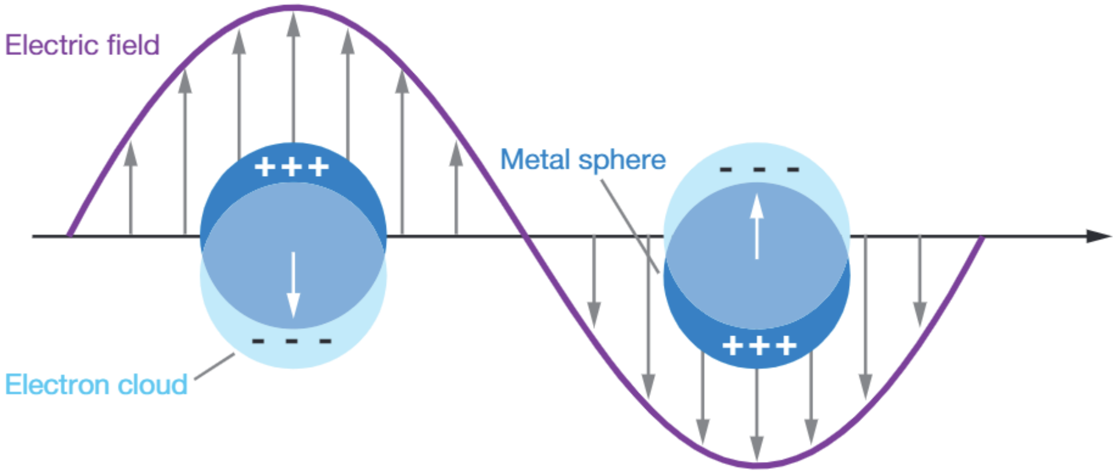

Figure 2.2: Schematic illustration of localized surface plasmonic resonance (LSPR). *Illustration from ref.* [28].

The LSPR of metallic NPs leads to an enhanced local electric field near the metal surface, resulting in strongly enhanced absorption and scattering properties that can be measured and exploited in various applications[29]. In photothermal therapy, for instance, plasmonic NPs are delivered into cancer tumors and irradiated with laser light which is absorbed by the particles[30]. The absorbed light is then non-radiatively relaxed, resulting in the release of thermal energy, effectively killing the surrounding diseased tissue[31]. The resonance frequency (or wavelength) at which the LSPR occurs is dependent on the composition, size, geometry, dielectric environment and particle–particle separation distance of the NPs[4]. This means that plasmonic NPs in various shapes and combinations can be used to tailor the optical properties of the material as desired[32]. The size of the NPs also determines whether the incoming light will be absorbed or scattered. For particles smaller than 20 nm, absorption is the predominant process. Increasing the physical dimensions or effective size of the nanoparticle will increase the probability of light scattering[4].

Both Ag and Au exhibit LSPR in the visible range. Figure 2.3 shows the extinction spectra of 20 nm Ag (blue) and Au (green) NPs in water, which show LSPR peaks at 380 nm and 520 nm respectively[33]. Even though Ag have the sharpest and strongest bands among all metals, Au is often preferred for biological applications due to its inert nature and biocompatibility[4].

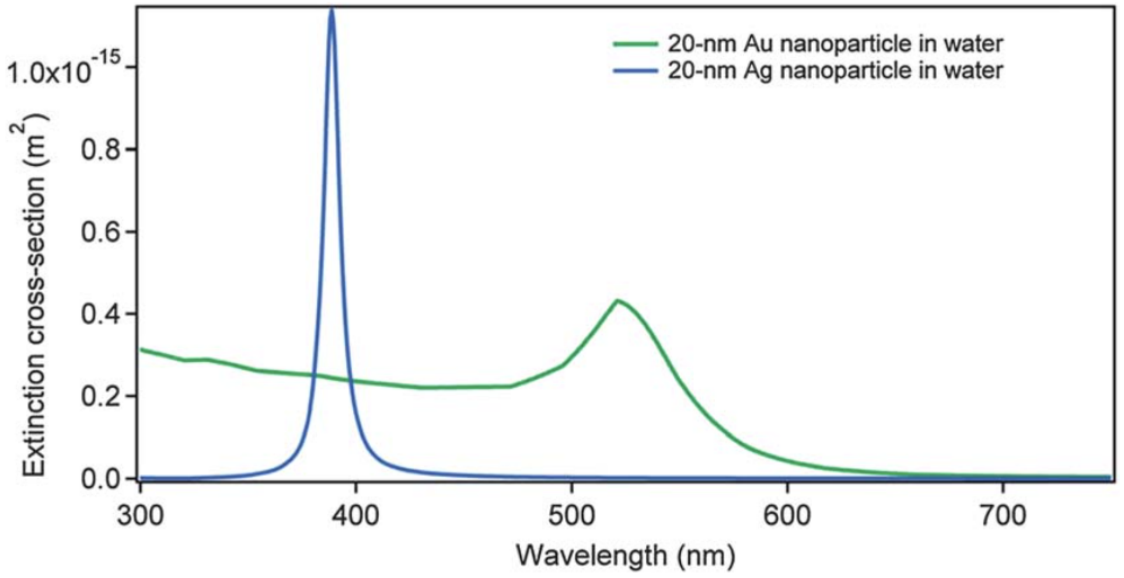

Figure 2.3: Extinction of 20 nm Ag NPs (blue line) and Au NPs (green line) showing LSPR at 380 nm and 520 nm, respectively. *Illustration from ref.* [33].

Additionally, the LSPR of Au NPs can be tuned from the visible to near infrared region (NIR) by adjusting the particle's size, shape and structure[20,33]. NIR light (650-900 nm) is of particular interest in biomedical applications because it can safely penetrate deep into the body (through healthy tissue), only affecting the Au NPs[30,31].

The absorption spectra associated to the LSPR of plasmonic NPs is affected to a greater extent by anisotropy than size-enlargement[4]. This was demonstrated by Marzán[34], by showing that increasing the size of spherical NPs by a factor of 10 results in a red shift of 47 nm, while increasing aspect ratio R (R=long-axis/short-axis) of ellipsoids by a factor of 1.4 results in a shift of the longitudinal band by 92 nm.

Typically, an increase in size, edges or sharpness of the nanoparticle results in a red shift of the absorption spectra as there is an increase in charge separation in these structures, while an increased symmetry results in higher LSPR intensity[4,33]. NPs that can be polarized in several modes will also have several absorption peaks. Thus, anisotropic NPs tend to exhibit multiple, red-shifted peaks in comparison to spherical particles. Nanorods can be polarized along two axis (transverse and longitudinal), resulting in two LSPR peaks. The absoprtion spectra of Au nanospheres vs. Au nanorods is illustrated in Figure 2.4.

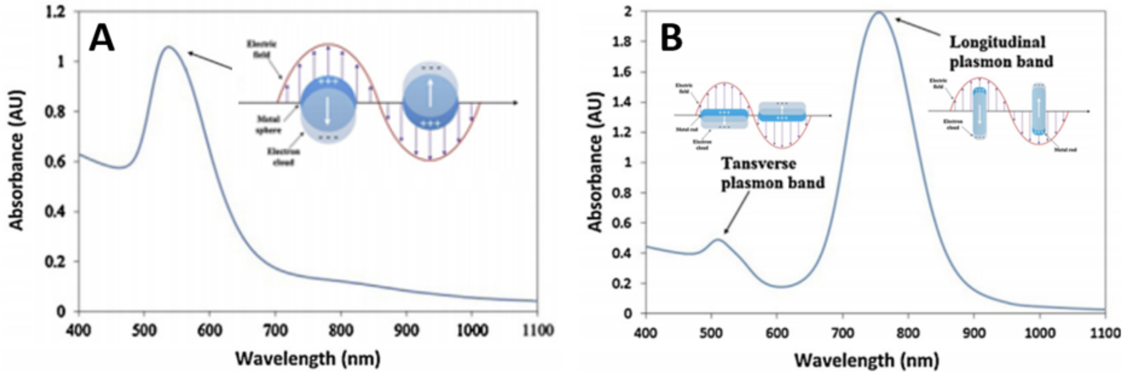

Figure 2.4: Absorption spectra of (A) Au nanospheres and (B) Au nanorods. *Illustration adapted and modified from ref.* [2].

2.1.3 Magneto-Plasmonic Nanoparticles

Magneto-plasmonic NPs are composed of both a magnetic and a plasmonic material combined together into a single NP through solid-solid interfaces. The resulting heterodimeric NPs have the benefit of inheriting the physico-chemical properties of their parent materials. In other words, these particles exhibit the specific characteristics of both superparamagnetism and localized surface plasmon resonance, making them a lot more versatile than their individual monomeric moieties. The expression of these properties have been shown to be directly related to the NP size and morphology[35]. Based on their morphology, heterodimeric NPs can be classified as having either a core-shell, dumbbell-, or raspberry-like structure. The different morphologies are shown in Figure 2.5.

The final morphology of the heterodimeric NPs is both dependent on the structural parameters of the nanomaterials involved as well as the synthesis condition of the particles. This will be discussed in the following sections.

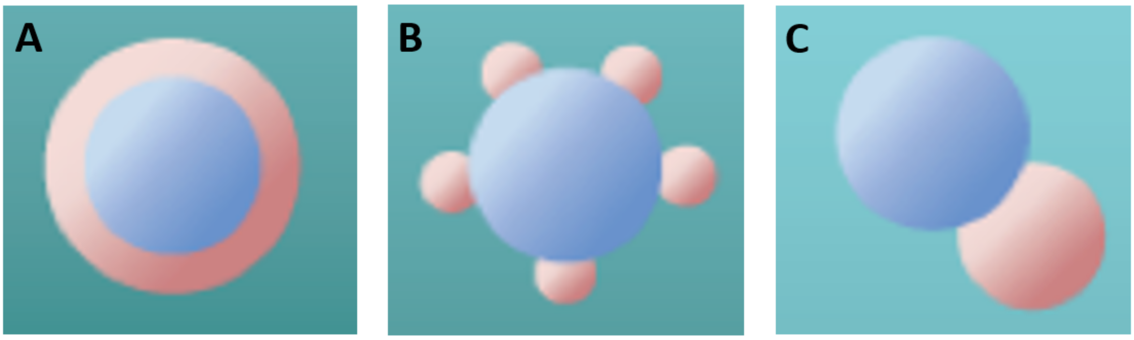

Figure 2.5: Three kinds of heterodimeric nanoparticle morphologies: (A) core-shell (B) raspberry and (C) dumbbell. *Illustration adapted and modified from ref.*[36].

2.2 Nanoparticle Synthesis

There exist numerous ways to synthesize NPs and the methods can be classified as either a "top down" or "bottom up" approach. In the top down procedures, the NPs are derived from larger molecules, whereas in the bottom up approach they are synthesized by nucleation and growth of molecular distributions in either liquid or vapor phase[37]. As the latter allows for a more controlled synthesis with regards to particle size and shape, the bottom up approaches are the most commonly used methods for synthesizing NPs[38]. Generally, for a bottom-up synthesis of NPs to take place, three components are required: a precursor, reducing agent and surfactant. The precursor provides the material of which the NPs will compose, the reducing agent reduces the precursor into the atoms serving as building blocks for the NPs, and the surfactant stabilizes the synthesized NPs by preventing aggregation and other unwanted phenomena such as Ostwald ripening.

2.2.1 Synthesis of Heterodimeric Nanoparticles

The synthetic routes for making heterodimeric NPs are more complex than their individual single-component NPs, and are commonly obtained by sequential growth of a second component on so-called seeds[21,39]. This is a two step synthesis: First, one of the two components is synthesized, for example the magnetic part, following a regular single material NP synthesis procedure. In the second step, these NPs are added as seeds in the growth solution of the second material, which then will nucleate and grow on the seeds resulting in heterodimeric particles. Two of the most commonly used materials for magneto-plasmonic NPs are iron oxide combined with gold for the magnetic and plasmonic parts respectively.

2.2.2 Synthesis of Iron Oxide Nanoparticles

Due to their unique physico-chemical and magnetic properties, as well as their wide spread of biomedical applications[40], several techniques have been developed in order to synthesize IO NPs. Some of the commonly used methods include thermal decomposition[41], microemulsion[42], electrochemical[43], solvothermal[44], sol-gel[45], sonochemical[46], and co-precipitation[47]. The different methods have different advantages and disadvantages. Here, only the thermal decomposition and co-precipitation methods will be presented, which are two common techniques used to obtain magnetite (Fe_3O_4) NPs.

Co-Precipitation

Co-precipitation is often considered to be the simplest and most efficient technique for synthesizing magnetic IO NPs[47]. The method takes advantage of the difference in solubility of Fe^{2+}/Fe^{3+} salts in water and involves their simultaneous precipitation into iron oxides. This reaction is promoted by the addition of a base, usually sodium hydroxide (NaOH) or ammonium hydroxide (NH_4OH). The reaction can be described as follows[47,48]:

$$Fe^{2+} + 2Fe^{3+} + 8OH^{-} \rightarrow Fe(OH)_2 + 2Fe(OH)_3 \rightarrow Fe_3O_4 + 4H_2O$$

The main advantage of the co-precipitation technique is its large yield of IO NPs[47]. However, the resulting particles have a wide size distribution as the method provides very little control over particle size and morphology[49]. The IO NPs generally have sizes in the range of 5-33 nm[50,51] and exhibit thus superparamagnetic behavior.

Thermal Decomposition

Thermal decomposition allows for the effective production of monodisperse, size- and shape-controlled particles at large scale[41,52]. The method involves the thermal decomposition of an iron precursor in high boiling organic solvents containing surfactants[35]. The most commonly used precursors include iron pentacarbonyl ($Fe(CO)_5$), iron oleate (FeOl) and iron acetyl acetonate ($Fe(acac)_3$), whereas the surfactants are usually oleic acid (OA) and/or oleylamine. The thermal decomposition method yields IO NPs with a typical size distribution between 4 and 19 nm, ensuring the superparamagnetic properties of the particles[52,53]. The main advantage of this method over the co-precipitation method is the narrow size distribution of the particles it produces. However, the thermal decomposition IO NPs are dispersed in organic solvents which are hazardous to any biological environment[54]. Thus, in order for the IO NPs to be used in biomedical applications, they first have to be phase transferred into aqueous solution. This intermediate step is avoided in water-based synthesis methods such as the co-precipitation method.

2.2.3 Gold Nanoparticle Synthesis

As one of the most commonly used materials for plasmonic NPs, there exist a variety of techniques for synthesizing gold nanoparticles (Au NPs), including electrochemical[55], sonochemical[56], thermal[57] or photochemical[58] reduction. The most commonly used synthesis pathway however, is by chemical reduction[59]. In this method, gold ions (Au^{3+} or Au^{1+}) are reduced to metallic gold (Au^0) by the addition of a reducing agent (electron donor), commonly citric acids or borohydrides[60]. The Au^0 building units are further assembled into Au NPs, which are stabilized by the presence of stabilizing agents such as sodium citrate (NaCit) or cetyltrimethylammonium bromide (CTAB)[60]. The resulting Au NPs have spherical morphologies.

Anisotropic Au nanorods, on the other hand, are commonly synthesized through a silver assisted, seed-mediated method[61]. In a typical synthesis, ascorbic acid (AsA) is used as a mild reducing agent and added to an aqueous solution of CTAB, silver nitrate ($AgNO_3$), and chloroauric acid ($HAuCl_4$) in order to selectively reduce Au^{3+} to Au^{1+}. Thereafter, the addition of a seed solution containing small spherical Au NPs catalyses the reduction of Au^{1+} ions onto their surface, resulting in anisotropic growth[62]. The aspect ratios of the resulting nanorods ranges from 1 up to 18 and can be tuned by adding different volumes of seed solution[62].

Despite numerous experiments resulting in the synthesis of NPs of different materials and with several different morphologies, the detailed reaction mechanism and how the synthesis conditions and parameters influence the overall process are still not fully understood[63]. In order to coherently design and precisely synthesize NPs for their target use, a thorough understanding of the growth mechanism is vital.

2.3 Crystallization: General Nucleation and Growth Theory

Crystallization can be defined as the phase transition of matter from a disordered high free energy state, to a low free energy crystal state. The crystal state is characterized by a repeating pattern of the crystal's building blocks exhibiting a long-range ordered structure. The crystallization process can be divided into two steps; nucleation, and growth. Nucleation is often considered as the birth of a solid as it is the first step in the formation of the new phase[64]. Once the initial nucleus is formed, it serves as a site upon which additional monomeric building units are deposited in the second part of the crystallization process, namely crystal growth[65].

2.3.1 Supersaturation is the Thermodynamic Driving Force

In order for nucleation and growth to occur in a given solution, the crystallizing species must be supersaturated in the solution[66]. Supersaturation (S) is in fact the thermodynamic driving force pushing the system towards crystallization, and can be defined as the ratio between the concentration (C) and solubility (C^*) of the crystallizing species: $S = C/C^*$. Once supersaturation is established, the free atoms in the solution will start to nucleate and the resulting nuclei will grow if left in the supersaturated solution[66].

2.3.2 Homogeneous Nucleation

When a nucleus spontaneously forms in a pure liquid solution, i.e. without the presence of any other surfaces, it is referred to as homogeneous nucleation[65]. This process can be considered thermodynamically by looking at the total Gibbs free energy change ΔG, which is defined as the sum of the free energy change for phase transformation (ΔG_V) and the free energy change for the formation of a new surface (ΔG_S):

$$\Delta G = \Delta G_S + \Delta G_V \tag{2.1}$$

In the homogeneous nucleation reaction, ΔG_V has a negative contribution and will promote nucleation, while ΔG_S has a positive contribution as it represents the energy cost of creating a solid-liquid interface[65]. ΔG_S can be expressed as the product of the surface area of the crystallite (A) and the surface free energy of the interface (γ). Thus, for a spherical particle of radius r, the total free energy change of homogeneous nucleation can be expressed as follows:

$$\Delta G = \Delta G_S + \Delta G_V = A\gamma + V\Delta G_v = 4\pi r^2\gamma + \frac{4}{3}\pi r^3\Delta G_v \tag{2.2}$$

where ΔG_v is the free energy change of phase transformation per unit volume and is equal to the difference in chemical potential as it is the driving force of the reaction:

$$\Delta G_v = -\Delta\mu_v = \frac{-k_B T ln(S)}{v}. \tag{2.3}$$

Here, T is the temperature, k_B is the Boltzmann's constant, S is the supersaturation of the solution, and v is the molar volume of the crystal. The maximum value of ΔG corresponds to the activation energy barrier (ΔG_{crit}) a nucleus has to overcome in order to be stable, and can be found by differentiating equation (2.2) with respect to r and setting it to zero, $d\Delta G/dr = 0$. The radius which satisfies this condition is called the critical radius (r_{crit}) and corresponds to the minimum radius above which a nucleus is stable in the solution not being redissolved[65]. The expressions for r_{crit} and ΔG_{crit} are given in equations (2.4) and (2.5) respectively:

$$r_{crit} = \frac{-2\gamma}{\Delta G_v} = \frac{2\gamma v}{k_B T ln(S)} \tag{2.4}$$

$$\Delta G_{crit} = \Delta G|_{r_{crit}} = \frac{4}{3}\pi\gamma r_{crit}^2 \tag{2.5}$$

Figure 2.6 shows how the Gibbs free energy for homogeneous nucleation changes as a function of the nucleus radius.

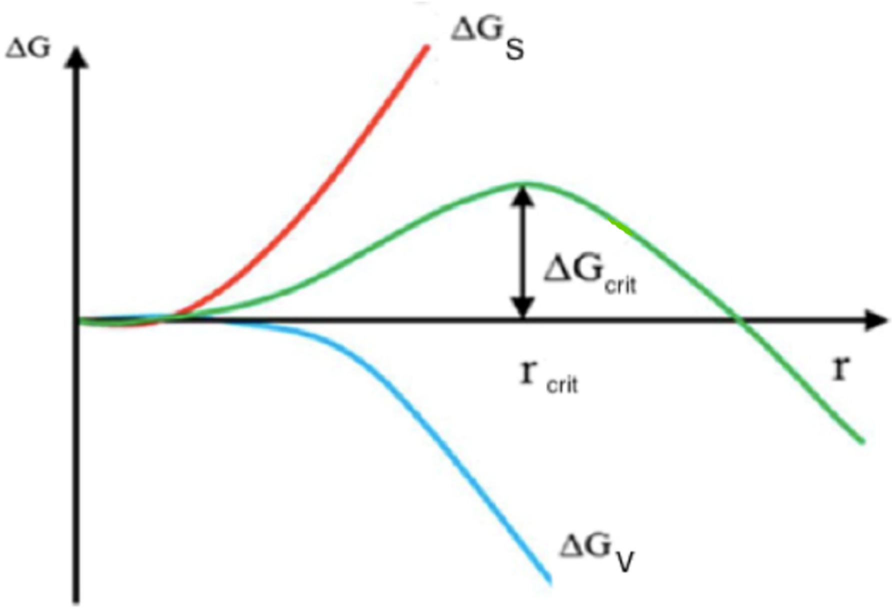

Figure 2.6: Plot of the free energy changes present in homogeneous nucleation as a function of the formed nucleus radius. ΔG_S (red) is the Gibbs free energy change for the formation of a new surface, ΔG_V (blue) is the Gibbs free energy change related to the phase transformation and ΔG (green) is the total Gibbs free energy change which is the sum of the two former terms. ΔG_{crit} denotes the activation energy barrier a nucleus has to overcome in order to form a stable nucleus. The radius associated to this value (r_{crit}) corresponds to the minimum size at which a nucleus can survive in solution without being redissolved. *Illustration adapted and modified from ref.[67]*.

As seen from equations (2.4) and (2.5) there are three ways to reduce the activation energy barrier in order to promote nucleation; (i) increasing the supersaturation (S), (ii) decreasing the interfacial tension (γ) or (iii) increasing the temperature (T).

2.3.3 Heterogeneous Nucleation

In the availability of a solid surface (e.g impurities, walls, bubbles etc.), nucleation will occur on the surface of the foreign body and is referred to as heterogeneous nucleation[65]. Heterogeneous nucleations have a much lower interfacial free energy change (ΔG_S) than homogeneous nucleations, and will thus be energetically favorable. This is because, in the former, the newly formed solid nuclei has a much lower surface to volume ratio as compared to the latter. As a result the activation energy barrier is reduced by a factor ϕ. This factor is dependent on the contact angle (θ) between the surface and the nucleus:

$$\Delta G_{crit}^{het} = \phi \Delta G_{crit}^{hom} \tag{2.6}$$

with

$$\phi = \frac{1}{4}(2 + \cos\theta)(1 - \cos\theta)^2 \tag{2.7}$$

The contact angle θ is another way of representing the surface to volume ratio of the formed nuclei. An illustration of a heterogeneous nucleation as a function of the contact angle θ between the nucleus and the solid surface is shown in Figure 2.7.

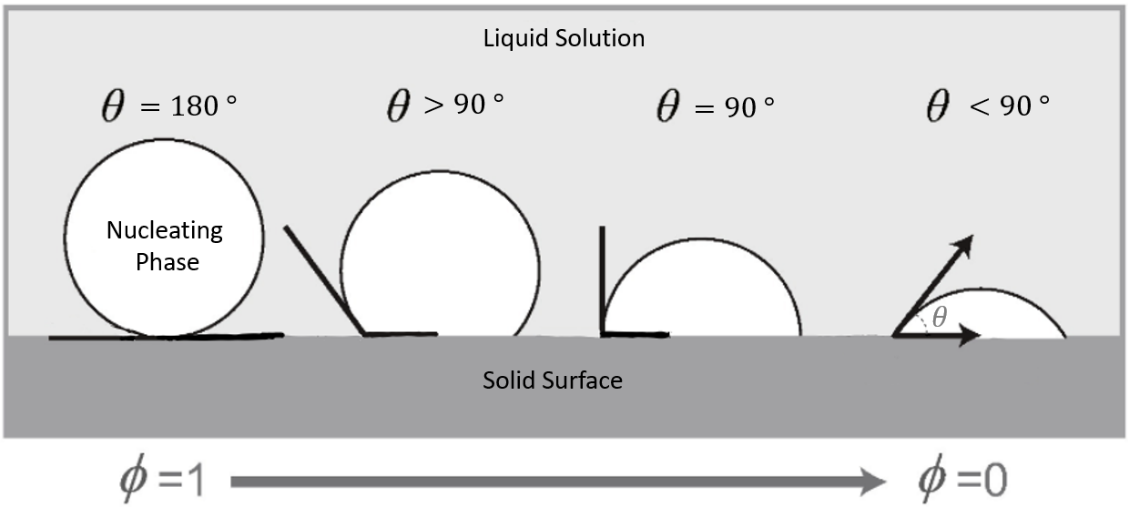

Figure 2.7: Illustration of heterogeneous nucleation as a function of the contact angle θ between the nucleus and the solid surface. As the contact angle increases the surface to volume ratio of the nucleating phase is reduced consequently reducing the total free energy change of the reaction. *Illustrations adapted and modified from ref.*[68]

2.3.4 The LaMer Mechanism

The LaMer mechanism, developed in 1950 by LaMer and Dinegar[69], is generally used to describe the formation of colloidal nanoparticles in solution[36]. The model describes the energy-landscapes associated to nucleation and growth, both in the case of homogeneous and heterogeneous nucleation, and is summarized in Figure 2.8 where the concentration of the free monomers in solution is schematically plotted as a function of the reaction timeline.

According to the LaMer model, the process of nucleation and growth can be divided into three events. The initial step consist of generating a supersaturated solution by a rapid increase of free monomer concentration. Secondly, after the concentration has exceeded the minimum concentration required for nucleation (C^{nu}_{min}), the monomers undergo "burst-nucleation" that consumes most of the supersaturation and thus significantly reduces the monomer concentration. After this point the supersaturation never surpasses the C^{nu}_{min}, and no further nucleation is possible. In the third step, the remaining supersaturation is consumed by the growth of the nuclei, a process which has a much lower activation energy barrier, thus requiring a much lower supersaturation in order to occur[36,65]. Because of this chronological order of events, the resulting

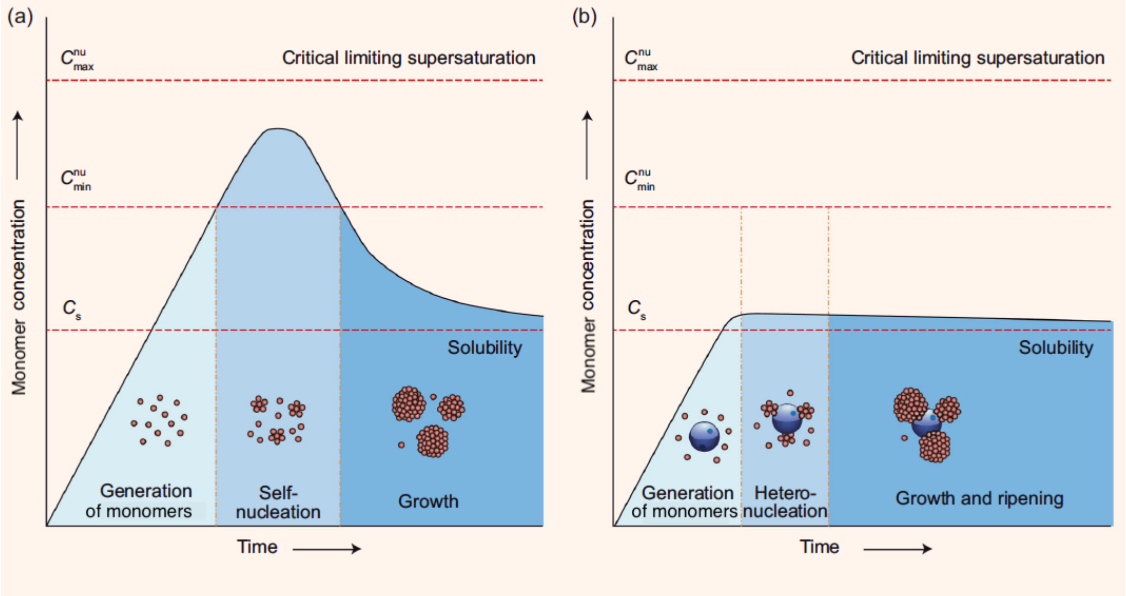

Figure 2.8: LaMer diagrams showing the monomer concentration in the solution as a function of time in the case of (a) homogeneous nucleation and (b) heterogeneous nucleation. The diagram is a representation of the energy landscapes associated to the nucleation and growth process in the two cases. The vertical red lines indicate the concentrations at which the solution is supersaturated (C_S), the minimum concentration required for nucleation (C^{nu}_{min}), and the critical limiting supersaturation (C^{nu}_{max}). *Illustration from ref.*[36].

particles have a very monodisperse size distribution. This is due to the fact that all the nuclei are formed simultaneously, and are thus exposed to the same growth conditions for the same amount of time.

When comparing Figure 2.8 (a) and (b), it is clear that the concentration at which the nucleation occurs in the two cases is very different. In order for homogeneous nucleation to occur, a much higher monomer concentration is required than for heterogeneous nucleation. In fact, in order for heterogeneous nucleation to occur the solution barely has to be supersaturated, and the activation energy barrier is almost as low for nucleation as it is for growth. The LaMer diagram however, does not account for the type of material involved in the nucleation which will greatly influence the contact angle between the materials and thus affect the activation energy barrier.

2.3.5 Growth Mechanisms of Heterodimeric Nanoparticles

As mentioned in Section 2.2.1, in the case of heterodimeric NPs, the synthesis of the second material occurs by heterogeneous nucleation and growth on pre-synthesized seeds. This process is, as mentioned in Section 2.3.3, dependent on the contact angle θ, i.e. the level of wetting, between the two materials involved. In fact, when a second material is supersaturated in a seed containing solution, there are three kinds of interactions that may occur between them. Favorable interactions corresponds to small angles, and if $\theta < 30^\circ$ the materials are said to have a very good wettability[36]. As given by equations (2.6) and (2.7), small angles leads to a small activation energy barriers. This means that in the case of very good wettability, the second material will easily nucleate on the seed, resulting in particles with a core-shell structure. When the contact angle is in the range between $30^\circ - 150^\circ$, the interaction is more or less unfavorable and the heterogeneous nucleation will occur at preferential sites of the seed (e.g. phase boundaries and surface defects). Depending on the reaction conditions, the heterodimeric nanoparticles in this case could end up with either a dumbbell or raspberry structure corresponding to a single-site or multiple-site nucleation respectively. When the contact angle exceeds 150°, the two materials can be considered as non-interacting. In this case, $\phi \approx 1$ and the activation energy barrier of heterogeneous nucleation approaches that of homogeneous nucleation (Equation (2.6)), leading to independent nucleation and growth of the second material. This results in a system with the presence of two nanomaterials which are isolated from one another. The three different cases are illustrated in Figure 2.9 where the proportionality factor ϕ is plotted as a function of the contact angle θ.

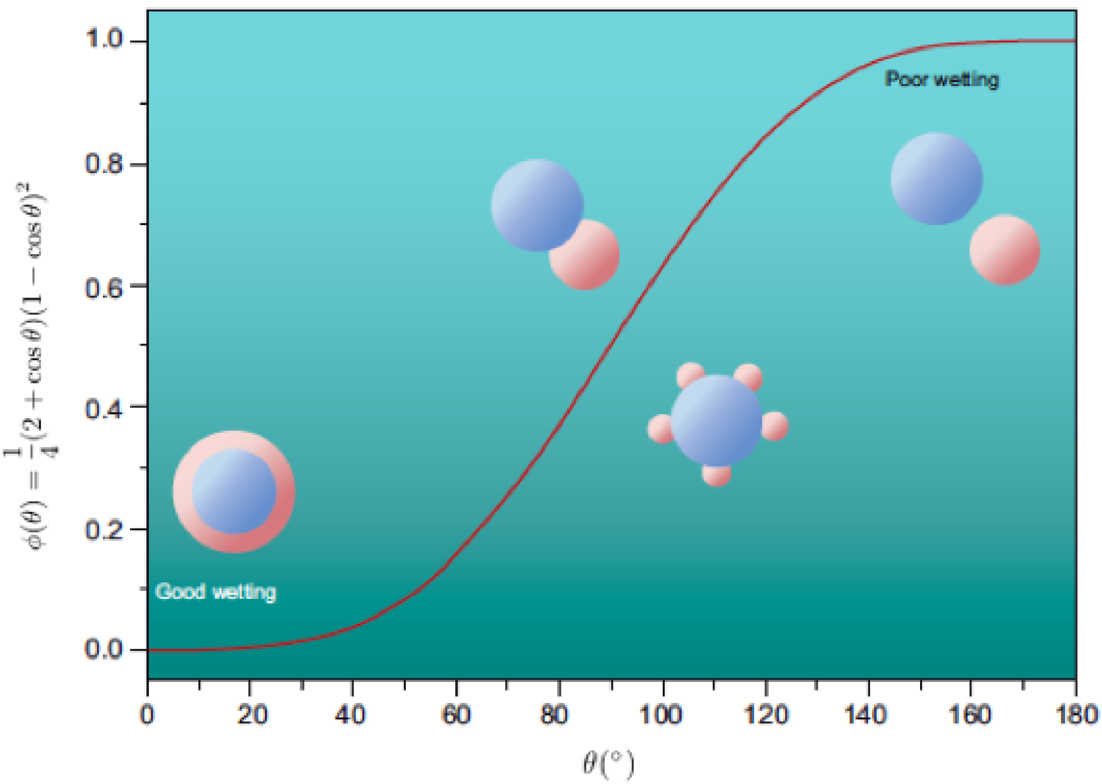

Figure 2.9: The proportionality factor ϕ as a function of the contact angle θ between the nanoparticle seed (blue) and the overgrown material (red). *Illustration adapted and modified from ref.*[36].

The contact angle itself is determined by the structural compatibility between the crystalline characteristics of the two components. Generally, solid materials are characterized by the arrangement of their atoms, and can be either crystalline or amorphous. A crystalline solid has a long-range highly ordered structure, forming a continuous (unbroken) crystal lattice. An amorphous solid on the other hand, has only a short-range order and no apparent characteristic morphology. When synthesizing heterodimeric nanoparticles using the seed-mediated method, there are four different structural combinations possible as illustrated in Figure 2.10.

Amorphous solids have no structural restrictions when nucleating heterogeneously on a pre-existing surface. This is due to the lack of atomic ordering which increases the mechanical flexibility of the solid and limits the interfacial stress between the seed and the second overgrown material[36]. Thus, when the overgrown material is amorphous, the resulting heterodimeric nanoparticle tend to form core-shell structures regardless of the crystallinity of the seed (Figure 2.10, I). When the second material is highly crystalline on the other hand, the lattice structures of the two materials need to be similar in order for the heterogeneous nucleation to be energetically favorable[36]. The interatomic distance in the crystalline material cannot be freely stretched, and when the seed material is amorphous or a highly crystalline material of a different structure, the nucleation sites are limited. Thus, the product will be dumbbell nanoparticles (Figure 2.10, II and III). The third possible combination is having a highly crystalline seed with a highly crystalline overgrown material of similar lattice structures. Due to the match in crystal structures, the interfacial energy will be low, allowing for multiple nucleation sites. The overgrown material will thus epitaxially grow on the seed, resulting in core-shell nanoparticles (Figure 2.10, IV).

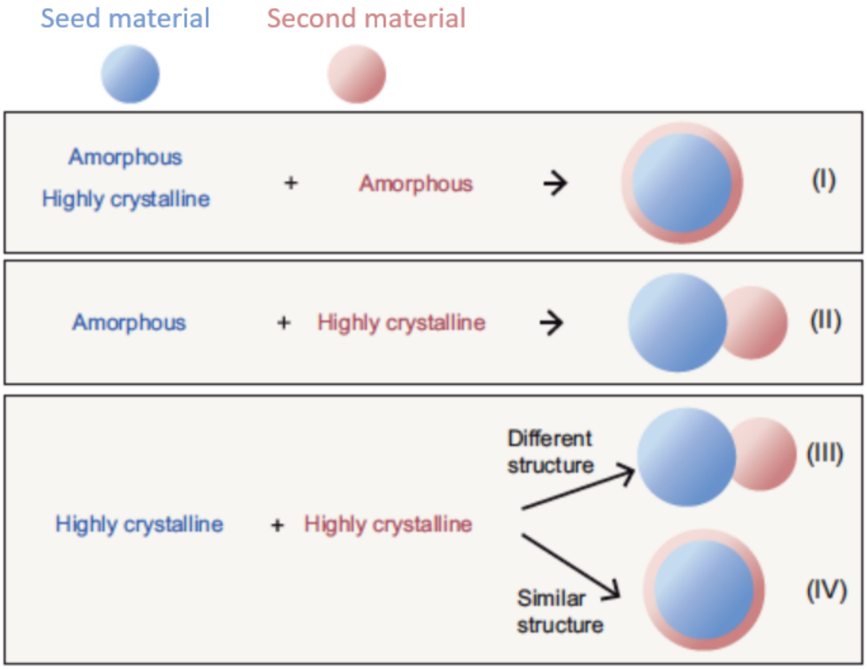

Figure 2.10: The four different structural combinations of seed nanoparticles and overgrown materials and their resulting products. *Illustration from ref.*[36].

2.3.6 Anisotropic Growth

When metal salts are reduced in solution they generally form spherical nanoparticles, as the sphere is the lowest energy shape[38]. In the case of structurally isotropic materials that have face centered cubic (fcc) lattice structures, growth into low-symmetry nanostructures is highly unfavored. Yet, the silver assisted seed-mediated growth of Au nanorods have shown that anisotropic NPs can be synthesized with a yield over 99%[70]. Furthermore, it has been experimentally shown that both CTAB and $AgNO_3$ play crucial roles in promoting the growth of anisotropic structures[62]. However, the exact growth mechanisms taking place during the synthesis are still not fully understood. In order to explain the formation of these anisotropic nanoparticles as seen from experiments, three different mechanisms have been proposed[71], which are summarized in Figure 2.11.

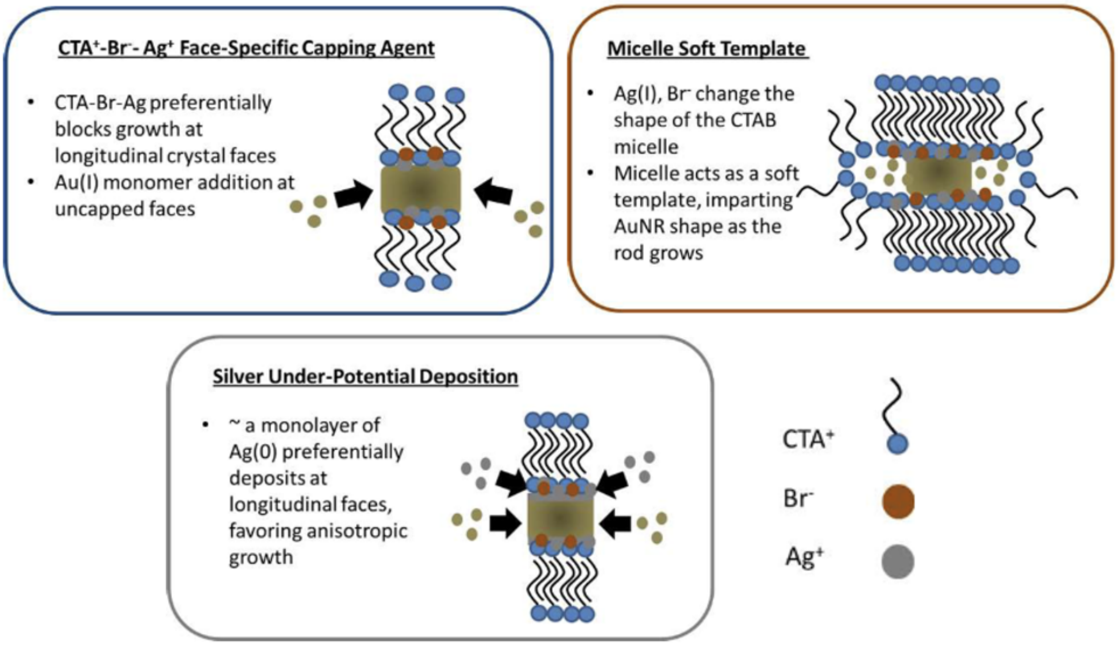

Figure 2.11: Schematic representation of three different mechanisms proposed to explain the anisotropic growth experimentally observed in the silver assisted seed-mediated synthesis of Au nanorods. *Illustration adapted from ref.*[71].

One of the mechanisms suggest that the silver bromide complexes that are formed when $AgNO_3$ is added to the aqueous CTAB solution, are preferentially adsorbed onto the Au NP surface and restricts growth at the longitudinal crystal faces[71]. In the second proposed mechanism, it is suggested that the presence of Ag^+ and Br^- gives the CTAB micelle a cylindrical/rod shape. The micelle is thought to act as a "soft template" for the nanoparticle growth[71]. The third mechanism, referring to silver under-potential deposition, proposes that even though the reduction potential of the Au nanorod growth solution is not sufficient enough to reduce Ag^{1+} to Ag^0, it can reduce Ag^+ to a submonolayer of silver metal. This silver submonolayer is deposited at specific faces of the Au nanorod, preventing further Au growth at these sites[71].

Each of the proposed mechanisms have been supported by experimental data, however several contradicting observations have also been made, leaving the mechanism of anisotropic growth of Au nanorods a mystery yet to be solved[71].

2.4 Surfactants and Surface Functionalization

Functionalization of NPs refers to surface modification processes that makes the particles more suitable for their target application. The thermal decomposition synthesis of IO NPs, for instance, results in particles that are dispersed in organic solvents and are thus unfit for biological applications. In order to phase transfer such NPs from organic to aqueous solutions, ligand-exchange processes are often used to make the particle surface hydrophilic[54]. CTAB[72] and NaCit[73] are ligands commonly used for this purpose.

CTAB is a large (364,45 Da) cationic surfactant molecule that adsorb onto the surface of NPs and reduces their surface energy[74]. As the surfactant has a positive charge, it keeps the NPs stable and prevent aggregation due to electro-static repulsion. CTAB is, however, highly toxic to cultured cells and tissues. Consequently, CTAB phase transferred NPs must therefore be accompanied by another ligand-exchange process before they can be used in biomedical applications[74]. Poly-ethylene glycol (PEG) is a molecule often used for this purpose[75].

NaCit is a smaller (258,06 Da) negatively charged stabilizing agent commonly used in iron oxide nanoparticle (IO NP) synthesis[74]. It also stabilizes the NPs through electrostatic repulsion. As opposted to CTAB however, citrate is non-toxic, biodegradable and biocompatible and thus, citrate capped NPs can directly be used in biomedical applications[74].

2.5 Biosensing Applications

A biosensor can be defined as a device that detects the presence of a target-molecule by using a biological recognition element, and converts the signal into a form that can be measured such as an electrical, optical or magnetic signal. A schematic illustration of a biosensor and its elements is shown in Figure 2.12.

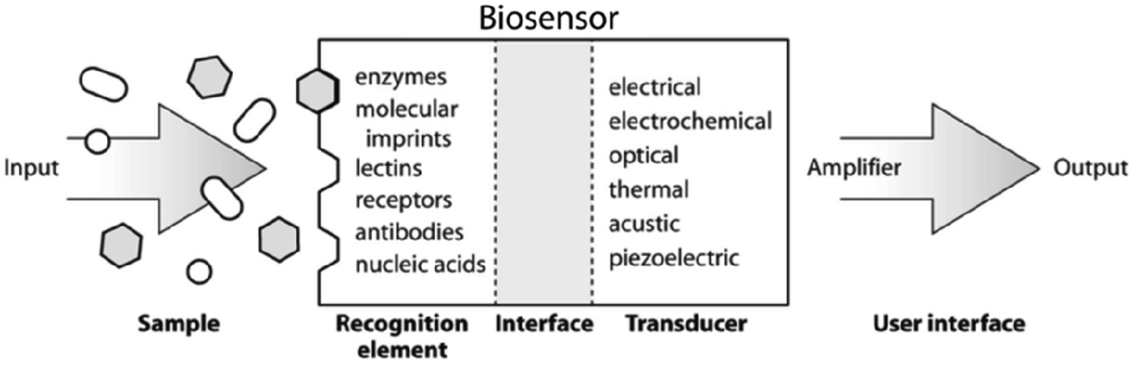

Figure 2.12: Schematic illustration of a biosensor. *Illustration from ref.*[76].

Due to their optical properties, as described in Section 2.1.2, Au NPs have gained increasing attention for their application as optical nano-biosensors[1]. The highly enhanced and confined electromagnetic field induced by the LSPR of the NPs serves as a very sensitive probe that can detect changes in the surrounding dielectric environment. Traditional LSPR-based sensors detect changes in the local refractive index at the NP surface. These changes, typically induced by biomolecular interactions at the NP surface, can be monitored as it results in a distinct shift in the LSPR peak wavelength[1,77]. The shift of the LSPR peak wavelength ($\Delta\lambda$) in response to changes in the dielectric environment can be expressed as follows[2]:

$$\Delta\lambda = m\Delta n\left[1 - exp\left(\frac{-2d}{l_d}\right)\right]. \tag{2.8}$$

Here, m denotes the bulk refractive index response of the NPs, Δn is the change in refractive index, d represents the effective thickness of the adsorbed biomolecule layer and l_d is the characteristic electro-magnetic field decay length.

As opposed to nanospheres, nanorods have two absorption bands (see Figure 2.4), a longitudinal plasmon band (LPB) and a transverse plasmon band (TPB) corresponding to electron oscillations along the long and short axis of the nanorod respectively[2]. Whereas the TPB has been shown to be insensitive to changes in the surrounding dielectric environment, the LPB shows a red-shift in LSPR wavelength with increasing aspect ratios and a high sensitivity to changes in refractive index[2]. In fact, an ellipsoidal nanoparticle with an aspect ratio 5:1 have a dielectric sensitivity that is 5-10 times greater than that of a spherical nanoparticle as illustrated in Figure 2.13[78].

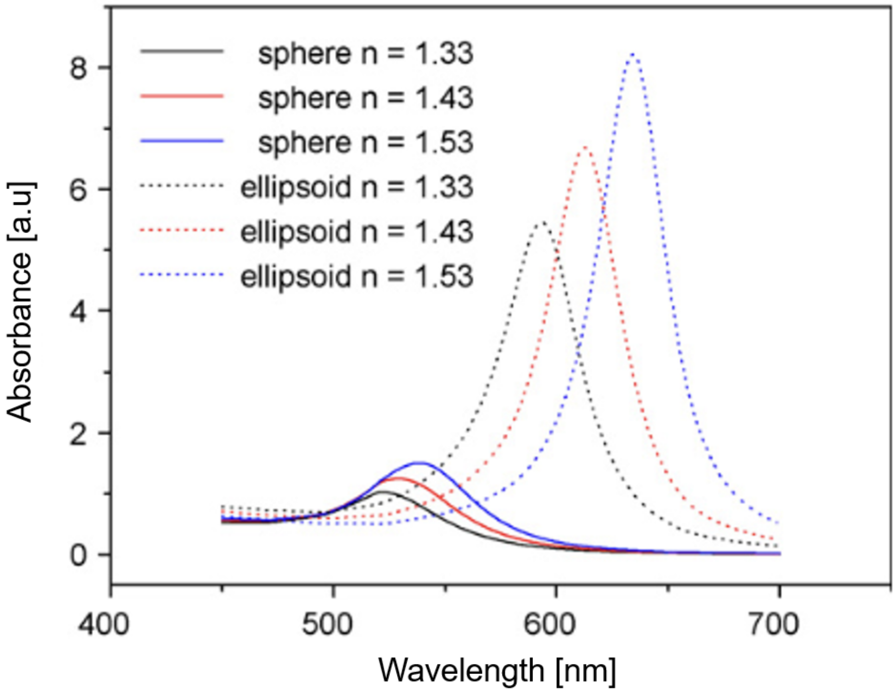

Figure 2.13: Absorption spectra of 20 nm spherical NPs as compared to the one of ellipsoids with an aspect ratio of 2, when the surrounding refractive index n changes. *Illustration adapted and modified from ref.*[1].

In order to use the LSPR property of the NPs for sensing of biomolecules, the biomolecules need to specifically attach to the NP surface. To ensure that only the target molecule attaches and promotes the LSPR shift, the NPs have to be surface functionalized with a molecule that specifically binds to the target. The most common biosensor-biomolecule binding is based on antigen-antibody interaction, nucleic acid interaction (two complementary strands), enzymatic interaction (enzyme-substrate), or cellular interaction (microorganisms, proteins)[79]. Figure 2.14 shows an example of surface functionalized NPs, how the target analyte attaches, and how this is detected as a shift in the LSPR wavelength.

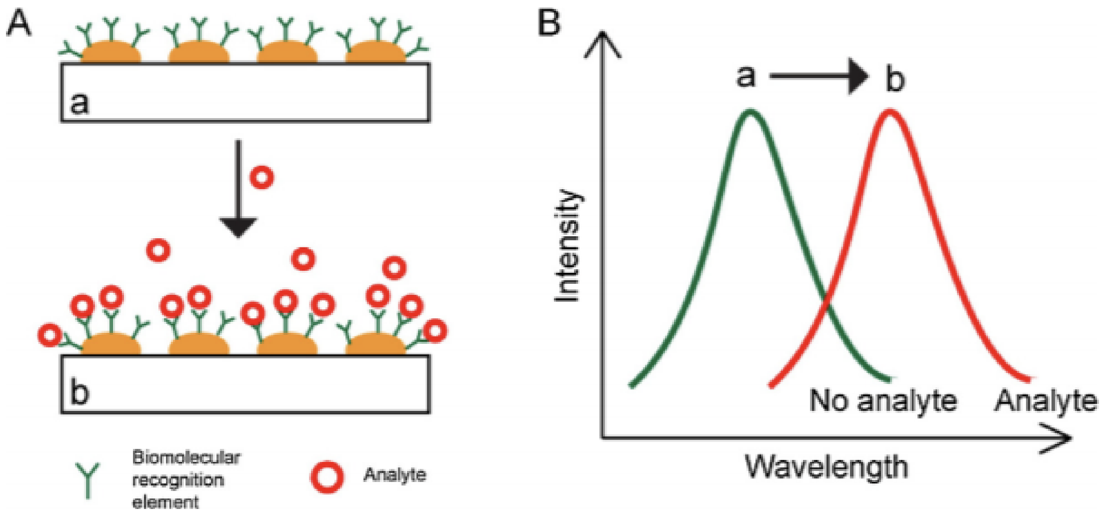

Figure 2.14: Illustration of a LSPR based nano-biosensor. *Illustration from ref.*[80].

Clinical diagnostics, including virus detection, is one of the areas that has greatly benefited from the use of biosensors[10]. Several viruses, including the human immunodeficiency virus (HIV)[11], hepatitis B virus[12] and the measles virus[13], have already been successfully detected using biosensing technology. With the current outbreak of coronavirus disease (COVID-19), early detection of infection is crucial to prevent this deadly virus from spreading. By coating the nanoparticles with the complementary single-stranded nucleic acid aptamer of the virus, these nano-biosensors could be an alternative, faster, and more accurate method of detecting COVID-19 in clinical samples[81]. This technique has already been explored by Su et al[82]. who decorated Au NPs with a single stranded lipopolysaccharide (LPS) DNA aptamer in order to selectively and sensitively detect the endotoxin in crude biological liquors. With this method they were able to detect LPS at concentrations as low as 0.1 pg/ml.

Biosensors are also used in several other scientific fields including food quality, environmental monitoring, biomolecular engineering, drug design and detection[1,2].

Chapter 3

Experimental Section

3.1 Chemicals

Gold(III) chloride trihydrate ($HAuCl_4$,≥99.9%), methanol (≥99.8%), oleic acid (OA, ≥ 99%), sodium citrate dihydrate (NaCit, ≥ 99%), hexane (≥ 99%), 1-Octadecene (90%), Chloroform-d (99.8%), sodium borohydrate ($NaBH_4$, ≥ 98.0%), silver nitrate ($AgNO_3$, ≥ 99.0%), sodium hydroxide (NaOH, ≥ 99.0%, pellets), ammonia solution (NH_4OH, 25%) and iron(III)chloride hexahydrate ($FeCl_3$, ≥ 99%) were purchased from Sigma-Aldrich®. Hexadecyltrimethylammonium bromide (CTAB, ≥ 99%) was purchased from Acros Organics®. Toluene (technical), isopropanol (technical), acetone (technical), hydrochloric acid (HCl, 37%), ethanol (absolute) and iron(II)chloride tetrahydrate ($FeCl_2$, ≥ 99.0%) were purchased from VWR chemicals®. D-(-)-Isoascorbic acid (AsA, 98%) was purchased from Alfa Aesar®, sodium Oleate (NaOl, ≥97.0%) was purchased from Tokyo Chemical Industry®, and argon gas (Ar, ≥ 99.999%) was purchased from AGA AS®.

All chemicals were used as received without any further purification or modification. The distilled de-ionized water (MQ water) used had a resistivity $\sim$ 18.2 MΩ/cm at 25°, taken from Simplicity® Millipore water purification system.

3.2 Synthesis of Iron Oxide Nanoparticles

3.2.1 Co-Precipitation

Citrate capped-Cit Iron oxide nanoparticles (IO-Cit NPs) were synthesized following a co-precipitation protocol modified from Zhou et al[83]. An overview of the method and the experimental set-up is shown in Figure 3.15. Briefly, 0.99 g of $FeCl_2$ and 1.62 g $FeCl_3$ were dissolved in 40 ml MQ water under magnetic stirring. Once the reactants were completely dissolved, 10 ml NH_4OH was added to the reaction mixture. 10 min later, 5.01 g NaCit was added and the temperature was raised to, and maintained at, 90°C for 30 min.

The solution was then cooled to room-temperature and transferred to a centrifuge tube. The IO-Cit NPs were precipitated from the reaction mixture by keeping a disc magnet (strength of $\sim$ 677 N) on the side of the tube. The separation was achieved within 3 min. The supernatant was discarded while the IO-Cit NPs were held back by magnetic attraction. The particles were washed 3 times by the addition and removal of MQ water before they were redispersed in a known volume of MQ water for storage (typically 12 ml).

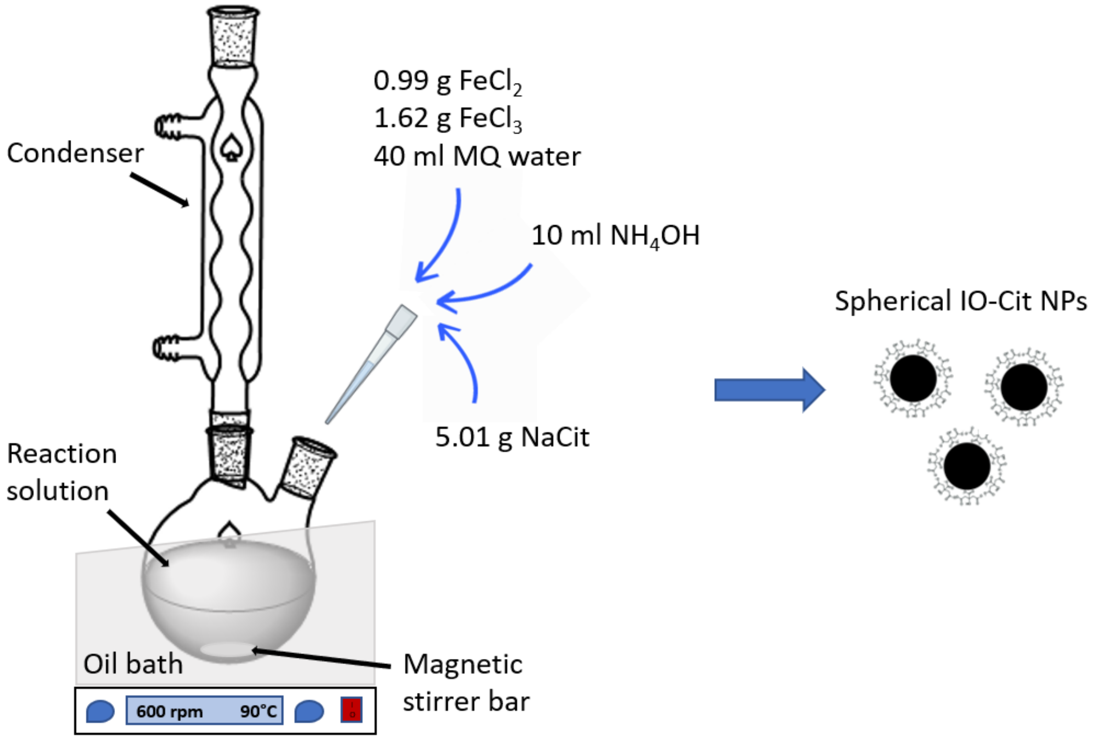

Figure 3.15: Overview of the experimental technique and equipment used in the co-precipitation synthesis of IO-Cit NPs.

3.2.2 Thermal Decomposition

Spherical oleic acid capped iron oxide nanoparticles (IO-OA NPs) were synthesized from the thermal decomposition of iron oleate (FeOl). The FeOl complex was prepared following an adapted protocol from Momtazi et al.[84]. Briefly, 5.395 g $FeCl_3$ and 18.25 g NaOl were dissolved in a mixture of 30 ml MQ water, 70 ml hexane and 40 ml ethanol. The resulting solution was refluxed at 70°C for 4 hours under vigorous stirring. The dark red organic phase was collected and washed 3 times with MQ water, discarding the aqueous phase by the use of a separatory funnel. Finally, hexane was removed from the solution using a rotary evaporator yielding a viscous dark red liquid FeOl complex.

The synthesis protocol of IO-OA NPs from the thermal decomposition of FeOl was adapted and modified from the protocol reported by Ridelman et al[85]. In short, 25 ml (70.3 mmol) of octadecene, 600 μl (1.9 mmol) of oleic acid and 1.6 g (1.78 mmol) of FeOl were added to a two-necked round-bottom flask and stirred under Ar atmosphere. The mixture was heated to 320°C with a heating rate of 3°C/min, and finally maintained for 45 min. A schematic representation of the synthesis protocol is shown in Figure 3.16.

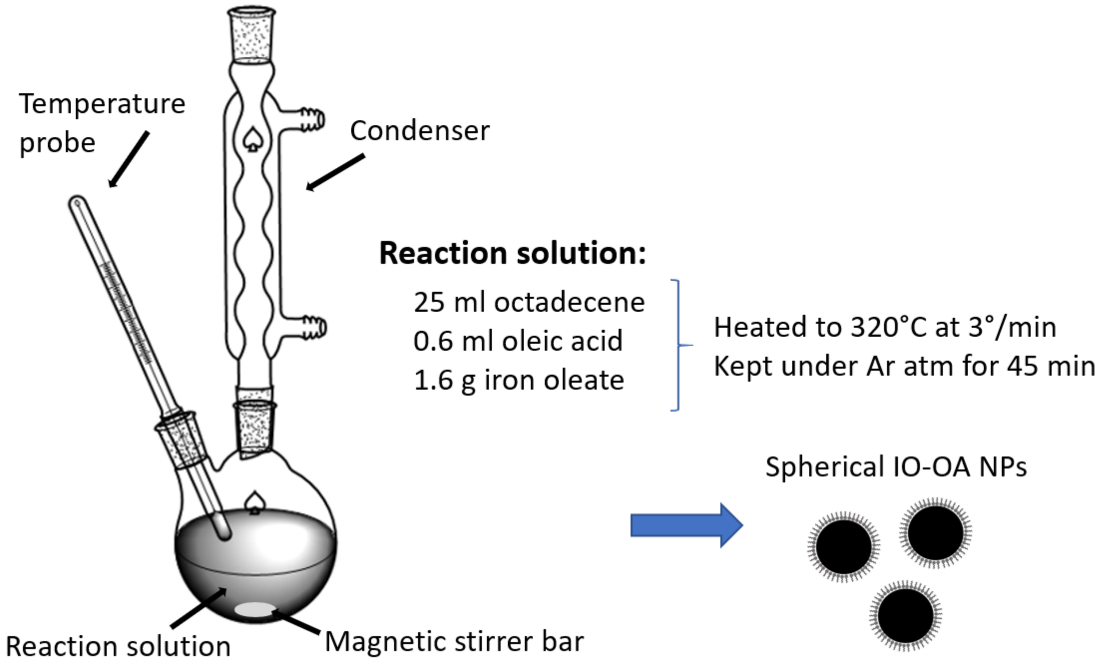

Figure 3.16: Overview of the experimental method and equipment used in the synthesis of IO-OA NPs by thermal decomposition of FeOl.

After the reaction solution had cooled to room temperature, it was transferred to a beaker where the IO-OA NPs were precipitated out by adding 25 ml of hexane, 50 ml of isopropanol and 50 ml of acetone. A disc magnet (strength of ∼ 677 N) was kept below the beaker until all particles were separated from the solution (approximately 10 min) and the supernatant was removed. The particles were washed 3 times with acetone. Finally, the particles were left to dry before they were redispersed in a known volume of toluene (typically 30 ml).

3.3 CTAB Phase Transfer

In order to make the IO-OA NPs dispersible in aqueous solution, a modified CTAB phase transfer procedure was followed based on the protocol reported by Kim et al[75]. 10 ml of the IO-OA NP solution was added to a glass vial and precipitated out by the addition of 40 ml methanol. A disc magnet (strength of ∼ 677 N) was kept under the vial, causing the particles to separate out of the solution. The supernatant was removed while the particles were attached to the bottom of the vial by magnetic attraction. After, the particles were washed with acetone 3 times to ensure that all the solvent was removed, and left to dry. In the mean time, 1.00 g of CTAB and 20 ml of MQ water was added to a single-necked round-bottom flask resulting in a milky-white mixture. The solution was stirred vigorously while heated to 35°C in order to dissolve CTAB, resulting in a transparent liquid. The dried NPs were redispersed in 1 ml of chloroform, and mixed thoroughly by ultra-sonication to ensure that all the particles were included in the mixture. The chloroform solution was then added to the round-bottom flask and stirred magnetically for 30 min to ensure proper mixing with the CTAB solution. The mixture was heated up to 60°C and maintained for 10 min under stirring to evaporate the chloroform. An overview of the described experimental technique and set-up is illustrated in Figure 3.17.

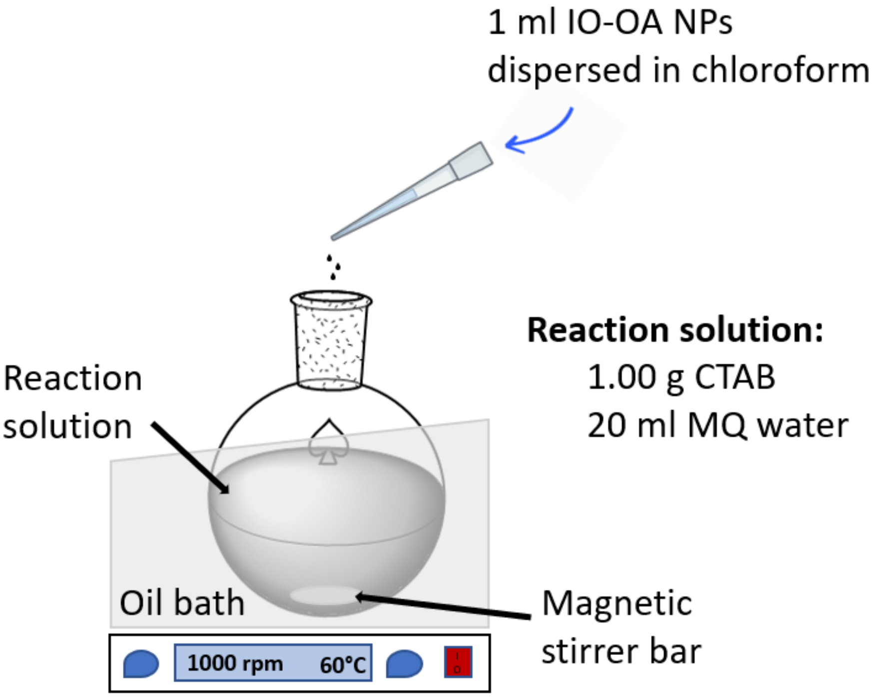

Figure 3.17: Overview of the experimental technique and set-up used in the CTAB phase transfer of IO-OA NPs.

After the reaction solution had cooled to room-temperature, it was transferred to a glass vial and the CTAB-capped iron oxide nanoparticles (IO-CTAB NPs) were precipitated out by the addition of MQ water. A disc magnet (strength of $\sim$ 677 N) was kept on the side of the vial so that the nanoparticles were separated from the liquid, and the supernatant was discarded. The particles were washed 3 times with MQ water to remove any excess CTAB. Finally, the particles were redispersed in a known volume of MQ water (typically 4 ml).

3.4 Synthesis of Fe@Au-Cit Core Shell Nanoarticles

Citrate capped core shell iron gold (Fe@Au-Cit) NPs were synthesized following a modified procedure form Zhou et al[83]. Briefly, 20 ml 1.0 mM $HAuCl_4$ solution was added to a round-bottom flask and heated until boiling (∼ 120°C) under continuous stirring. Then, 20 mg of the IO-Cit NP (prepared as described in Section 3.2.1) dispersed in 10 ml MQ water was rapidly added. After approximately 4-6 min, the reaction solution turned purplish red. After 15 min, the solution was allowed to cool to room-temperature. An overview of the described experimental technique and set-up is shown in Figure 3.18.

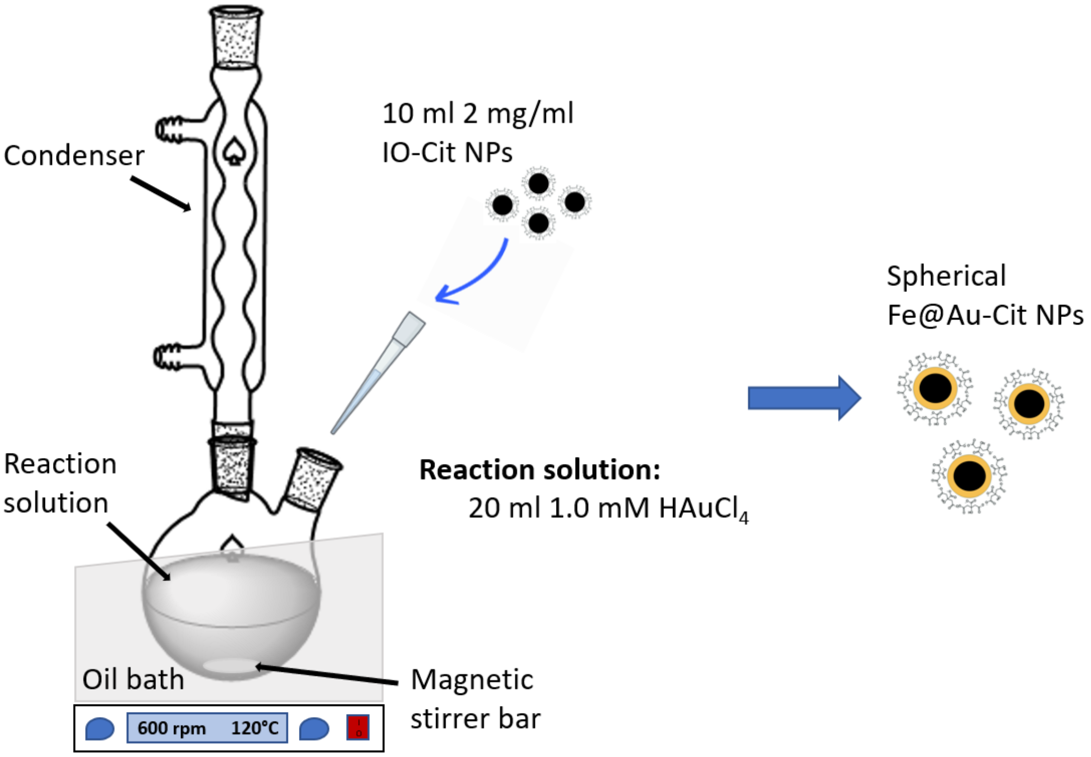

Figure 3.18: Overview of the experimental technique and set-up used in the synthesis of Fe@Au-Cit core shell NPs.

The Au-Cit coated IO NPs were separated from the rest of the reaction solution first by centrifugation (14.5k rpm, 5 min), followed by magnetic separation. The particles were washed 3 times with MQ water, each time separated magnetically from the solution by keeping a disc magnet (strength of ∼ 677 N) on the side of the glass vial in which they were contained. The Fe@Au-Cit NPs separated magnetically within 5 min. After discarding the supernatant the third time, the NPs were redispersed in a known volume of MQ water (typically 5 ml).

3.5 Synthesis of Anisotropic Au Nanostructures

Anisotropic Au nanostructures were synthesized following a modified protocol from Bandyopadhyey et al[86]. In short, 1.2 g CTAB was dissolved in 15 ml MQ water by heating the solution to 35°C under magnetic stirring. Once dissolved, the solution went from having a milky white to a transparent color and 750 μl of 4 mM $AgNO_3$ solution was added. The mixture was left stirring for 15 min before 15 ml of 1.0 mM $HAuCl_4$ solution was added, turning the resulting growth solution yellow. After another 15 min of mixing, the stirring was increased to 1000 rpm and 135 μl of 0.13 M AsA solution was added, resulting in a decolorization of the growth solution. Finally, 96 μl of seed solution was added and after $\sim$ 30 s, the stirring was decreased to 300 rpm. The reaction was left overnight at 35°C. The reaction steps followed in this synthesis are schematically illustrated in Figure 3.19. The aforementioned values for the added reaction parameters will be referred to as the standard values.

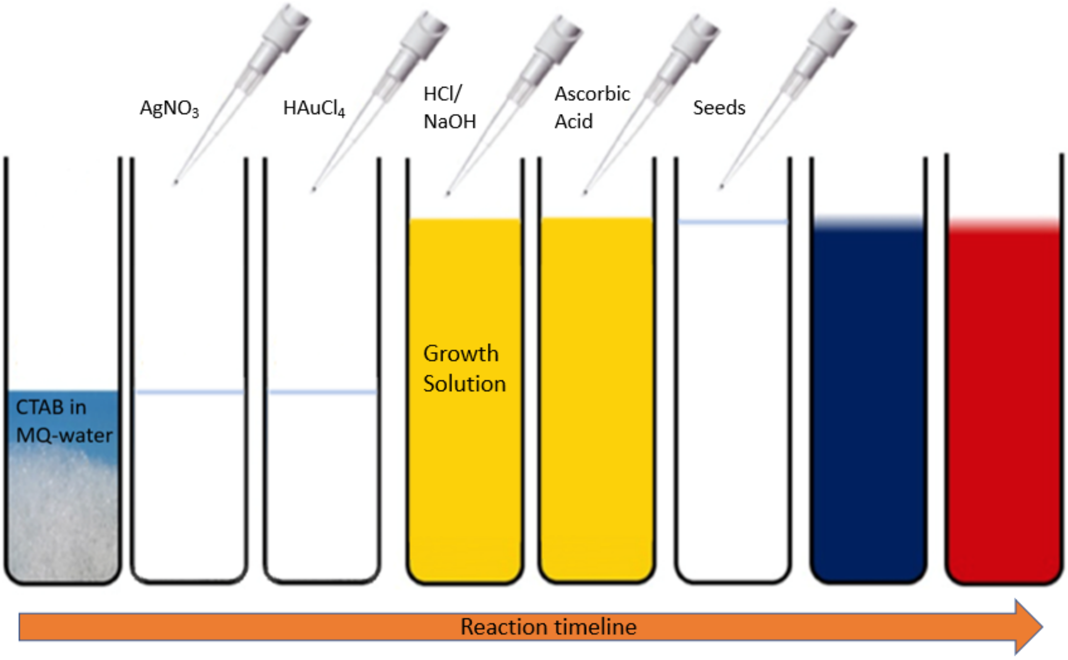

Figure 3.19: Overview of the experimental method used in the synthesis of anisotropic Au nanostructures. *Illustration adapted and modified from ref.* [86].

In several of the conducted experiments, the added amount of the different chemicals was varied in order to examine their effect on the anisotropic growth. The chemicals that were varied was the amount of CTAB, $AgNO_3$ and the pH of the reaction solution. The amount of CTAB ranged from 1.2 g to 2 g, whereas the volume of $AgNO_3$ ranged from 375-2000 μl. The pH of the growth solution was varied from 1.5, by the addition of 0.5 M HCl, to 10.0 by the addition of 0.25 M NaOH. The addition of acid/base was done after the addition of $HAuCl_4$, just before adding the AsA.

A minimum of 12 hours after the seed addition, the reaction solution was transferred to a centrifuge tube and centrifuged twice, each time for 45 min at 11k rpm. After each centrifugation the supernatant was discarded, and the particles were redispersed first in 35 ml, then finally in 5 ml MQ water.

Following the synthesis method of anisotropic Au nanostructures as described above, several different NP solutions were used as seeds. The NP seed solutions included the IO-CTAB NPs, the Fe@Au-Cit NPs, and also Au-Cit NP seeds. In fact, two different protocols were followed in order to synthesize spherical citrate coated Au seed NPs.

3.5.1 Turkevich Seeds

Spherical citrate coated Au NPs were synthesized following a modified protocol from Jimenez-Lamana et al[87] and Wuithschick et al[88]. Briefly, 19.9 ml of 0.25 mM $HAuCl_4$ solution was heated in a round-bottom flask under continuous stirring (500 rpm). Once the solution was boiling, it was maintained for 15 min to ensure an equilibrated mixture. Then, 0.1 ml of 500 mM NaCit solution was added. The reaction solution was maintained for another 5 min before it was allowed to cool to room temperature. Before the particles were used as seeds in the seed-mediated growth, the seed solution was centrifuged for 20 min at 13.4k rpm. The supernatant was discarded and the particles were redispersed in the same volume of MQ water as before the centrifugation.

3.5.2 Jana Seeds

Following a modified protocol from Jana et al[89] also resulted in the synthesis of spherical NaCit coated Au NPs. Briefly, a 20 ml aqueous solution containing 0.25 mM $HAuCl_4$ and 0.25 mM NaCit was prepared in a glass vial. While stirring, 0.6 ml of ice cold 0.1 M $NaBH_4$ solution was added to the solution. The solution turned orange immediately after the injection. These seeds were used in the anisotropic growth solution within 2-5 hours after the injection of $NaBH_4$. By then, the seed solution had turned red, indicating growth of the seed particles.

3.5.3 CTAB Surface Modification of Seed NPs

A CTAB adsorption protocol was performed on the Turkevich Au-Cit and the Fe@Au-Cit NPs in order to change their surface functional groups. The protocol is adapted from the one reported by Lim et al[90]. Briefly, X ml of NP solution (X = 0.5, 1.0, 1.5) was added to a glass vial containing 2 ml of a 2.5 mM CTAB solution. The resulting solution were stirred until fully equilibrated (15 hours). No further cleaning procedure was performed.

3.6 Characterization Techniques

3.6.1 UV-vis Spectroscopy

Ultraviolet-visible (UV-vis) spectroscopy is an experimental technique in which the intensity of light in UV and visible regions is measured as a function of wavelength[91]. The light is passed through the sample of interest, and the amount of light absorbed by the sample is calculated by comparing the intensity of the light before and after having passed through the sample. The result is given as a plot of the sample absorption as a function of the wavelength of the incoming light. Before measuring the absorbance of the nanoparticles, UV-vis spectrometer was first calibrated by establishing a water baseline made from measuring the absorbance of MQ water. This way, only the absorbance caused by the nanoparticles in the solution will be measured. All nanoparticle solutions[2] were diluted in order to obtain an absorbance maximum ≤ 1 in agreement with Beer-Lambert's law[92]. All the measurements were done using an Agilent Cary 60 UV-vis spectrophotometer. The obtained absorbance for each sample was normalized to 1 before presented graphically as a function of the wavelength of the absorbed light.

3.6.2 Scanning (Transmission) Electron Microscopy

The Scanning (Transmission) Electron Microscope (S(T)EM) is a powerful and highly versatile instrument capable of atomic-resolution imaging and nanoscale analysis[93]. The microscopy technique uses an electron gun to generate a high energy beam of electrons (30-600 kV) that is focused through a series of lenses and raster-scanned across a thin sample (<100 nm)[93]. Both scattered and transmitted electrons are detected and their intensity as a function of the position of the electron beam is what generates an image of the specimen. Due to the sample thickness however, the majority of the electrons are transmitted through the sample and thus, the most commonly used S(T)EM detectors are placed after the sample[93].

The S(T)EM images of the various NP populations were taken using a Hitachi High-Tech SU9000 scanning transmission electron microscope that has a resolution down to 0.4 nm. The sample grids were prepared by placing several drops (40-100 μl) of the NP solution on a Formvar carbon-coated copper grid (Electron Microscopy Sciences).

---

[2] that had a concentration leading to an absorbance maximum > 1.

3.6.3 Vibrating-Sample Magnetometer

Vibrating-sample magnetometry is an experimental technique used to measure the magnetic moment of a sample by vibrating the sample perpendicularly while exposed to a uniform magnetizing field[94]. The vibrating-sample magnetometer (VSM) is based on Faraday's law of induction which states that a varying magnetic field generates an electric field[95]. The VSM measures this electric field and calculates the corresponding change in magnetic moment of the sample. This instrument can detect changes as small as 10^{-5} to 10^{-6} emu[96]. In order to measure the magnetic moment of the different NPs, approximately 300-700 μl of the NP solutions were dried to a powder of approximately 0.01-20 mg, depending on the concentration of the solution. All of the measurements were carried out using a MicroMag^{TM} 3900 vibrating sample magnetometer.

3.6.4 Zetasizer

The Zetasizer is an instrument that can measure both the hydrodynamic diameter (H_d) and the zetapotential (ZP) of nanoparticles.

The H_d of nanoparticles in solution is obtained using the dynamic light scattering (DLS) technique. DLS measures the diffusion speed of the particles associated to their Brownian motion, and calculates the corresponding size using the Stokes-Einstein equation:

$$H_d = \frac{kT}{3\pi\eta D}$$

where D is the translational diffusion coefficient, k is Boltzmann's constant, T is the absolute temperature and η the viscosity of the solution. This method assumes that the particles are spherical. For each sample, the H_d is measured thrice and the final result is given along with the standard deviation of the measurements. By taking the square of the standard deviation divided by the square of the average size, the Zetasizer also calculates the polydispersity index (PDI) of the population.

In order to obtain the particle's ZP, the Zetasizer uses Laser Doppler Microelectrophoresis. In this technique an electric field is applied to the nanoparticles in solution which causes them to move with a velocity related to the particles ZP.

Before measuring the hydrodynamic size and ZP of the different NP solutions, the solutions were thoroughly mixed by vortex and ultra-sonication to ensure a homogeneous solution of non-aggregated particles. All of the measurements were done using a Malvern Zetasizer Nano ZS.

Chapter 4

Results and Discussion

In this chapter, the result obtained form the experiments conducted throughout the semester will be presented and discussed. The results can be divided into two main parts; I) Synthesis of seed nanoparticles (NPs) and II) seed-mediated growth of anisotropic nanostructures. Included in the first part are two types of gold (Au) NPs that were synthesized and characterized by scanning (transmission) electron microscopy (S(T)EM) and dynamic light scattering (DLS). As Au is a plasmonic material, the UV-vis absorbance spectra of these NP populations were measured in order to establish the wavelength (λ) at which their local surface plasmon resonance (LSPR) occurs. Also two different types of iron oxide nanoparticles (IO NPs) were synthesized and characterized by S(T)EM, DLS and vibrating sample magnetometry (VSM). From these measurements, both the size distribution and the magnetic hysteresis curves of the two NP populations were obtained. Next, the IO NPs were used as seeds in order to synthesize spherical core shell Fe@Au NPs. These five types of NP populations were used as seeds in the second part of the results, namely the seed-mediated growth of anisotropic nanostructures. In these experiments, both the different types and amount of seed were tested. Finally, also the volume of silver nitrate ($AgNO_3$) and amount of Cetyltrimethylammonium bromide (CTAB) used in the growth solution, as well as the solution's pH, was varied in order to study their impact on the final NP morphology.

4.1 Seed Nanoparticles

4.1.1 Particle Size Distributions and Surface Charge

Jana Au-Cit NPs

Citrate capped gold nanoparticles (Au-Cit NPs) were synthesized following the procedure described in Section 3.5.2. The resulting NP population was examined in S(T)EM, however no particles were found observing the prepared grid. It is possible that the NPs were too small to be detected in S(T)EM. To get a higher resolution view of the sample, high resolution transmission electron microscopy (HRTEM) should be used. According to Jana et al.[89], this synthesis results in particles with an average diameter of 3.5 nm ± 0.7 nm, which would indeed make the NPs difficult to observe through S(T)EM.

Using the Zetasizer instrument (described in Section 3.6.4), the hydrodynamic diameter (H_d) and the zetapotential (ZP) of the Jana Au-Cit NPs were measured to be

136 ± 51 nm and - 35.6 ± 8.3 mV respectively. The population's PDI was calculated to be 0.28 ± 0.08. Looking at the value of the H_d, it is likely that the small size of the seeds introduced difficulties also in the DLS measurements. As indicated by the ZP, the particles are electro-statically stabilized by the negatively charged citrate that surrounds the particles and introduces a repulsion between the citrate coated surfaces. However, if the particles are small enough, aggregation is still energetically favorable, as it will reduce their surface energy (see Section 2.3.2). The large H_d size is thus likely due to aggregated clusters of NPs that are measured as a single particle by the Zetasizer.

Turkevich Au-Cit NPs

Following the procedure given in Section 3.5.1, another Au-Cit NP population was synthesized. The resulting particles were imaged by S(T)EM and their size distribution calculated by measuring the area of 200 particles using the ImageJ software. The results are shown Figure 4.20. The Au-Cit population had an average diameter of 17 ± 2 nm, and a PDI of 0.35. The PDI is calculated by taking the square of the standard deviation divided by the square of the mean, using the same method as the Zetasizer.

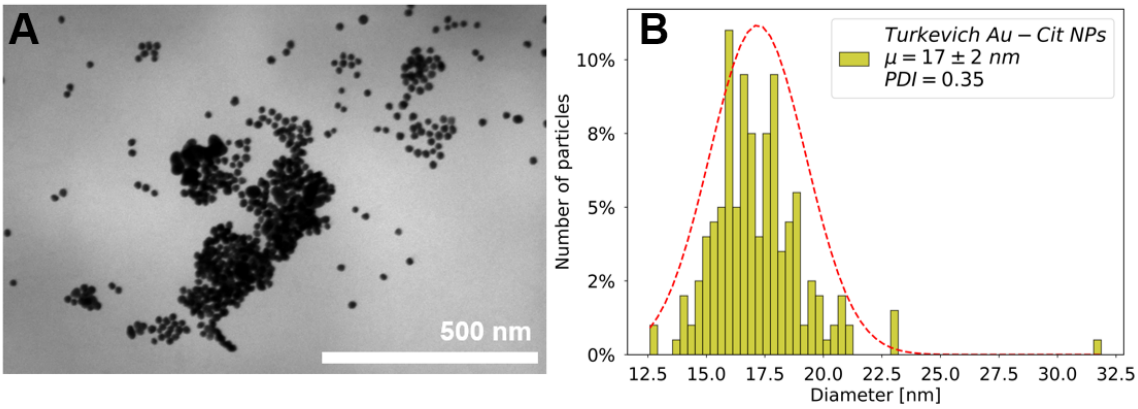

Figure 4.20: Representative scanning (transmission) electron microscope (S(T)EM) image and size distribution of the Turkevich citrate capped gold nanoparticles (Au-Cit NPs).

The H_d, ZP and PDI for the Turkevich Au-Cit NPs are given in Table 4.2. The average diameter of the Turkevich Au-Cit population as measured from the S(T)EM image ($\mu = 17 \pm 2$ nm), differ significantly from the H_d of the same population ($H_d = 43 \pm 1$ nm). The difference is likely due to the different measurements techniques applied in the two cases. The hydrodynamic size is measured on particles dispersed in aqueous solution and includes the size of the hydration layer of the particles. The particles viewed by S(T)EM, on the other hand, are dried and the measured size includes nothing more than the bare NP. However, the water removal induces particle aggregation resulting in the NP clusters seen in the S(T)EM image of the population. Yet, enough individual particles could be distinguished in order to obtain a representative size distribution.

Table 4.2: The hydrodynamic diameter (H_d), zetapotential (ZP) and polydispersity index (PDI) for the Turkevich citrate capped gold nanoparticle (Au-Cit NP) population as measured by the Zetasizer.

Nanoparticle Population	H_d [nm]	ZP [mV]	PDI
Turkevich Au-Cit	43 ± 1	- 40.4 ± 0.4	0.60 ± 0.04

When comparing the two different Au-Cit populations, it is the Jana seeds that shows the highest H_d, even though the Turkevich seeds are estimated to be around five times the size of the Jana seeds. As discussed in the previous section, this is likely due to NP aggregation in the Jana seed population. As the magnitude of the ZP is a measure of the degree of electrostatic repulsion between the NPs in solution, a higher ZP implies a more stable NP population[97]. Thus, the higher absolute value of the ZP of the Turkevich Au-Cit also indicates that this population is less prone to aggregation than the Jana seed population.

Following the procedure described in Section 3.5.3, CTAB was adsorbed onto the surface of the Turkevich Au-Cit NPs. The procedure was performed in three parallels with increasing amounts of citrate capped particles. Consequently, three NP solutions with different Au-Cit NPs concentrations were obtained. Both the H_d and the ZP were measured before and after the CTAB adsorption and are given in Table 4.3. Here, X denotes the amount of Turkevich Au-Cit NPs that was functionalized following the protocol. Although it is unsure exactly how CTAB interacts with the negatively charged Au-Cit surface, after having performed the adsorption protocol the ZP of

Table 4.3: The hydrodynamic diameter (H_d), zetapotential (ZP) and polydispersity index (PDI) for the Turkevich citrate capped gold nanoparticle (Au-Cit NP) populations before and after the cetyltrimethylammonium bromide (CTAB) adsorption procedure, for three different NP concentrations. X denotes the amount of Turkevich Au-Cit NPs that was used in the adsorption protocol. The data was measured using the Zetasizer instrument.

Samples	X [ml]	Before Adsorption		After Adsorption	
		H_d [nm]	ZP [mV]	H_d [nm]	ZP [mV]
Au-Cit-CTAB_0.5	0.5	43 ± 1	- 40.4 ± 0.4	59 ± 3	93.8 ± 3.4
Au-Cit-CTAB_1.0	1.0			50 ± 1	45.5 ± 2.0
Au-Cit-CTAB_1.5	1.5			50 ± 1	44.2 ± 2.6

the particles changes from negative to positive and their H_d size increases. These changes were also observed in the experiments of Lim et al.[90] and are indications of a successful change of the NPs's surface layer (see Section 2.4). The ZP of the Au-Cit-CTAB_0.5 is much higher than the other two parallels. This can be due to the presence of excess, free CTAB in the solution. If the ratio of NPs to free CTAB in the solution is high, it could reduce the LSPR signal the particles. There is not much of a difference in the data obtained for the 1.5 and 1.0 parallels. In order to surface functionalize the most particles per procedure, 1.5 ml of nanoparticle solution was used in the following adsorption protocols.

IO-Cit NPs

Following the procedure described in Section 3.2.1, citrate capped IO NPs (IO-Cit NPs) were synthesized and imaged using S(T)EM. The result is shown in Figure 4.21A. Using the ImageJ software on the S(T)EM image, the area of 356 particles was measured in order to calculate the size distribution of the population given in Figure 4.21B. The average diameter of the particles was found to be 9 ± 2 nm, with a PDI of 0.46.

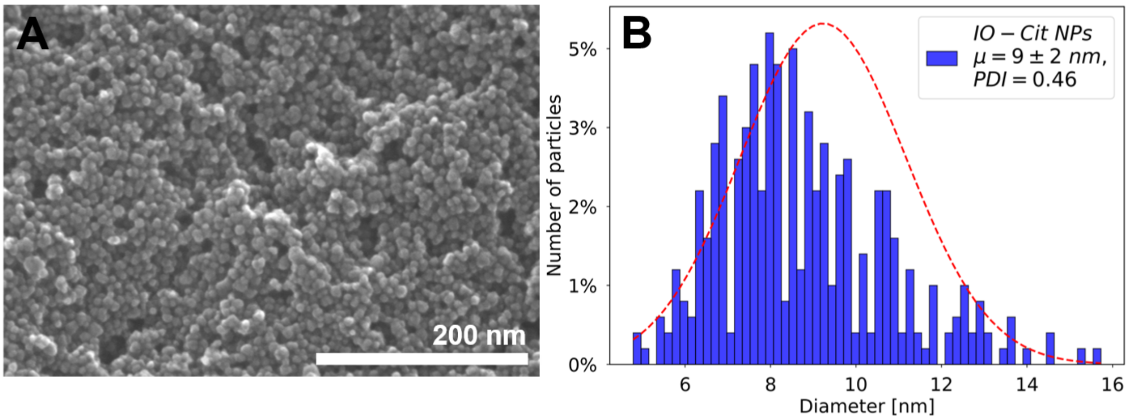

Figure 4.21: Representative scanning (transmission) electron microscope (S(T)EM) image and size distribution of the citrate capped iron oxide nanoparticles (IO-Cit NPs), synthesized by co-precipitation.

The H_d and ZP for the IO-Cit NPs, as well as the population's PDI, are given in Table 4.4. As expected, the H_d of the population is much larger than the size measured from the S(T)EM image. Seen from the absolute value of the ZP of the two populations, the IO-Cit NPs show less electro-static stability than the Turkevich Au-Cit NPs. As a consequence, the IO-Cit NPs are more prone to aggregation when dispersed in solution. The large H_d value is thus likely not only due to the hydration layer, but a result of aggregated clusters of IO NPs that were measured as a single particle by the Zetasizer. The negative value of the ZP confirms the citrate surface layer of the particles.

Table 4.4: The hydrodynamic diameter (H_d), zetapotential (ZP) and polydispersity index (PDI) for the citrate capped iron oxide nanoparticle (IO-Cit NP) population that was synthesized by co-precipitation. The data was measured by the Zetasizer.

Nanoparticle Population	H_d [nm]	ZP [mV]	PDI
IO-Cit NP	97 ± 7	- 39.2 ± 0.2	0.49 ± 0.06

IO-OA NPs

Before the synthesis of the thermal decomposition IO NPs could be performed, the iron precursor had to be synthesized. Liquid iron oleate (FeOl) was synthesized following the procedure described in Section 3.2.2. Figure 4.22 shows the final product of dark reddish orange FeOl and illustrates its viscous nature. However, when used in previous work[19], the FeOl was even more viscous, indicating that perhaps not all the solvent was evaporated when using the rotavapour. It is likely due to residual water, as it has a higher boiling point than both hexane (69°C) and ethanol (78.37°C).

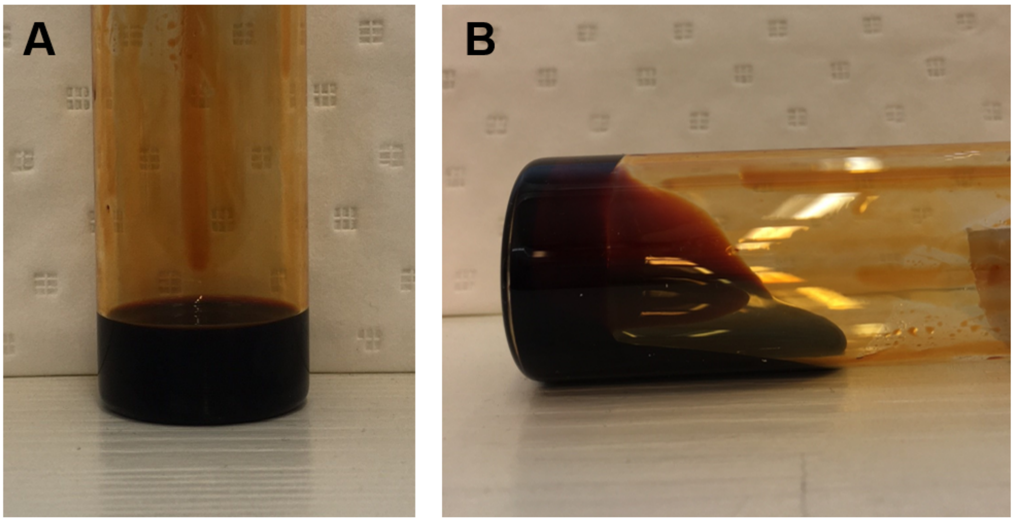

Figure 4.22: Photos of the final iron oleate (FeOl) product in upright (A) and horizontal (B) position, illustrating its viscous nature.

Once the FeOl had been synthesized, it was used as the iron precursor in the thermal decomposition protocol when producing the oleic acid capped IO NPs (IO-OA NPs). The procedure is described in Section 3.2.2. The resulting NP population was imaged using S(T)EM and is shown in Figure 4.23A. The area of 304 particles was measured using the ImageJ software on this image. From these measurements, the size distribution of the population was calculated and is shown in Figure 4.23B. The average diameter of the particles was measured to be 13 ± 1 nm, resulting in a PDI of 0.27 for the IO-OA NP population. This value is lower than the PDI obtained for the IO-Cit NP population, indicating that the particles synthesized by thermal decomposition have a more uniform and monodispersed size distribution than the ones synthesized by co-precipitation, as expected from literature[98]. The IO-OA NPs were not characterized by DLS as the cuvettes used in the Zetasizer instrument are not equipped to measure on particles dispersed in organic solvents.

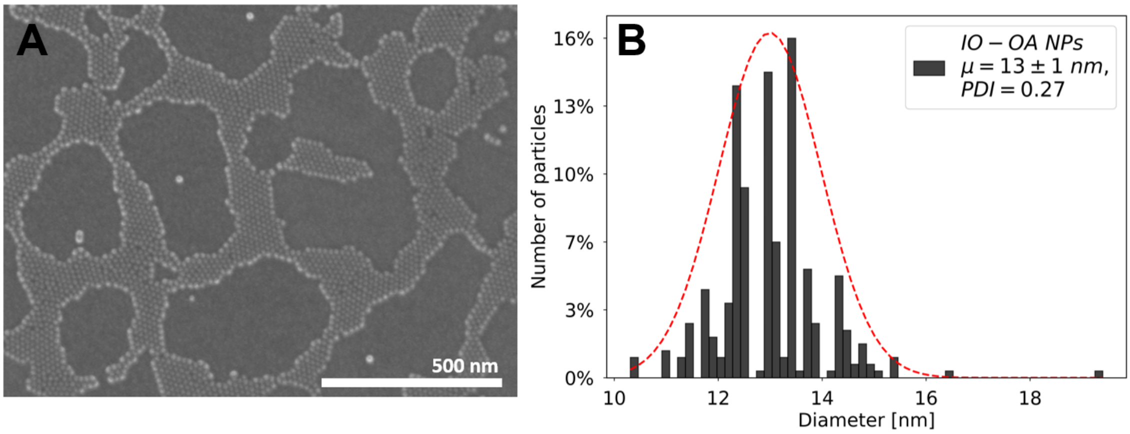

Figure 4.23: Representative scanning (transmission) electron microscope (S(T)EM) image and size distribution of the oleic acid capped iron oxide nanoparticles (IO-OA NPs), synthesized by thermal decomposition of iron oleate (FeOl).

IO-CTAB NPs

In order to make the IO-OA NP dispersible in water, a CTAB phase transfer protocol was performed on the particles, as described in Section 3.3. The resulting IO-CTAB NPs were imaged by S(T)EM and are shown in Figure 4.24. As can be seen from the images, the IO NPs appear to have formed some kind of spherical aggregates of various sizes, likely held together by the CTAB capping agent. This can indicate that during

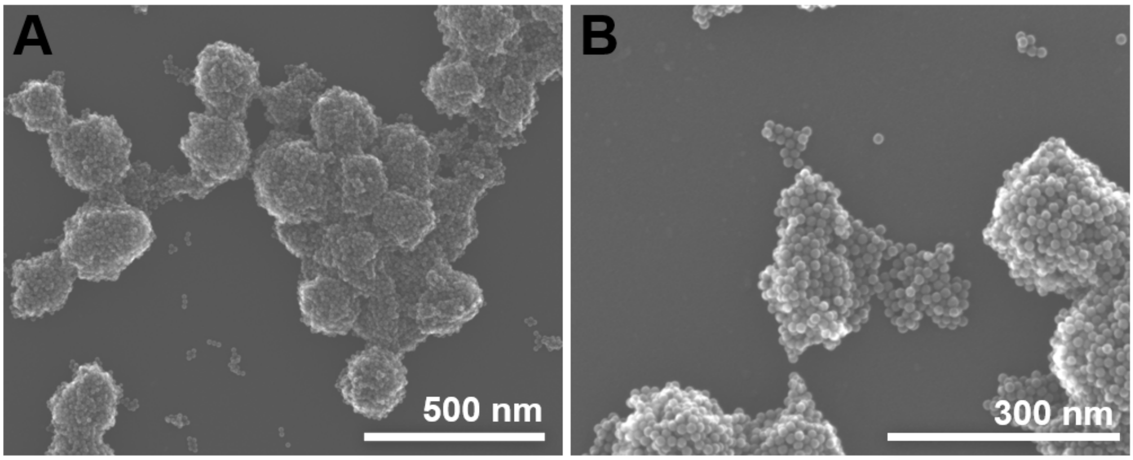

Figure 4.24: Representative scanning (transmission) electron microscope (S(T)EM) images of the cetyltrimethylammonium bromide-capped iron oxide nanoparticles (IO-CTAB NPs) with a scale bar of (A) 500 nm and (B) 300 nm.

the phase transfer, it is actually not each individual NP that is coated with CTAB, but that the CTAB can encapsulate whole clusters.

The H_S, ZP and PDI obtained from the IO-CTAB NP population are given in Table 4.5. When comparing the two aqueous IO NP populations, it is clear that they have very different properties. The IO-CTAB NPs have a larger hydrodynamic size, a positive ZP due to its CTAB surface layer, and are more monodispersed than the IO-Cit NPs. As the phase transfer procedure only affect the surface properties of the IO NPs, their size as measured from S(T)EM do not change after the CTAB coating. Compared to the co-precipitation IO-Cit NPs, the thermal decomposition IO-CTAB NPs have a average diameter that is 4 nm larger. However, their hydrodynamic sizes differ by 187 nm. This can be due to the aggregated clusters, as observed in the STEM images in Figure 4.24, that can have been measured as one particle by the Zetasizer.

Table 4.5: The hydrodynamic diameter (H_d), zetapotential (ZP) and polydispersity index (PDI) of the the cetyltrimethylammonium bromide-capped iron oxide nanoparticle (IO-CTAB NP) population, measured by the Zetasizer.

Nanoparticle Population	**H_d [nm]**	**ZP [mV]**	**PDI**
IO-CTAB NPs	284 ± 6	37.4 ± 1.1	0.40 ± 0.02

Fe@Au-Cit NPs

Following the protocol as described in Section 3.4, citrate capped Fe@Au NPs were synthesized using IO-Cit NPs as seeds. Figure 4.25 show the representative S(T)EM image taken of the population (A) and their measured size distribution (B). The Fe@Au-Cit NPs had an average diameter of 8 ± 2 nm, and a PDI of 0.52. Comparing

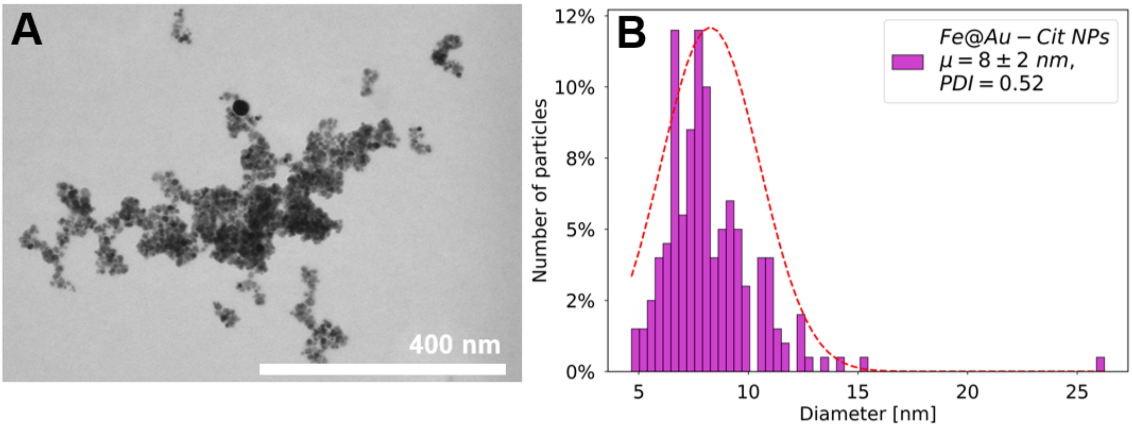

Figure 4.25: Representative scanning (transmission) electron microscope (S(T)EM) image and size distribution of the citrate capped core shell iron gold nanoparticles (Fe@Au-Cit NPs).

with the diameter of the uncoated IO-Cit NPs, the two populations have similar sizes implying that the gold layer is thin.

The measured values of the H_d, the ZP and the PDI of the Fe@Au-Cit NPs are given in Table 4.6. Compared to the data given in Table 4.4, the H_d of the Fe@Au-Cit particles are larger than that of the IO-Cit NPs, suggesting that the IO-Cit NP have been coated with gold. The data also indicates that the population has become less stable after the coating as the the absolute value of the ZP decreases. In the Fe@Au-Cit synthesis, it is the citrate surface layer of the IO-Cit NPs that reduces the Au precursor resulting in the coating of the particles. Thus, the decrease in electrostatic repulsion could be due a decreased concentration of citrate as some of it will have been used in reduction of the Au precursor.

Table 4.6: The hydrodynamic diameter (H_d), zetapotential (ZP) and polydispersity index (PDI) of the citrate capped core shell iron gold nanoparticles (Fe@Au-Cit NPs), measured by the Zetasizer.

Nanoparticle Population	**H_d [nm]**	**ZP [mV]**	**PDI**
Fe@Au-Cit	110 ± 2	- 28.6 ± 0.4	0.33 ± 0.05

The CTAB adsorption procedure, described in Section 3.5.3, was performed on two different Fe@Au-Cit populations, using 1.5 ml NP solution. One of which was synthesized using the standard procedure as reported in Section 3.4, i.e. 20 mg IO-Cit NP seeds (C = 2 mg/ml) and a 1.0 mM concentration of the $HAuCl_4$ solution. This batch of NPs will be referred to as Fe@Au-Cit (20-1.0). The second was synthesized using 15 mg IO-Cit NP seeds (C = 1.5 mg/ml) and a 0.75 mM concentration of the $HAuCl_4$ solution. This second batch of NPs will be referred to as Fe@Au-Cit (15-0.75). In both batches, the seed to gold ratio were the same. This ratio was found to be optimal for synthesizing Fe@Au NPs exhibiting both LSPR and superparamagnetic behavior[99]. The H_d and the ZP of the two populations before and after the CTAB adsorption are given in Table 4.7. CTAB is a larger molecule than citrate, yet the H_d is decreasing

Table 4.7: The hydrodynamic diameter (H_d), zetapotential (ZP) and polydispersity index (PDI) of the citrate capped core shell iron gold nanoparticles (Fe@Au-Cit NPs) before and after cetyltrimethylammonium bromide (CTAB) adsorption. The data was measured by the Zetasizer.

Nanoparticle Seeds	**Before Adsorption**		**After Adsorption**	
	H_d [nm]	**ZP [mV]**	**H_d [nm]**	**ZP [mV]**
Fe@Au-Cit-CTAB (20-1.0)	110 ± 2	- 28.6 ± 0.4	81 ± 1	42.3 ± 1.6
Fe@Au-Cit-CTAB (15-0.75)	124 ± 2	- 20.5 ± 0.5	89 ± 2	42.4 ± 0.6

after the adsorption. This might be due to smaller free CTAB micelles in the solution that are measured as particles by the Zetasizer, resulting in a smaller average size of the population.

In a separate experiment, the IO-CTAB NPs were also coated with gold, resulting in CTAB capped core shell iron gold NPs (Fe@Au-CTAB). This work is presented in Appendix Fe@Au-CTAB NPs.

4.1.2 Plasmonic Properties

The absorbance of the gold containing seed NPs were measured using a UV-vis spectrometer (described in Section 3.6.1). The resulting spectra are shown in Figure 4.26.

The UV-vis spectra of the Jana Au-Cit population (Figure 4.26A, orange), shows an absorption peak at $\lambda = 507$ nm, which is the LSPR wavelength of the NPs. The absorption spectra of the Turkevich Au-Cit seeds (Figure 4.26A, yellow) have a LSPR wavelength of 523 nm. The LSPR wavelength for spherical Au NPs with a diameter of 20 nm is typically reported as 520 nm[33] (see Figure 2.3). When comparing the two different Au-Cit populations, it is clear that the LSPR of the Turkevich seeds has a higher intensity and is red-shifted as compared to the LSPR peak of the Jana seeds. This is as expected when considering the size difference between the two populations. Generally, smaller NPs show less distinct LSPR at shorter wavelengths[33]. Furthermore, there is a shoulder peak present in the spectra of the Turkevich seeds at $\lambda \sim 750$ nm that is not seen in the spectra of the Jana seeds. This indicates the existence of NPs with different sizes and/or shapes in the Turkevich seeds, and that the Jana seeds consist of a more monodispersed population. This is also what is indicated by the calculated PDI from the Zetasizer measurements for the Jana and Trukevich seeds.

The UV-vis absorption spectra for the Turkevich Au-Cit populations before and after CTAB adsorption, for three different NP concentrations, is plotted in Figure 4.26B. The spectra of the seeds before and after the CTAB adsorption share the same form, although the Au-Cit-CTAB_0.5 sample has a reduced absorption maxima compared to the other samples. This is likely due to the low NP/CTAB ratio of this sample. These UV-vis spectra indicate that the CTAB adsorption do not affect the plasmonic properties of the Au NPs when performing the CTAB adsorption on 1.0 ml or 1.5 ml Au-NPs.

The UV-vis absorption spectra of the magneto-plasmonic Fe@Au-Cit seeds is shown in Figure 4.26C. This population has a LSPR peak at 535 nm. Furthermore, comparing the absorption spectra of the Fe@Au-Cit NPs to the spectra of the Jana Au-Cit NPs, the former could be expected to show the largest LSPR when only considering the average size of the two populations. However, this is not the case, indicating that the gold shell of the Fe@Au-Cit seeds is thin.

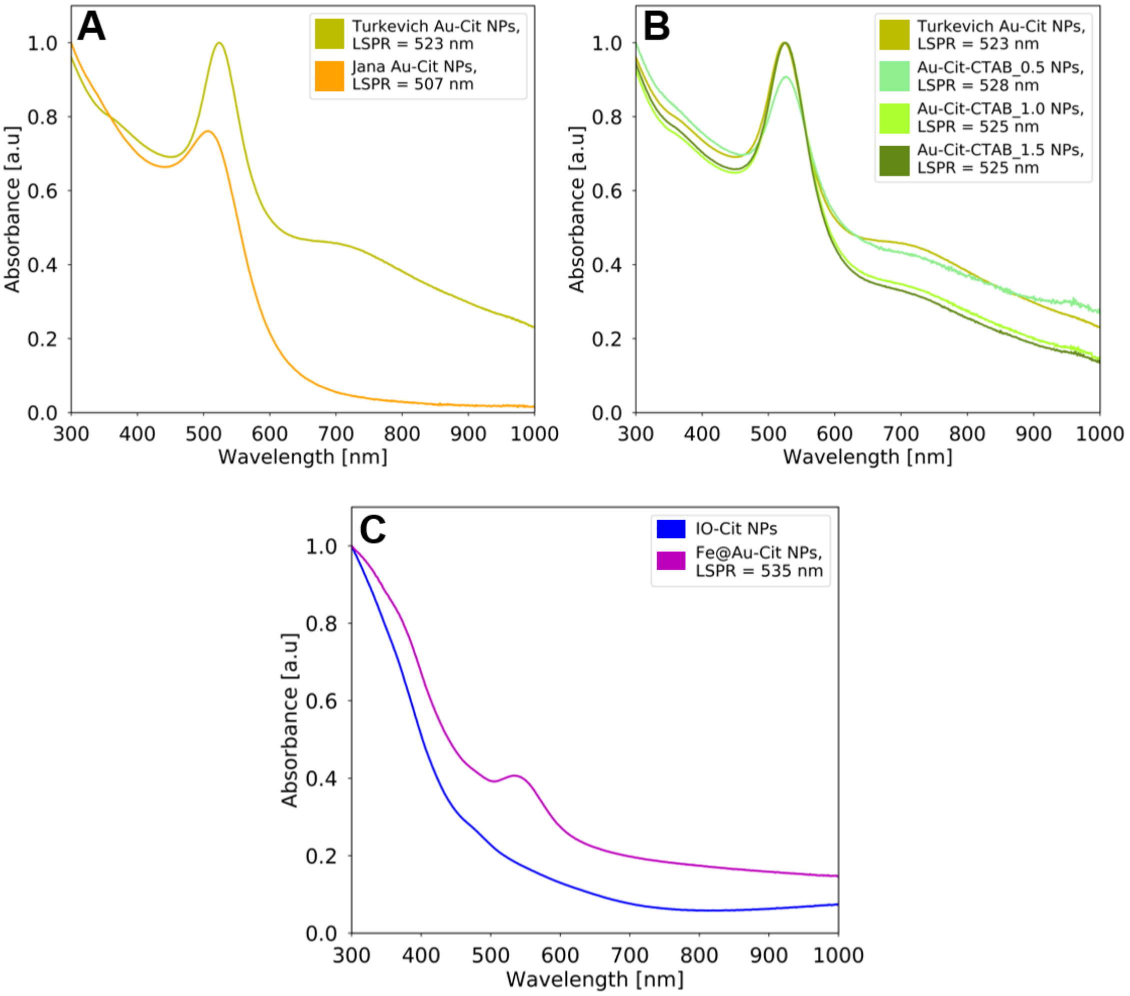

Figure 4.26: Normalized UV-vis absorbance spectra of the plasmonic NP seeds. **A**: The Jana (orange) and the Turkevich (yellow) citrate capped gold nanoparticles (Au-Cit NPs), **B**: The Turkevich Au-Cit NPs before and after cetyltrimethylammonium bromide (CTAB) adsorption for the three different particle concentrations, **C**: The citrate capped iron oxide nanoparticles (IO-Cit NPs) with (purple) and without (blue) Au coating.

4.1.3 Magnetic Properties

The magnetic hysteresis curves of the iron containing seed NPs were measured using VSM (described in Section 3.6.3) and are given in Figure 4.27. All the hysteresis curves exhibit the same characteristic shape as that of superparamagnetic materials, i.e. having zero magnetic moment for zero magnetic field (see Figure 2.1). However, the saturation magnetization (M_S) vary greatly between the populations. The seed population with the highest M_S is the IO-Cit NPs with the value of 50.35 emu/g. This value is of the same magnitude as the M_S reported in literature for magnetite nanoparticles synthesized via the chemical co-precipitation method[100].

The fact that the thermal decomposition IO-OA NPs have a M_S of 28.35 emu/g, is unexpected. According to what is reported in literature[101], and also in agreement with the findings of previous work[19], the M_S of such particles is expected to be in the range of 62-90 emu/g. It should be mentioned that the cleaning procedure (as described in Section 3.2.2) had to be performed twice as the IO-OA NPs did not precipitate out of toluene as easily as expected[102]. This suggests that the IO-OA NP solution could have contained residual solvent from the synthesis procedure. When measured by the VSM, the magnetic moment of the NPs are given in emu. In order to represent the magnetic moment as emu/g, the measured value is divided by the weight of the sample. This way, only $\sim$ 5 mg of dried NPs are necessary in order to measure the magnetic moment of the population. However, leftover impurities or residual solvent from the synthesis procedure would greatly impact the M_S as it would make the mea-

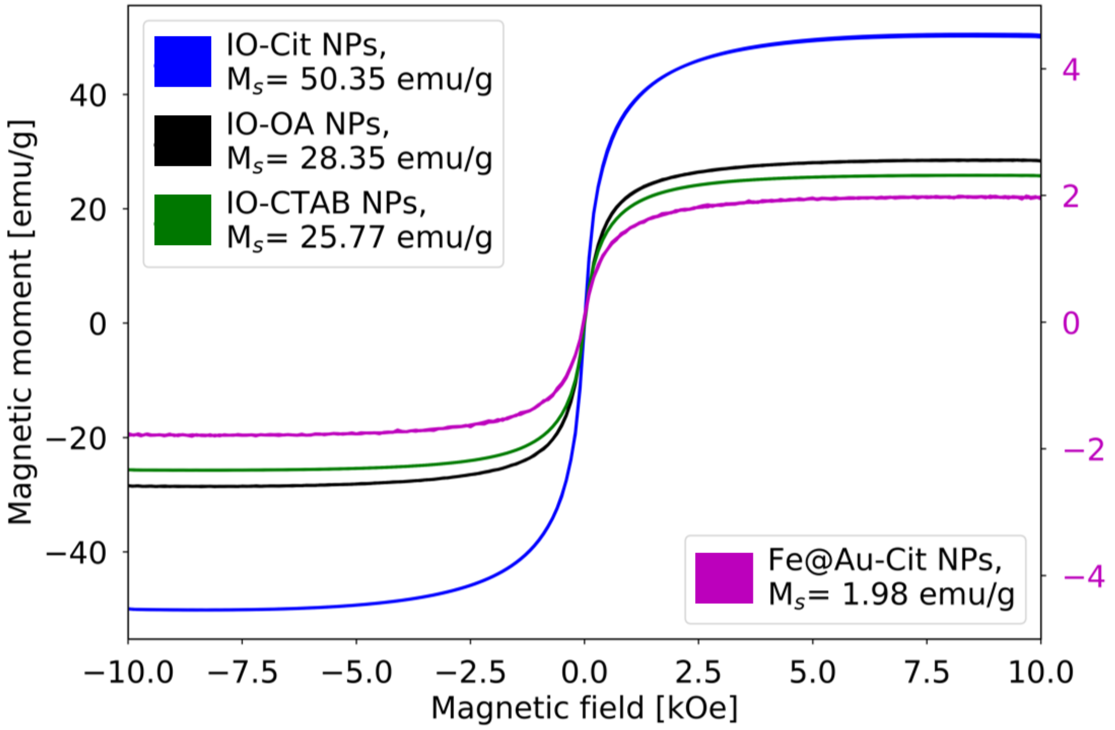

Figure 4.27: Magnetic hysteresis curves and saturation magnetization (M_S) of the iron containing seed NPs: the citrate capped iron oxide nanoparticles (IO-Cit NPs, blue), the oleic acid capped iron oxide nanoparticles (IO-OA NPs, black), the cetyltrimethylammonium bromide capped iron oxide nanoparticles (IO-CTAB NPs, green), and the citrate capped core shell iron gold nanoparticles (Fe@Au-Cit NPs, purple). The data was measured by vibrating sample magnetometry (VSM).

sured weight of the sample higher than the weight of IO NPs present in the sample. This is likely the reason why the calculated M_S (in emu/g) of the IO-OA NP population is lower than expected.

After the phase transfer of the IO-OA NP population, the M_S of the population is reduced from 28.35 to 25.77 emu/g. As previously discussed, the IO-OA NPs show a lower M_S than what is expected from literature, yet the M_S value of the IO-CTAB NPs is in the expected range[103]. This is another indication that the low M_S of the IO-OA NPs is due to some leftover impurities or residual solvent from the synthesis procedure that can have been removed during the phase transfer procedure.

When comparing the magneto-plasmonic NP population to the IO NPs, it appears that the presence of Au drastically reduces the M_S. This is expected, as the plasmonic material only contributes to the NP mass, and not its magnetic moment. This is further confirmed by the results of Bandyopadhyay et al.[104]

4.2 Seed-Mediated Growth of Anisotropic Nanoparticles

The seed-mediated growth of anisotropic nanostructures was carried out as described in Section 3.5, using the five different types of NP seeds that were presented in the previous section: The Jana Au-Cit, the Turkevich Au-Cit, the Fe@Au-Cit, the IO-Cit NP, and the IO-CTAB NP seeds. A summary of the seed properties is given in Table 4.8. The results obtained from using each of the different seeds in the anisotropic growth protocol will be presented and discussed in this section.

Table 4.8: Summary table showing the average diameter (μ), hydrodynamic diameter (H_d), zetapotential (ZP), local surface plasmon resonance (LSPR) and saturation magnetization (M_S) of all the seed nanoparticles.

Seed Population	**μ [nm]**	**H_d [nm]**	**ZP [mV]**	**LSPR [nm]**	**M_S [emu/g]**
Jana Au-Cit	-	-	- 35.6 ± 8.3	507	N.A
Turkevich Au-Cit	17 ± 2	43 ± 1	- 40.4 ± 0.4	523	N.A
Fe@Au-Cit	8 ± 2	110 ± 2	- 28.6 ± 0.4	535	1.98
IONPs-Cit	9 ± 2	97 ± 7	- 39.2 ± 0.2	N.A	50.35
IONPs-CTAB	13 ± 2	284 ± 6	37.4 ± 1.1	N.A	25.77

N.A = Not applicable

4.2.1 Jana Seeds

Two sets of experiments were conducted using the Jana Au-Cit NPs as seeds in which two different reaction parameters were varied in order to study their effect on the final morphology of the anisotropic particles.

In the first set of experiments, the amount of CTAB in the growth solution was increased from 1.2 g to 1.5 g to 2.0 g, while standard values were used for the other reaction parameters as reported in Section 3.5. Figure 4.28A show the measured UV-vis absorption spectra of the NPs before and after the seed-mediated growth. From the intensity of the LSPR peaks, it is clear that Au has grown on the seeds in all three experiments. There is not much of a change in the form of the spectra, and the variation of the LSPR wavelength is only 3 nm. The population grown in 1.2 g CTAB show the highest absorbance.

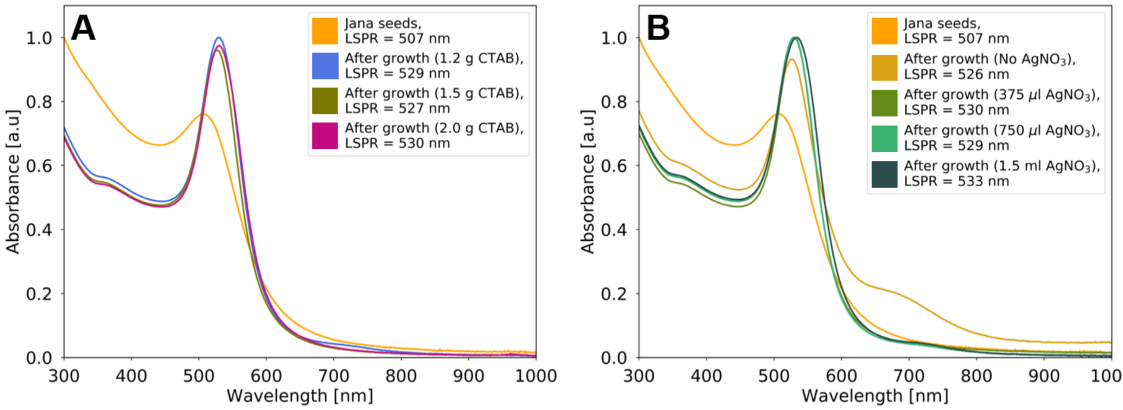

Figure 4.28: Normalized UV-vis absorption spectra for the Jana citrate capped gold (Au-Cit) seeds before and after seed-mediated Au growth, (A) having varied the amount of cetyltrimethylammonium bromide (CTAB) and (B) having varied the amount of $AgNO_3$ in the growth solution.

In the second set of experiments using the Jana Au-Cit seeds, it was the volume of $AgNO_3$ that was varied. 4 NP populations were synthesized in which 0, 0.375, 0.750, and 1.5 ml of $AgNO_3$ was used respectively. Figure 4.28B show the measured UV-vis absorption spectra of the NPs before and after the seed-mediated growth. After the growth procedure there is a clear enlargement of the LSPR peak of all the samples, indicating the successful heterogeneous Au nucleation and growth. The peak has also red-shifted > 20 nm in all samples which is another indication that the particles have become larger after the growth. In the spectra of the NPs that were grown without any $AgNO_3$, a shoulder peak is present at $\lambda \sim 700$ nm, very similar to the one observed for the Turkevich Au-Cit (Figure 4.26B). This could be an indication that there are NPs of several different shapes and sizes present in that population. This is not unexpected as $AgNO_3$ is known to induce shape control, promoting monodispersity[105]. The three other samples, synthesized with 375μl, 750μl and 1.5 ml of $AgNO_3$, show very similar absorbance spectra. Therefore, S(T)EM was performed on the samples synthesized using the extreme values of $AgNO_3$. The representative S(T)EM images of the two populations, shown in Figure 4.29, confirm what was indicated in the UV-vis spectra.

The sample synthesized without any $AgNO_3$ have NPs of various shapes and sizes, while the sample with 1.5 ml of $AgNO_3$ show more monodispersed, oval morphologies with sizes of ∼ 30 nm. Due to the low level of anisotropy, the Jana seeds were replaced by the Turkevich seeds in the following experiments.

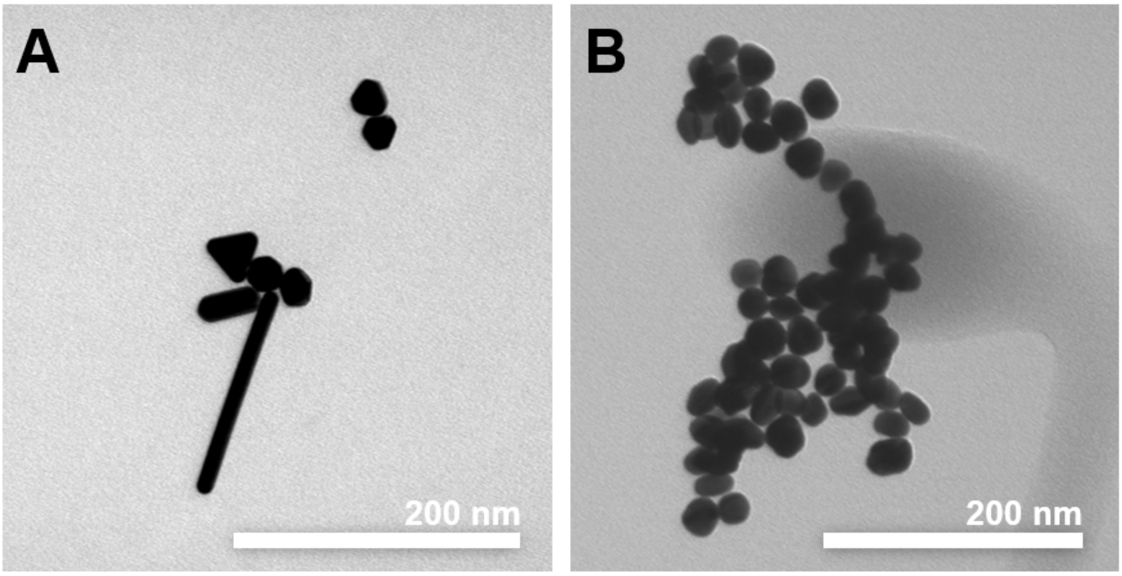

Figure 4.29: Representative scanning (transmission) electron microscope (S(T)EM) images of the nanoparticles synthesized from seed-mediated Au growth on the Jana citrate capped gold (Au-Cit) seeds using (A) 0 ml and (B) 1.5 ml of $AgNO_3$.

4.2.2 Turkevich Seeds

Five experiments were conducted using the Turkevich seeds in the seed-mediated growth procedure. In order to examine the effect of surface coating and charge, three of the experiments were conducted using the three different Au-Cit-CTAB seeds (see Table 4.3). In order to add the same amount of seeds as in the standard procedure, the seed volumes of the three populations had to be adjusted. Consequently, when using the Au-Cit-CTAB_0.5, Au-Cit-CTAB_1.0 and the Au-Cit-CTAB_1.5 population as seeds, 480, 288 and 224 μl of the respective seed solutions were added. The two other experiments were performed using citrate capped Au seeds, one in which the standard procedure was followed, and in the second the amount of CTAB in the growth solution was increased to 1.5 g.

The absorbance spectra of the five NP populations before and after the seed-mediated growth are shown if Figure 4.30A and 4.30B respectively. Comparing the spectra of the different samples, all in which there was more CTAB present in the growth solution than what is used in the standard procedure, show similar curves.

This indicates that whether the NPs have CTAB adsorbed on their surface prior to the seed-mediated growth, or if there is excess CTAB in the growth solution, does not affect the optical properties of the resulting seed-mediated particles. It is possible that the excess CTAB added into the growth solution adsorb onto the surface of the negatively charged Au-Cit seeds in a similar fashion as in the CTAB adsorption protocol performed before adding the seeds. This is also confirmed by the representative S(T)EM images of the populations, shown in Figure 4.31, in which no significant difference can be observed between the samples using the CTAB adsorption seeds (a-c) and the sample using the citrate seeds with excess CTAB in the growth solution (d). All four populations consist of oval shaped particles with sizes in the range of ∼ 100-150 nm. The particles synthesized following the standard procedure also show similar morphologies (Figure 4.31e), though their absorption peak is higher.

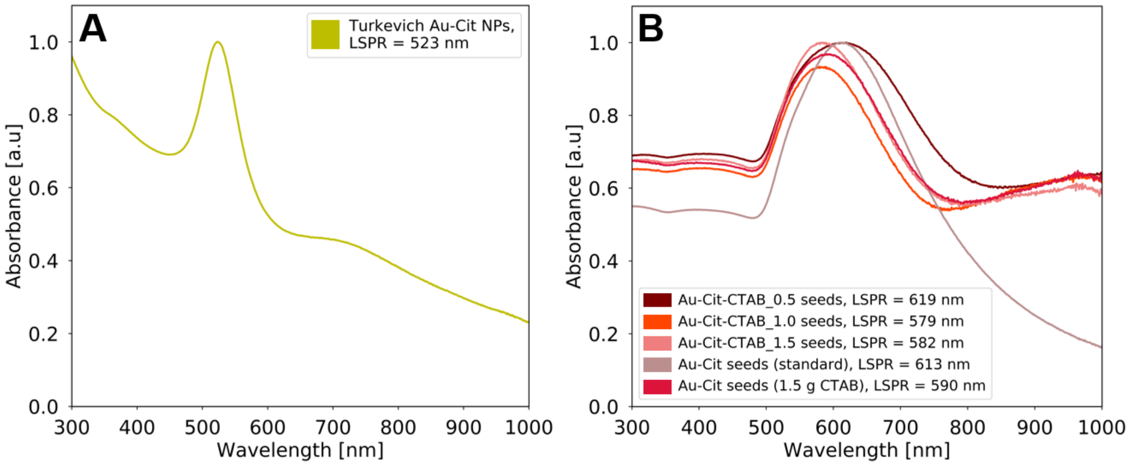

Figure 4.30: Normalized UV-vis absorbance spectra of the Turkevich gold nanoparticles (Au NPs) before (A) and after (B) seed-mediated Au growth.

When using the Turkevich Au-Cit NPs as seeds, the LSPR peaks are much broader than the LSPR peaks of the Jana seeded particles. This is likely due to a higher polydispersity in the particles synthesized from the Turkevich seeds. Each NP with a different size or shape will have a LSPR at a specific wavelength unique to that morphology. As the absorbance spectra of a NP population is a sum of the absorbance of its particles, a more polydispersed population would have a broader absorption peak[106]. Nonetheless, comparing the representative S(T)EM images of the population of particles synthesized using the Turkevich seed to the Jana seeded particles, the former are bigger and show more anisotropic features.

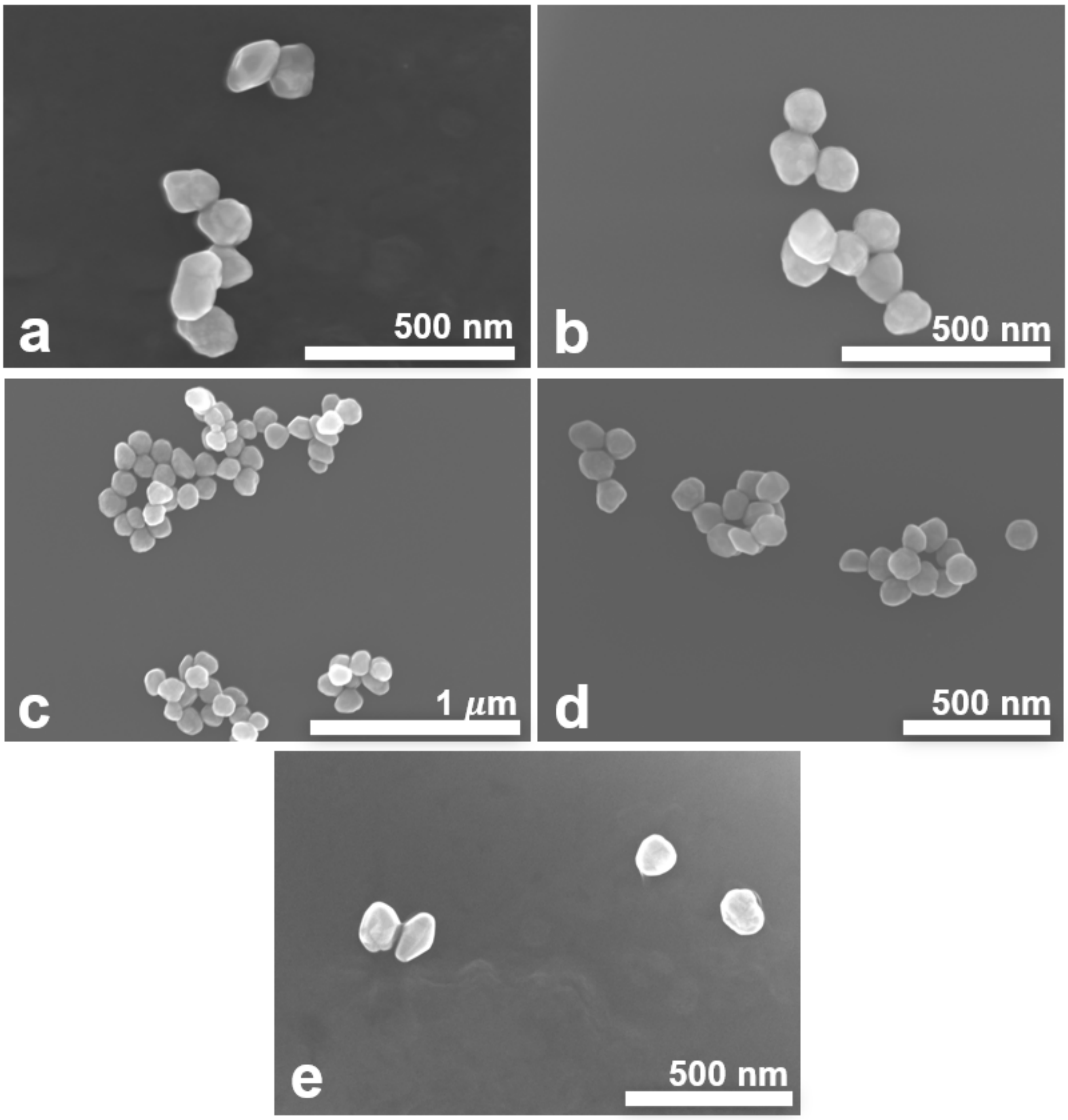

Figure 4.31: Representative scanning (transmission) electron microscope (S(T)EM) images of particles synthesized from seed-mediated Au growth on Turkevich gold nanoparticles (Au NPs). **a**: 480 μl Au-Cit-CTAB_0.5 seeds, **b**: 288 μl Au-Cit-CTAB_1.0 seeds, **c**: 224 μl Au-Cit-CTAB_1.5 μl seeds, **d**: 96 μl Au-Cit seeds with excess CTAB in the growth solution and **e**: 96 μl Au-Cit seeds, standard synthesis.

Having seen that the seeded growth works using both the Turkevich Au-Cit and Au-Cit-CTAB seeds, the Au seeds were replaced with iron-containing seeds to obtain magnetic-plasmonic particles. As a first try, the Fe@Au NPs were used as seeds as heterogeneous nucleation is more likely to occur when the seed and nucleating species are of the same material[20].

4.2.3 Fe@Au Seeds

Two sets of experiments were conducted while using the Fe@Au seeds synthesized from the IO-Cit NPs. In the first set, two experiments were performed, each in which 1.5 ml and 2.5 ml of the Fe@Au-Cit seed solution (see Table 4.6) was used respectively. In the second set, 224 μl of the two different Fe@Au-Cit-CTAB seeds (see Table 4.7) were used.

The UV-vis absorption spectra of the Fe@Au NPs before and after the seed-mediated growth is shown in Figure 4.32A and 4.32B respectively. After the Au growth, the particles from the Fe@Au-Cit seeded synthesis have an increased absorption peak that has been red-shifted by 28 and 50 nm respectively. However, the shape of the curves stayed more or less the same. This can indicate that Au has indeed grown on the seed, but that it only resulted in an isotropic increase of the Au-shell, and not necessarily in anisotropic particles. The sample in which 2.5 ml of the Fe@Au-Cit seeds were added have an LSPR that is red-shifted by 22 nm compared to the sample that had 1.5 ml seeds added. This indicate that the population synthesized using the larger seed-volume also resulted in larger particles. This is confirmed by the representative S(T)EM images taken of the two populations as shown in Figure 4.33. Using the ImageJ software, the sizes of the 1.5 ml Fe@Au-Cit seeded particles are $\sim$ 30 nm smaller than the particles synthesized using 2.5 ml seed solution. The S(T)EM images also show the presence of uncoated seeds, more so in the population using a smaller seed volume. As indicated by their UV-vis spectra, the particles are only slightly anisotropic, having oval morphologies.

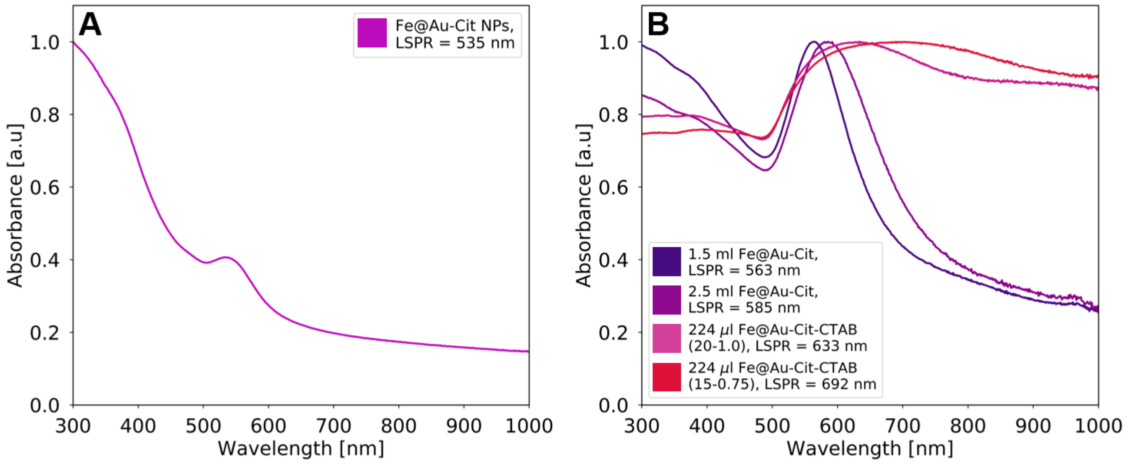

Figure 4.32: Normalized UV-vis absorbance spectra of the iron gold core shell nanoparticles (Fe@Au NPs) before (A) and after (B) seed-mediated Au growth.

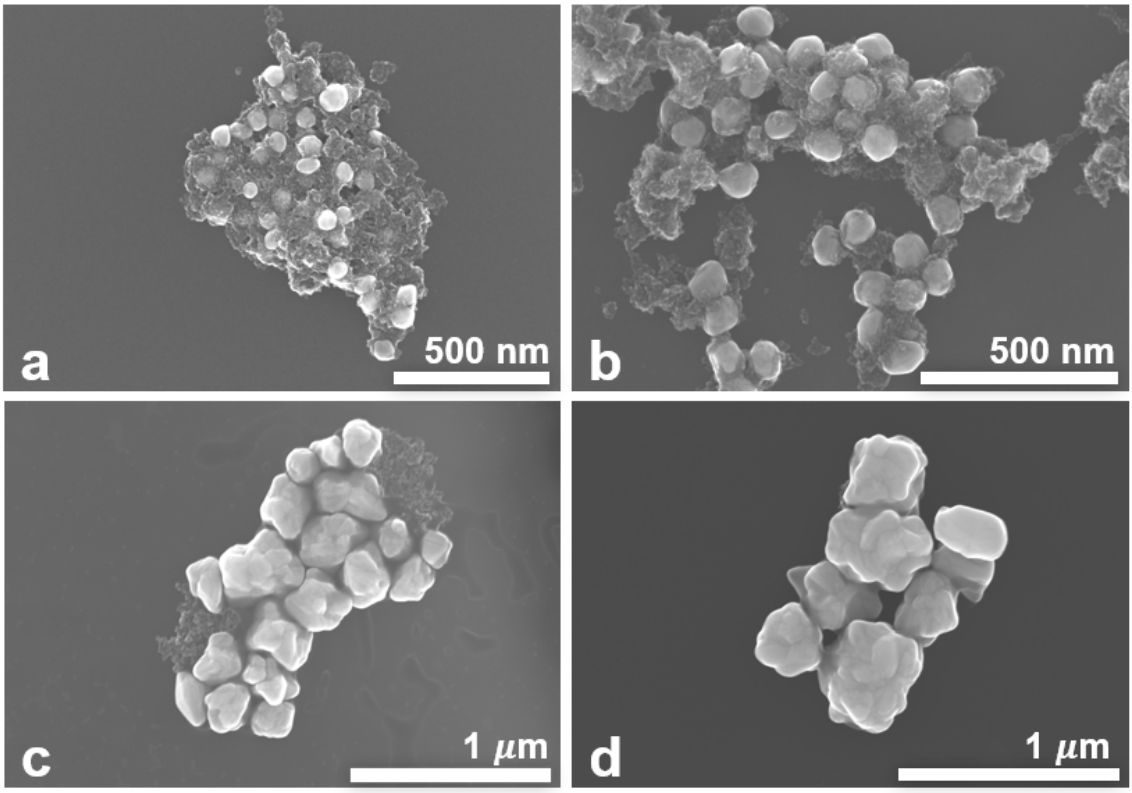

Figure 4.33: Representative scanning (transmission) electron microscope (S(T)EM) images of particles synthesized from the seed-mediated growth using iron gold core shell nanoparticle (Fe@Au NP) seeds. **a**: 1.5 ml and **b**: 2.5 ml of Fe@Au-Cit seeds, **c**: 224 μl Fe@Au-Cit-CTAB (20-1.0) seeds, and **d**: 224 μl Fe@Au-Cit-CTAB (15-0.75) seeds.

The absorption spectra of the particles synthesized using the Fe@Au-Cit-CTAB seeds on the other hand, have broadened after the Au growth, indicating the presence of new morphologies. From the representative S(T)EM images of the four populations (Figure 4.33), it is clear that the Fe@Au-Cit-CTAB seeded particles are larger, with sizes of $\sim$ 250 nm, and have more anisotropic features than the Fe@Au-Cit seeded particles. In the previous section it was shown that the particles synthesized using CTAB adsorption seeds have similar morphologies and absorption spectra as the particles synthesized from citrate capped seeds. Therefore, the difference in ZP of the two seeds is likely not the cause of the difference in the resulting NP populations. It is more likely due to the difference in the added seed volume in the two sets of experiments.

As a way of increasing the magnetic moment of the seeds, and the seed-mediated particles, the Fe@Au seeds were switched with IO NPs in the following experiments.

4.2.4 IO NP Seeds

Four seed-mediated NP synthesis were performed using IO NPs as seeds. In the first experiment, 182 μl of the IO-Cit NP seeds were used. The UV-vis absorption spectra of the IO-Cit NP seeded particles before and after the Au growth is shown in Figure 4.34A and 4.34B respectively. The spectra show no sign of plasmonic activity, indicating that no gold has nucleated and grown on the seeds. Looking at the S(T)EM image of this sample, shown in Figure 4.35a, there are actually some Au-containing anisotropic particles present. As the mass density of gold is higher than that of iron, gold appear brighter in the S(T)EM images[107]. However, the fraction of gold is likely too small as compared to the amount of uncoated iron in the sample to be detected by the UV-vis spectrometer.

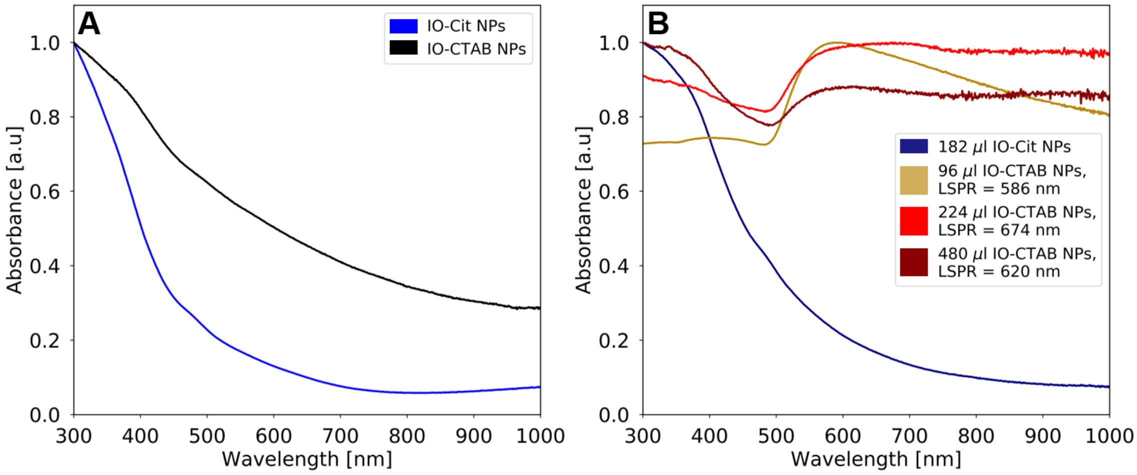

Figure 4.34: Normalized UV-vis absorption spectra of the two different aqueous iron oxide nanoparticles (IO NPs) before (A) and after (B) the seed-mediated growth.

Due to the lack of LSPR, the IO-Cit NPs were replaced with IO-CTAB seeds. Using the IO-CTAB NP as seeds, three synthesis were performed, using seed volumes of 96, 224 and 480 μl. The UV-vis absorption spectra of the IO-CTAB NPs before and after the seed-mediated growth is shown in Figure 4.34A and 4.34B respectively. The absorption spectra of the the IO-CTAB seeded particles all show plasmonic behavior. The representative S(T)EM images from these populations with seed volumes of 96, 224 and 480 μl are shown in Figure 4.35b, 4.35c and 4.35d respectively. In these images, no uncoated iron seeds are present. The population synthesized from 96 μl seed contain particles with a wide range of sizes, indicating a high polydispersity. When more seeds are added, the particles appear more monodispersed. Consequently, it is the two samples in which 224 and 480 μl IO-CTAB seeds are added that are the most suitable for biosensing applications. It is therefore the IO-CTAB seeds and the seed volumes of

224 and 480 μl that is used in the following and final set of experiments.

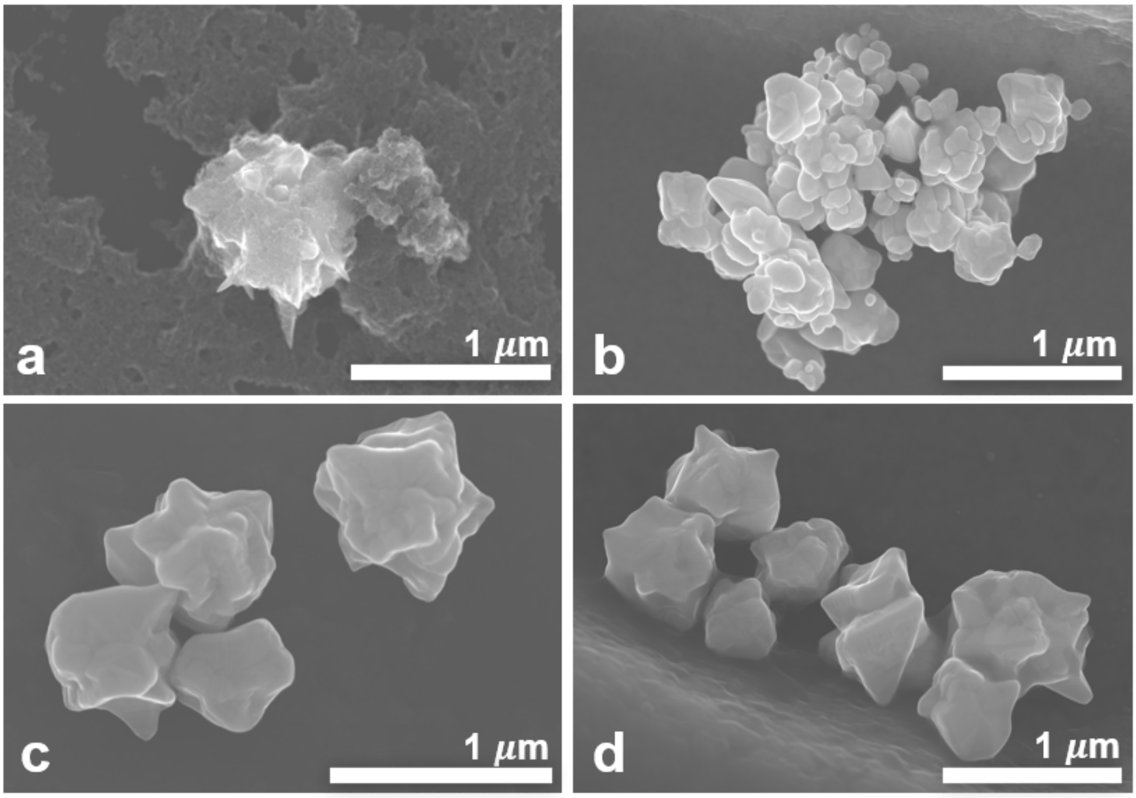

Figure 4.35: Representative scanning (transmission) electron microscope (S(T)EM) images of particles synthesized from seed-mediated Au growth using iron oxide nanoparticle (IO NP) seeds. **a**: 182 μl of IO-Cit NP seeds, **b**: 96 μl, **c**: 224 μl, and **d**: 480 μl of the IO-CTAB NP seeds.

4.2.5 Effect of pH and $AgNO_3$

As pH and $AgNO_3$ already have been shown to be reaction parameters that strongly influence the final morphology of nanoparticles[105], these parameters were varied in the IO-CTAB seeded Au growth of anisotropic nanostructures. The JMP software was used to optimize the experimental design. The 12 different experiments with different combinations of $AgNO_3$ and pH as proposed by the JMP software were divided into two sets (due to experimental convenience) as shown in Table 4.9. These two sets of experiments were conducted using both 224 μl and 480 μl of the seed solution, as these volumes of IO-CTAB seeds gave the most promising results in the previous section.

Table 4.9: The different combinations of $AgNO_3$ and pH used in the two sets of seed-mediated growth, as proposed by the JMP software.

Experiment Set 1						
$AgNO_3$ [μl]	2000	2000	1190	1190	375	1190
pH	1.5	10	1.5	10	3.4	3.4

Experiment Set 2						
$AgNO_3$ [μl]	2000	2000	375	375	375	2000
pH	10	1.5	3.4	10	1.5	3.4

224 μl IO-CTAB NP seeds

Following the procedure for seed-mediated growth as described in Section 3.5, anisotropic nanostructres were synthesized using 224 μl IO-CTAB NP seeds. 12 experiments were conducted using the combinations of values for the pH and $AgNO_3$ as reported in Table 4.9. The other reaction parameters involved were kept constant, using the standard values. While performing the cleaning procedure, it was found that some of the newly synthesized NPs had settled down during the overnight growth and were no longer dispersed in the reaction solution. The resulting NP populations were therefore divided into particles dispersed in the top product (TP) and particles left in the bottom product (BP) of the sample. The NPs of the BP were generally less concentrated and were not centrifuged contrary to the NPs of the TP. This was not considered necessary as most of the excess CTAB and other impurities of the growth solution was poured off when removing the TP.

The UV-vis absorption spectra of the particles found in the TP and the BP synthesized at pH = 1.5 are shown in Figure 4.36A and 4.36B respectively. Only the TP of the sample in which 375 μl $AgNO_3$ was added exhibit plasmonic behavior with an LSPR peak at $\sim$ 600 nm. At low pH the growth is expected to be slower as the reduction potential of the reducing agent is inhibited[105]. If the pH is too low, the reducing agent (ascorbic acid) will not be able to reduce the gold precursor (Au^{3+}), and there will be no build up of supersaturation. As a consequence, no growth will occur (see Section 2.3.6).

In order to get a first impression of the trends, only the samples showing promising LSPR properties based on their UV-vis spectra, were imaged in S(T)EM. Consequently, only the NPs synthesized at pH = 1.5 with 375 μl $AgNO_3$ were imaged and are shown in Figure 4.37. Whereas no defined particles could be seen in the TP, the particles found in the BP show a high degree of monodispersity. This could not be seen in their UV-vis absorption spectra, probably due to the low concentration of particles in this sample. The low concentration of the sample is also likely the reason why the absorption spectra of the BP show a higher level of noise than the TP spectra.

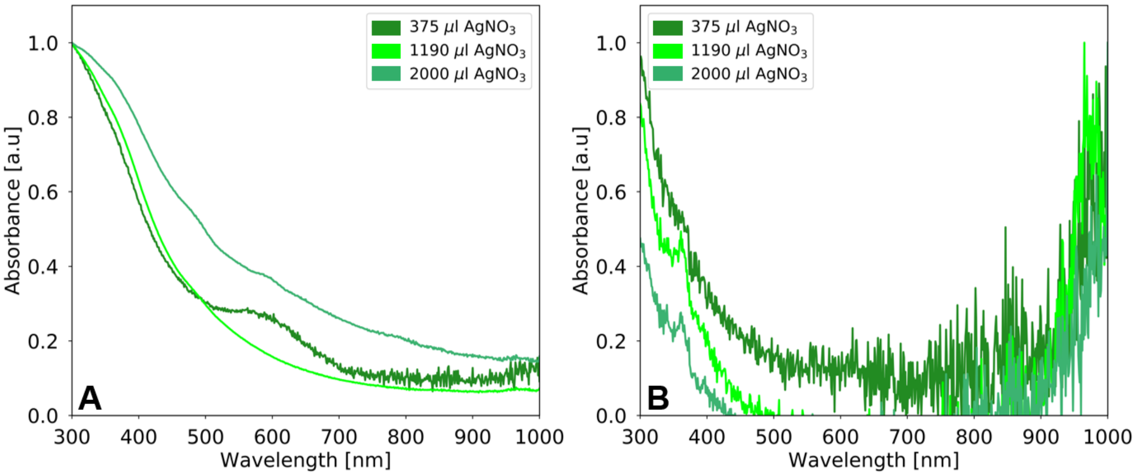

Figure 4.36: Normalized UV-vis absorption spectra of the NPs synthesized from seed-mediated Au growth at pH = 1.5, using 224 μl IO-CTAB NP seeds. Plot A and B show the spectra measured for the particles in the top and bottom product respectively.

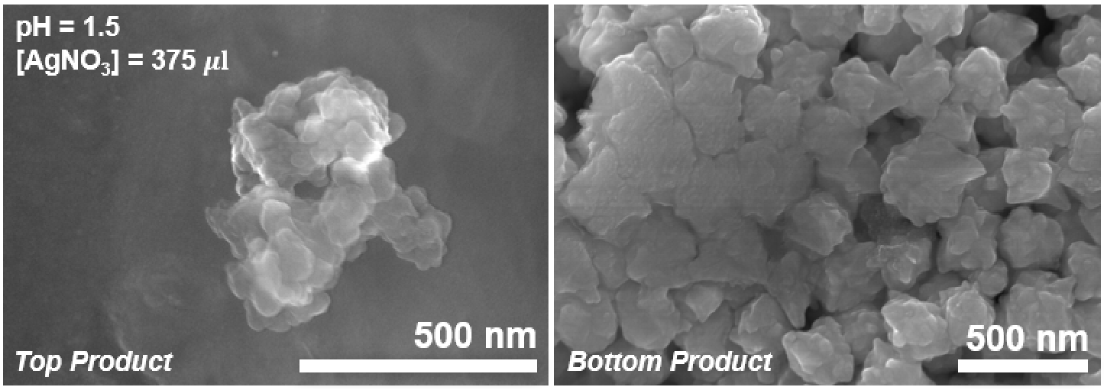

Figure 4.37: Scanning (transmission) electron microscope (S(T)EM) images of particles synthesized by seed-mediated growth at pH = 1.5, using 224 μl IO-CTAB NPs and 375 μl $AgNO_3$.

The UV-vis absorption spectra of the particles found in the TP and the BP, synthesized by seed-mediated growth at pH = 3.4, are shown in Figure 4.38A and 4.38B respectively. For these samples no acid or base was added to the growth solution. Contrary to the samples synthesized at pH = 1.5, all of the spectra now show plasmonic behavior. The corresponding S(T)EM images are shown in Figure 4.39. Comparing the NPs of the TP and the BP, they appear to have similar morphologies while the NPs in the BP have less sharp edges. All the samples, with exception of the TP of the sample in which 2000 μl $AgNO_3$ was added, showed low levels of monodispersity. In all the

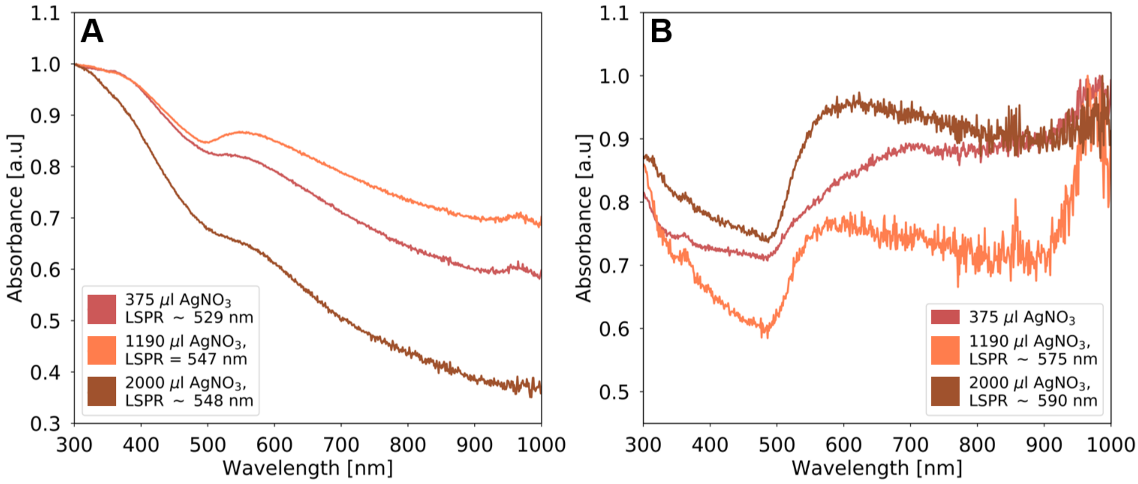

Figure 4.38: Normalized UV-vis absorption spectra of the particles synthesized from seed-mediated Au growth at pH = 3.4, using 224 μl IO-CTAB NP seeds. Plot A and B show the spectra measured for the particles in the top and bottom product respectively.

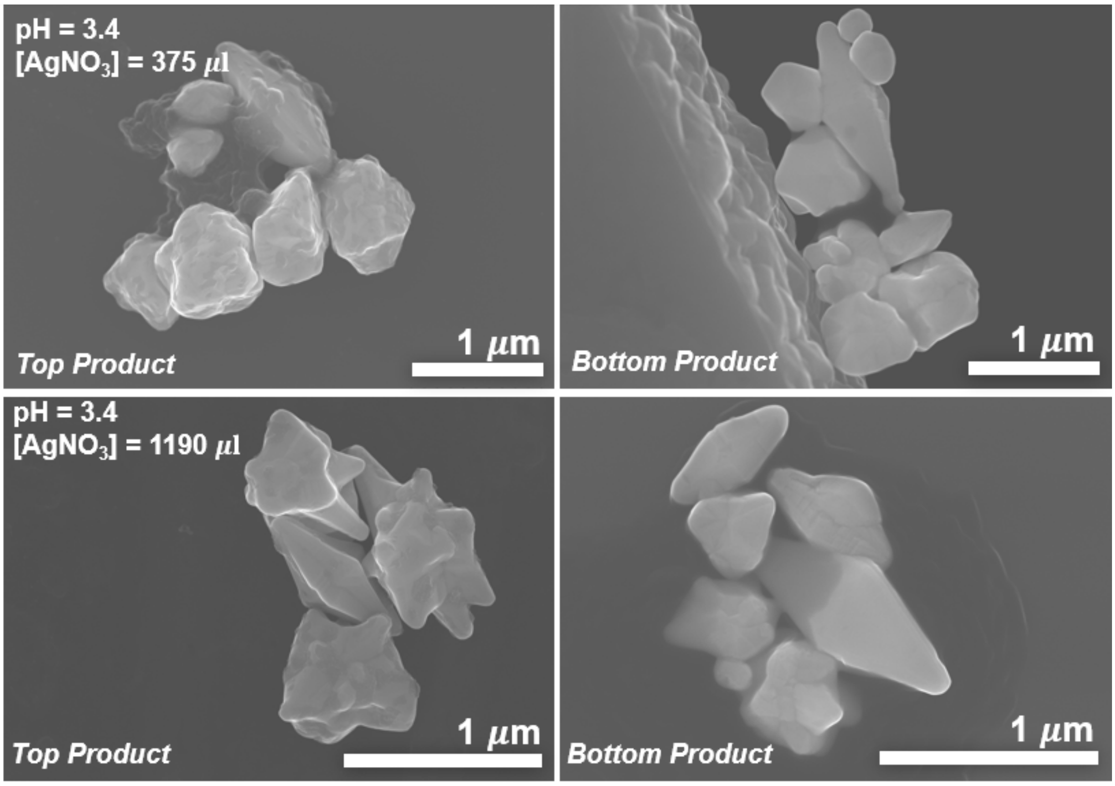

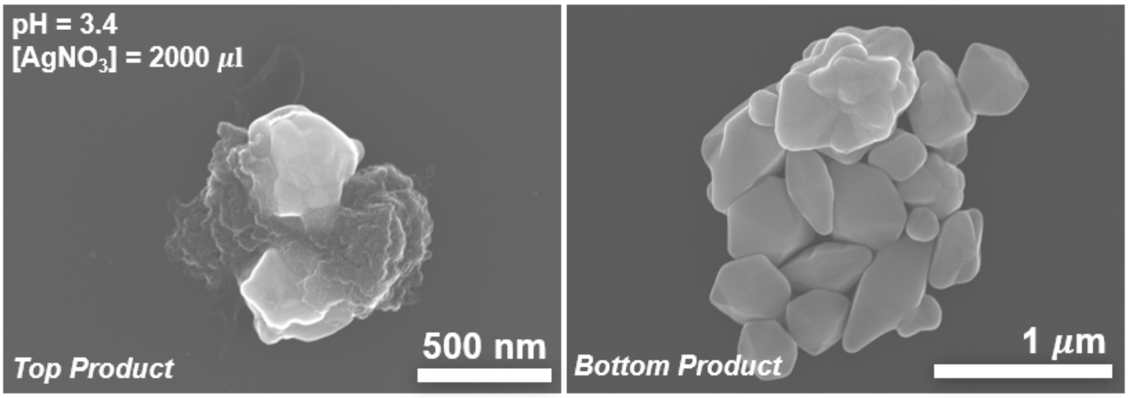

Figure 4.39: Representative scanning (transmission) electron microscope (S(T)EM) images of the particles synthesized from seed-mediated Au growth at pH = 3.4, using 224 μl IO-CTAB NPs.

images of the TP populations the presence of uncoated seed NPs can be seen. As the seed NPs are much smaller than the Au-coated particles, they are less likely to settle into the BP leading to a higher concentration of uncoated iron seeds in the TP. This is also indicated by the form of the absorption spectra of the samples. In fact, comparing the UV-vis absorption spectra of the top and bottom products, it is possible that if the presence of uncoated IO-CTAB seeds were removed the two spectra would look the same.

The UV-vis absorption spectra of the particles found in the TP and the BP, synthesized by seed-mediated growth at pH = 10, are shown in Figure 4.40A and 4.40B respectively. At this pH, there are signs of plasmonic behavior in both spectra, however less

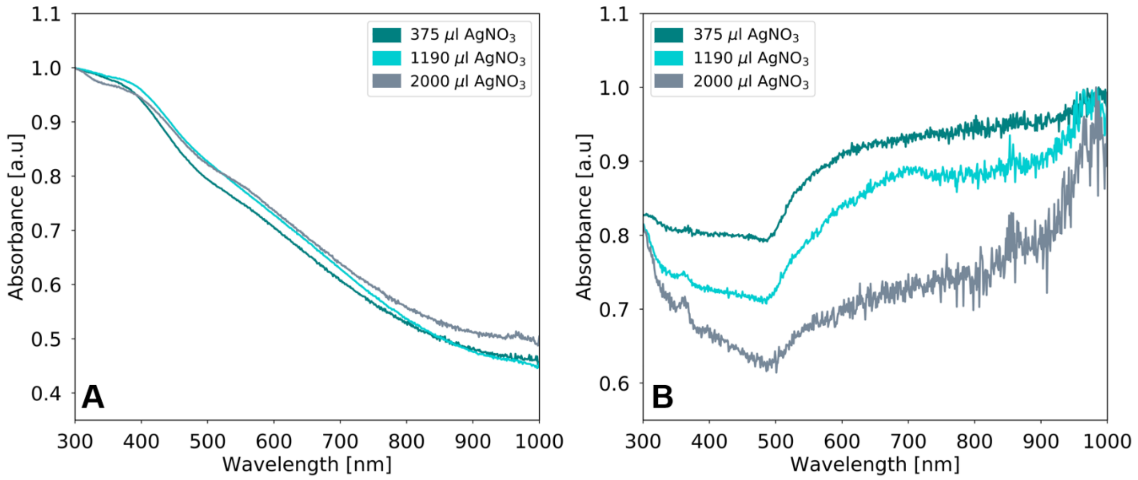

Figure 4.40: Normalized UV-vis absorption spectra of the particles synthesized from seed-mediated Au growth at pH = 10, using 224 μl IO-CTAB NP seeds. Plot A and B show the spectra measured for the particles in the top and bottom product respectively.

distinct than at pH 3.4. Also in these samples, the LSPR of the BP is more prominent. Again, the TP spectra are likely dominated by the iron content of the sample caused by a high fraction of uncoated seeds.

The representative S(T)EM images of the populations synthesized at pH 10, with 375 μl and 2000 μl $AgNO_3$, are given in Figure 4.41. In these images, no uncoated seeds are present. However, it should be noted that S(T)EM only gives an insight to a small fraction of the sample. The UV-vis spectrometer on the other hand, scans through a much larger, more homogeneous part of the sample. What can be seen in Figure 4.41 are Au coated anisotropic particles, more monodispersed than the particles synthesized at lower pH. The basic environment at this pH promotes a faster reduction of the gold precursor, generating a high supersaturation. This in turn increases the reactivity of the nucleation and growth leading to the star-shaped morphologies apparent in the S(T)EM images. Such morphologies are promising considering biosensing applications. The large surface area of these nanostructures enhances the interactions with a potential target molecule, and the fact that they are monodispersed ensures a consistent LSPR peak.

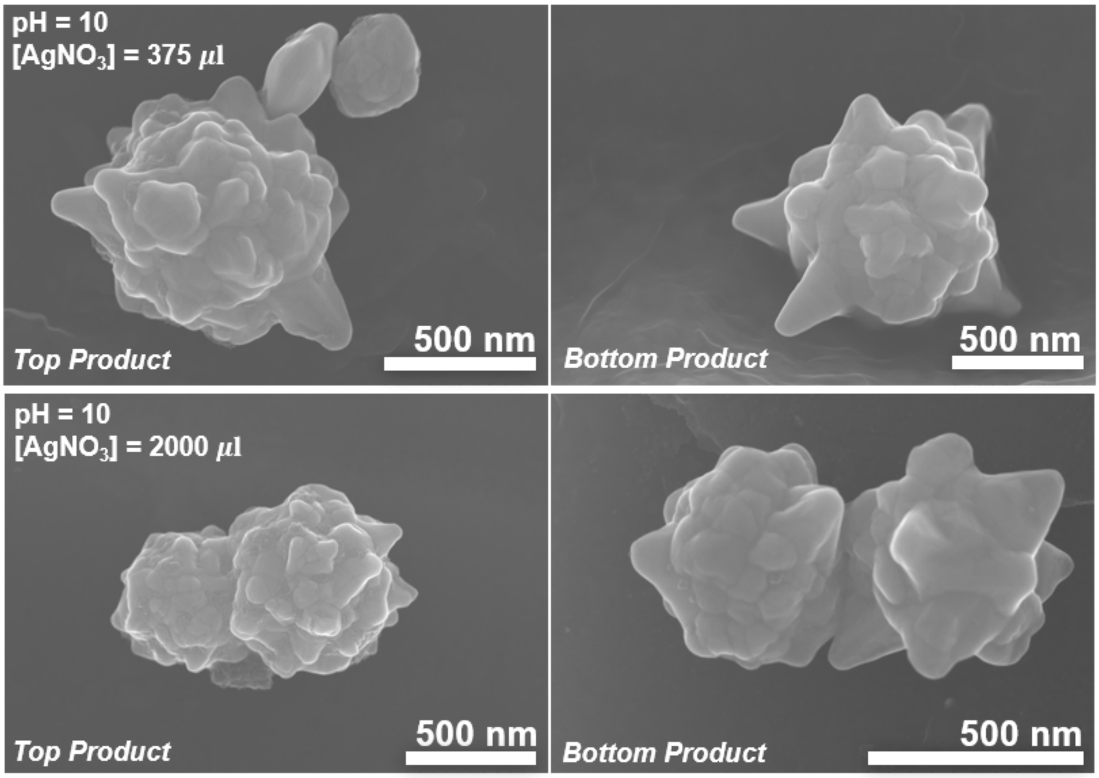

Figure 4.41: Representative scanning (transmission) electron microscope (S(T)EM) images of the particles synthesized by seed-mediated Au growth at pH = 10, using 224 μl IO-CTAB NPs, having added 375 and 2000 μl $AgNO_3$.

In order to increase the pH of the growth solution to 10, only ∼ 200 μl of the base had to be added. However, in the samples synthesized at pH = 1.5, ∼ 2.2 ml HCl had to be added to obtain the acidic pH. As a consequence, the total volume of the 12 different samples was not kept constant, which means that the concentrations of the chemicals involved in the synthesis also varied between the samples. This will in turn have affected the supersaturation of the systems, and could possibly have had an impact on the final morphology of the synthesized NPs. The effect of total reaction volume was not further studied as it was not included in the scope of this thesis.

480 μl IO-CTAB NP seeds

Next, the 12 experiments synthesizing anisotropic nanostructures while varying the pH and amount of $AgNO_3$ as presented in Table 4.9, were performed using 480 μl of the IO-CTAB NPs as seeds. Also these experiments resulted in a NP population separated into a TP and BP.

From previous discussion, it is not expected to see any distinct plasmonic behavior in the samples synthesized with a combination of such an acidic pH and high iron seed content. Indeed, in the UV-vis absorption spectra of these samples, given in Figure 4.42, no plasmonic behavior is observed. The curves resemble those of the seeds, indicating that no (or only very little) gold has grown on the iron seed.

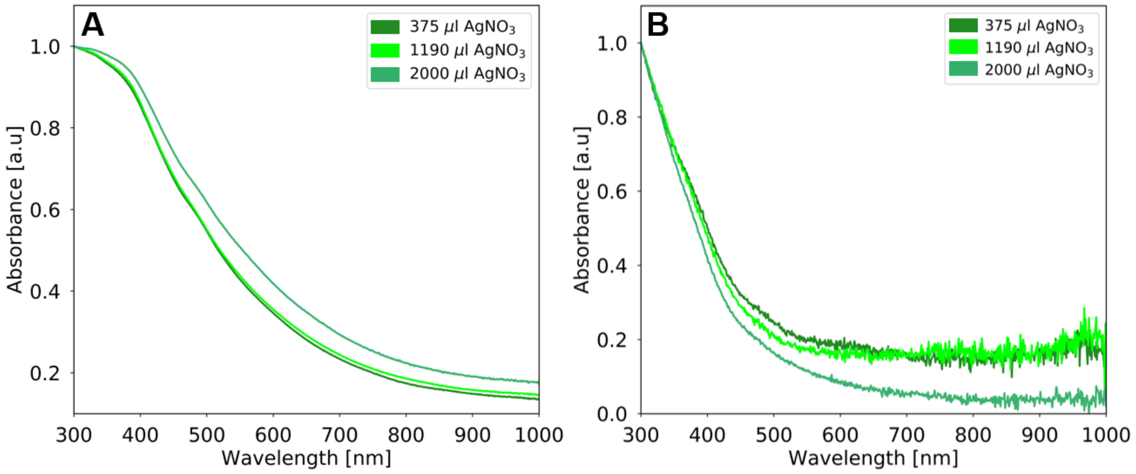

Figure 4.42: Normalized UV-vis absorption spectra of NPs synthesized from seed-mediated Au growth, using 480 μl IO-CTAB NP seeds, at pH = 1.5. Plot A and B show the spectra measured for the particles in the top and bottom product respectively.

The measured UV-vis absorption spectra of the NPs synthesized at pH 3.4 found in the TP and BP are given in Figure 4.43A and 4.43B respectively. When increasing the pH from 1.5 to 3.4, there are no big differences in the spectra of the TP. However, there are signs of plasmonic activity in the spectra of the BP, indicating the presence of gold.

The TP and the BP of the two extreme samples were imaged by S(T)EM. However, only in the TP could any kind of NP population be observed. The representative S(T)EM images of the TPs are given in Figure 4.44.

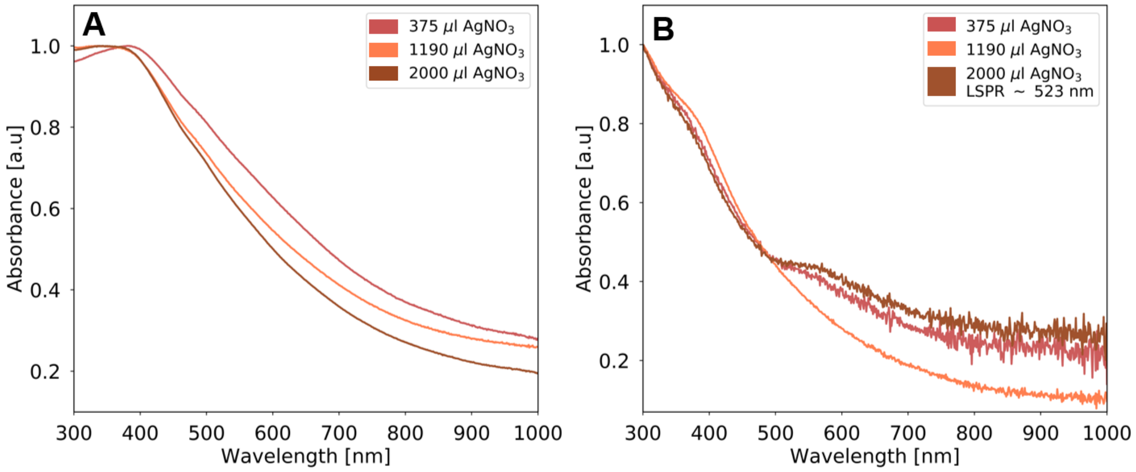

Figure 4.43: Normalized UV-vis absorption spectra of the NPs synthesized from seed-mediated Au growth at pH = 3.4, using 480 μl IO-CTAB NP seeds. Plot A and B show the spectra measured for the particles in the top and bottom product respectively.

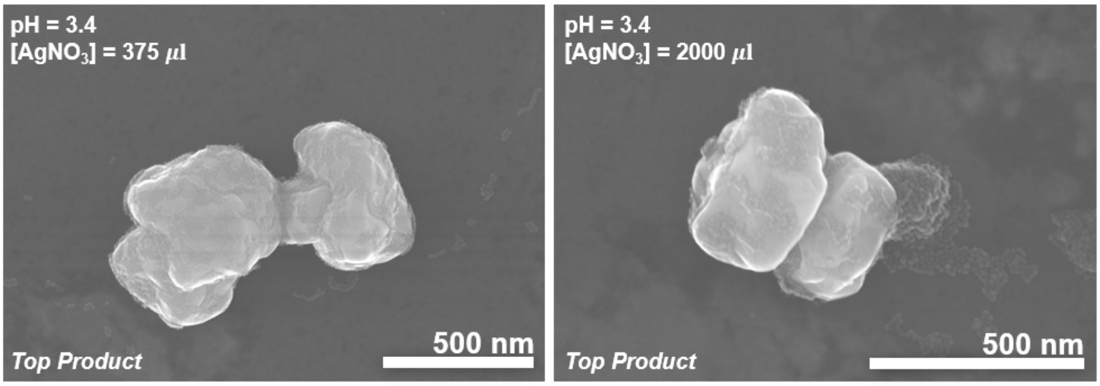

Figure 4.44: Representative scanning (transmission) electron microscope (S(T)EM) images of particles synthesized by seed-mediated Au growth at pH = 3.4, using 480 μl IO-CTAB NPs. Only the extreme samples, with regards to the added volume of $AgNO_3$, were imaged.

The UV-vis absorption spectra of the seed-mediated NPs synthesized at pH = 10 are given in Figure 4.45. When increasing the pH to 10, the LSPR of the TP are getting more visible, however it is the LSPR of the BP that are the most prominent. The S(T)EM images of the samples, shown in Figure 4.46, suggests that it is the sample in which 375 μl $AgNO_3$ is added that has the highest yield of anisotropic particles. This population also consist of larger particles that appear to have the highest surface area.

A larger surface area is considered beneficial for nano-biosensors as it increases the sites of interaction between the sensor and the target molecule.

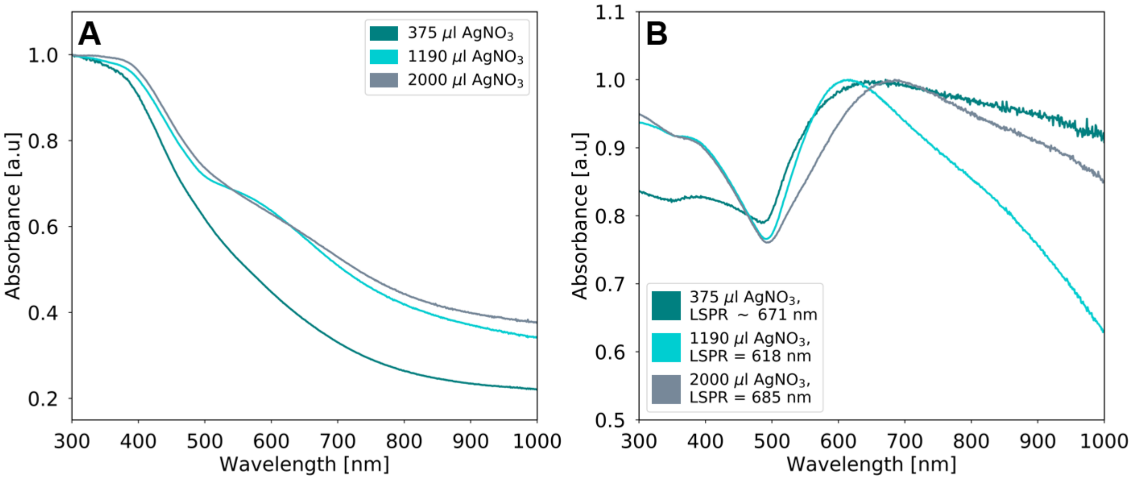

Figure 4.45: Normalized UV-vis absorption spectra of NPs synthesized through seed-mediated Au growth at pH = 10, using 480 μl IO-CTAB NP seeds. Plot A and B show the spectra measured for the particles in the top and bottom product respectively.

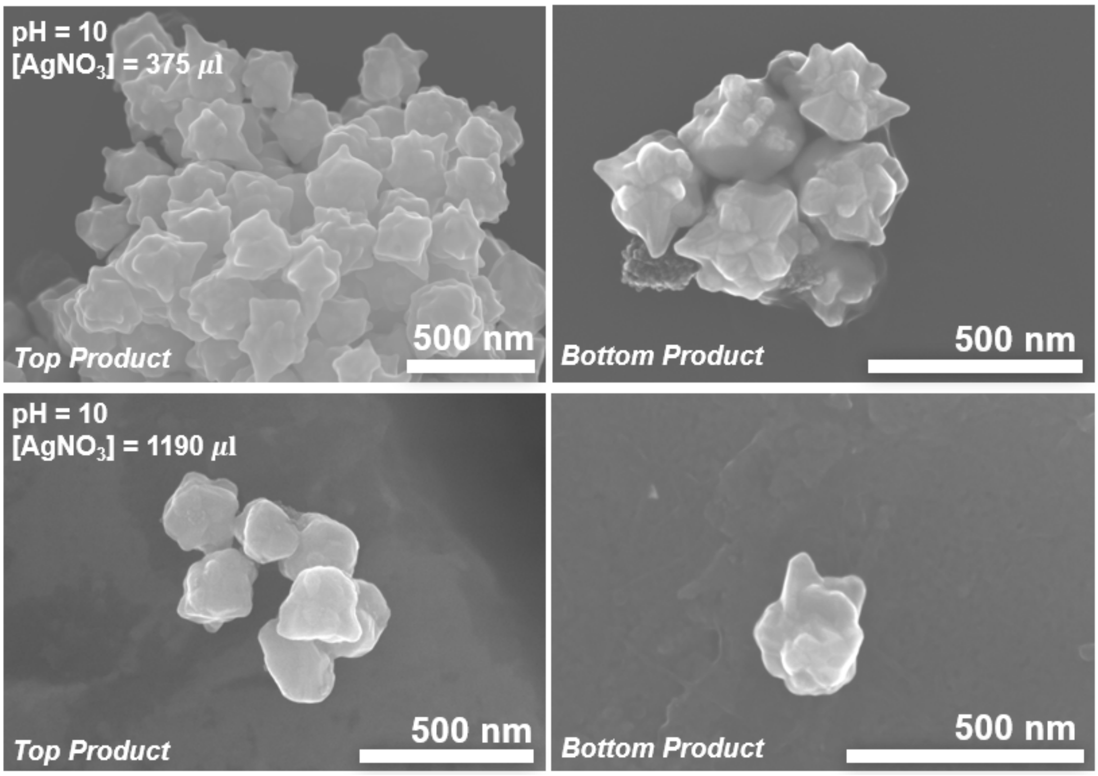

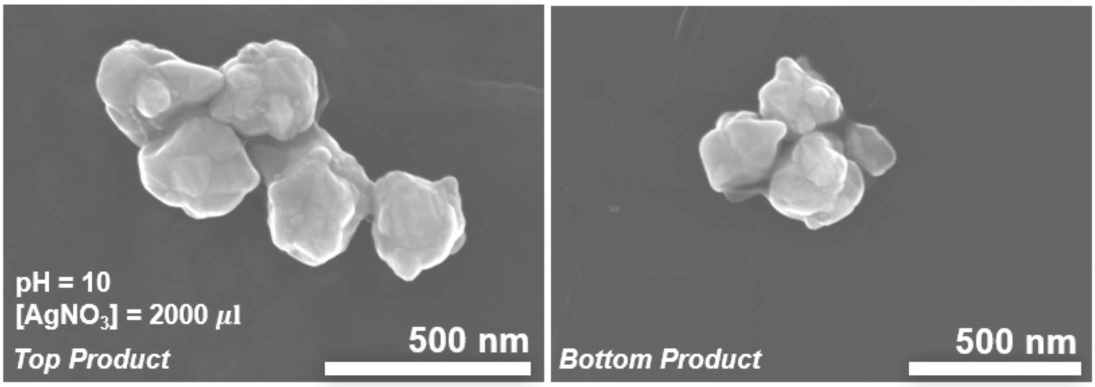

Figure 4.46: Representative scanning (transmission) electron microscope (S(T)EM) images of particles synthesized by seed-mediated Au growth at pH = 10, using 480 μl IO-CTAB NPs.

Magnetic Properties

Up until now, the focus has been on tailoring the plasmonic properties of the nanostructures as it is the LSPR that is exploited in the biosensing applications. However, the reason for using IO NPs as seeds was to obtain magnetic particles. In order to examine the magnetic properties of the anisotropic particles, magnetic separation was performed on the sample synthesized with 375 μl $AgNO_3$, at pH = 10. Figure 4.47 show the NP solution of the particles that separated out after 2, 10 and 30 min of being exposed to a magnetic field, and finally, also the particles that did not separate out, but were left in the supernatant.

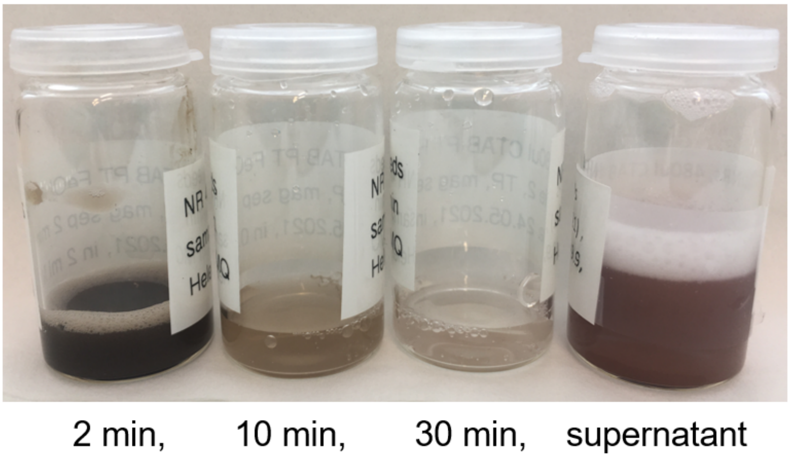

Figure 4.47: Samples of 480 μl IO-CTAB seeded particles that separated out solution after 2, 10, 30 min, and finally the particles that did not separate out after 30 min. For increasing separation times, the color of the solution changes from black (2 min separation time) to purple-pink (particles that did not separate after 30 min).

The color difference of the four solutions is an immediate indication that the plasmonic activity increases for the particles with longer separation times. With regards to the fraction of uncoated iron seeds, the opposite trend is expected. This is also what is seen in the UV-vis absorption spectra of the four solutions given in Figure 4.48. The NPs that separated out after 2 and 10 min of being exposed to the magnetic field show spectra similar to the absorption spectra of pure IO-CTAB NP. However, the 2 min spectra do show a minor peak at $\lambda \sim 800$ nm suggesting that the separated population contain plasmonic material. The particles that separated out after 30 min on the other hand, have an absorption spectra and LSPR peak similar to NPs of the supernatant and what is seen in the spectra of the BP in Figure 4.45B. This substantiates the earlier suspicion that the absorption spectra of the TP are largely dominated by the fraction of uncoated iron seeds.

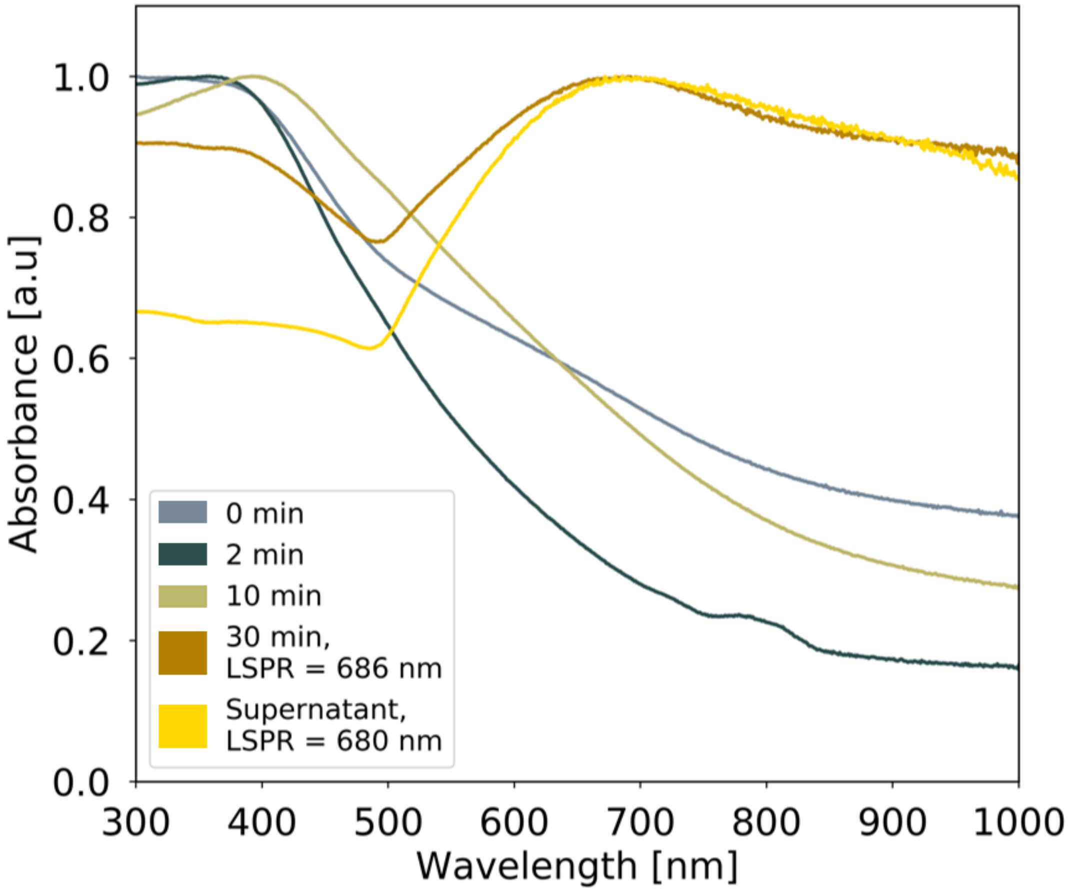

Figure 4.48: Normalized UV-vis absorption spectra of the particles synthesized from seed-mediated Au growth at pH = 10, using 480 μl IO-CTAB seeds and 375 μl $AgNO_3$, before and after magnetic separation. The gray, blue, beige and brown curves show the spectra of the particles that separated out from the solution after 0, 2, 10 and 30 min of being exposed to a magnetic field respectively. The spectra of the particles that did not separate out after 30 min of magnetic exposure is plotted in yellow.

The four fractions were examined in S(T)EM and their representative images shown in Figure 4.49. The representative images also show that the longer the solution is exposed to the magnetic field, the more anisotropic gold NPs and less uncoated iron seeds are observed. Yet, the presence of anisotropic NPs is observed in all the samples, suggesting that the magnetic moment may vary between each particle. This can be due to a variation in the number of IO-CTAB NPs that get Au coated at once. Looking at S(T)EM image of the IO-CTAB NPs (Figure 4.24), there are several different sized clusters present. As the heterogeneous nucleation of Au will happen on any given surface, it is possible that IO-CTAB NP get coated as clusters. This could result in magneto-plasmonic particles with varying amount of iron, again resulting varying magnetic moments. Another possibility is that the few magneto-plasmonic particles that separated out of solution after 2 min, only did so because they got trapped between surrounding seed NPs. Nonetheless, the anisotropic Au-coated IO-NPs that did separate out of solution due to the presence of the magnetic field, proved to exhibit both a characteristic LSPR and superparamagnetic behavior.

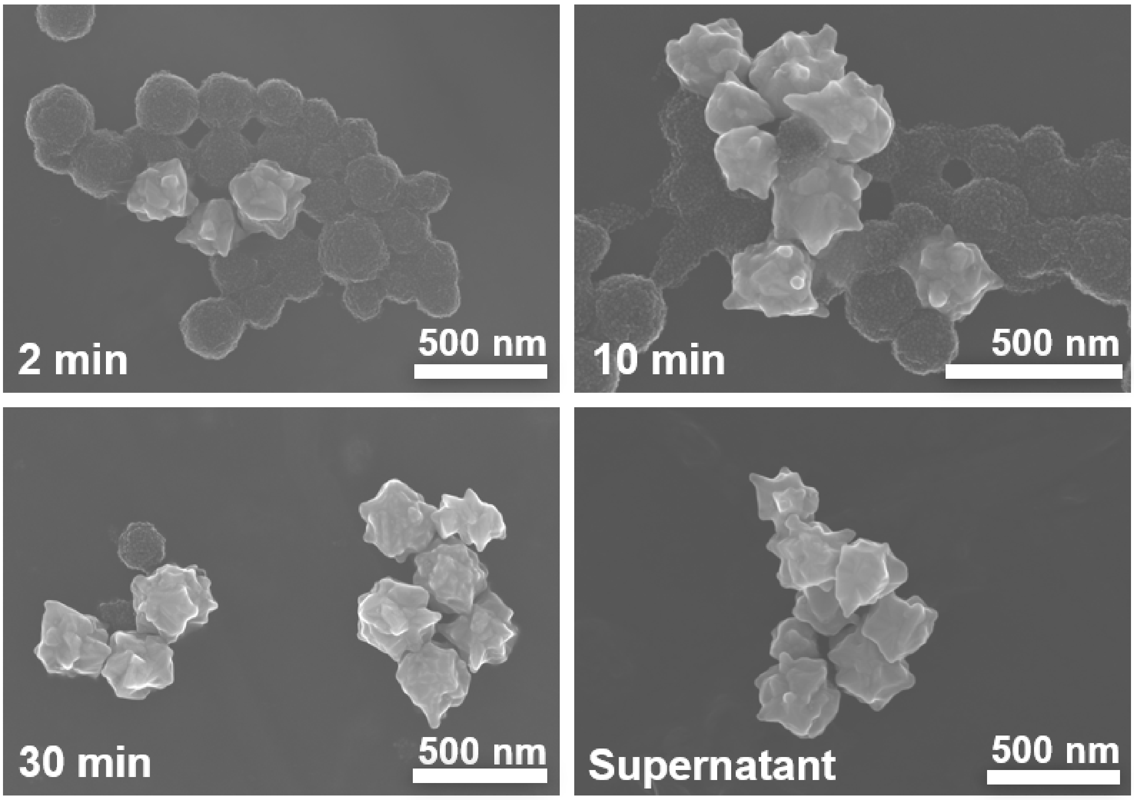

Figure 4.49: Representative scanning (transmission) electron microscope (S(T)EM) images of the particles that separated out after being exposed to a magnetic field for 2, 10 and 30 min, as well as the particles that were left in the supernatant. The particles were synthesized by seed-mediated Au growth at pH = 10, using 480 μl IO-CTAB NPs as seeds and 375 μl $AgNO_3$.

4.3 Summary and General Discussion

During the course of the experimental work, five different types of seed NPs were synthesized and characterized: Jana Au-Cit, Turkevich Au-Cit, IO-Cit NPs, IO-CTAB NPs, and Fe@-Au-Cit NPs. This collection of seeds consist of NPs of different material, different plasmonic and magnetic properties, different surface coating and charge, and different size distributions (see Table 4.8). All five seed populations were used as seeds in the seed-mediated Au growth towards anisotropic nanostructures. In these experiments, both the different types and amount of seed were tested.

The particles synthesized following the standard seed-mediated growth procedure, using the Jana Au-Cit seeds, were small ($\sim$ 30 nm) and showed little to no degree of anisotropy. It was found that the absence of $AgNO_3$ in the growth solution, lead to reduced shape control in the system, which in turn resulted in a NP population expressing several different anisotropic morphologies (see Figure 4.29A). As monodispersity is important in most biomedical applications, the Jana seeds were replaced with Turkevich seeds.

The Turkevich seeds were also citrate coated gold NPs, but the average size of the population was larger than for the Jana seeds. Consequently, the Turkevich Au-Cit seeded particles were larger than the Jana Au-Cit seeded particles. The former population also exhibited more anisotropic features. Furthermore, the Turkevich Au-Cit seeds were functionalized with a CTAB surface layer. It was found however, that the particles synthesized using the Turkevich Au-Cit seeds and the Turkevich Au-Cit-CTAB seeds showed similar physico-chemical properties, rendering the CTAB adsorption unnecessary.

Having seen that the seed-mediated protocol worked, the Au seeds were replaced with iron-containing seeds in order to obtain magneto-plasmonic NPs. Considering the fact that heterogeneous nucleation is more likely to occur when the seed and the nucleating species are of the same material, the Au coated iron particles were used as seeds in the first try. Using the Fe@Au-Cit NP as seeds, it was found that the volume of the seed solution could impact the seed-mediated growth. Using large seed volumes (1.5-2.5 ml) resulted in an isotropic increase of the gold shell, whereas smaller seed volumes (224 μl) promoted anisotropic growth. The particles synthesized from using 224 μl Fe@Au seed solution were also larger ($\sim$ 250 nm), implying a larger surface area. A larger surface area is considered beneficial for nano-biosensors as it increases the sites of interaction between the sensor and the target molecule.

Next, the Fe@Au NPs were replaced with IO NPs in order to increase the M_S of the particles. The different M_S values of the seeds are summarized in Table 4.8. The seed-mediated particles synthesized from using the IO-Cit population as seeds did not exhibit a LSPR. When using the IO-CTAB NP seeds, on the other hand, the resulting particle population did exhibit LSPR. In fact, it was the IO-CTAB NP seeds that gave the most promising anisotropic magneto-plasmonic nanostructures. This population had the most monodispersed particles, combined with a defined LSPR peak. Both the experiments using 224 μl, and the ones in which 480 μl of the IO-CTAB NPs seeds were added resulted in such anisotropic particles. Therefore, the remaining experiments were conducted using 224 μl and 480 μl of the IO-CTAB seeds.

In the final part of the experimental work, the added volume of $AgNO_3$ and the pH of the growth solution was varied. It was found that the particles synthesized at high pH had the plasmonic properties most suited for biosensing applications. Increasing the pH of the solution, increased the reduction potential of the reducing agent, which lead to a fast build up of the solution's supersaturation. This in turn, lead to a reaction controlled deposition of gold on the seed particles resulting in the observed star-shape morphology in Figure 4.46. For the synthesis taking place at this pH, it was the samples in which the lowest amount of $AgNO_3$ was added that resulted in the most promising nanostructures. $AgNO_3$ is a reaction parameter that has been shown to induce shape control in NP synthesis, restricting growth at preferential crystal facets. Thus, it is possible that the high volumes of $AgNO_3$ reduces the number of "spikes" on the particle's surface leading to particles with smaller surface areas.

The magnetic properties of one population of anisotropic nanostructures (synthesized using 480 μl IO-CTAB NP seeds, with 375 μl $AgNO_3$ and at a pH of 10) were examined. It was found that for increasing time in the presence of a magnetic field, more of the anisotropic particles separated out of solution. Comparing the UV-vis absorption spectra of the sample before and after magnetic separation (see Figure 4.48), it is clear that the original spectra is a superposition of the iron signal of the uncoated seed NPs and the plasmonic LSPR of the anisotropic Au coated NPs. Also confirmed by the S(T)EM images (see Figure 4.49), the particles that separated out after 2 and 10 min were largely uncoated iron seeds. The particles that separated out after 30 min, and the particles that did not separate out, were mainly Au coated particles. The Au coated particles that separated out of solution due to the presence of the magnetic field, proved to exhibit both a characteristic LSPR and superparamagnetic behavior. Furthermore, the population chosen for magnetic separation (synthesized at pH = 10, using 480 μl IO-CTAB NP seeds and 375 μl $AgNO_3$) was the population that showed the highest yield of monodispersed particles with large surface areas. Both of which are properties that contributes to making these anisotropic magneto-plasmonic nanoparticles suitable for biosensing applications.

4.4 Potential Applications and Future Work

The LSPR peak of the star-shaped NPs synthesized at pH = 10, is characteristic for the particles in this population. As indicated by the different UV-vis absorption spectra measured throughout this thesis, and elaborated on in Section 2.1.2, the LSPR properties of NPs are dependent on several factors. These factors include the composition, size and morphology of the NPs as well as their surrounding environment. Consequently, the LSPR peak of a given NP can act as a highly sensitive probe able to detect changes in the local refractive index at the nanoparticle surface. Such changes, which typically occur as a result of biomolecular interactions at the nanoparticle surface, can thus be monitored as it results in a distinct shift of the LSPR wavelength. This way, the NPs can be used to detect the presence of any given target-molecule that is able to bind to its surface. In order for the magneto-plasmonic NPs synthesized in this thesis to be used for this purpose, they would first have to be surface functionalized with a molecule that specifically binds to the target of choice. For the particles synthesized in this work, especially two target-molecule candidates were considered; Lipopolysaccharides (LPS) and the severe acute respiratory syndrome coronavirus 2 (SARS-CoV-2).

The superparamagnetic behavior of the anisotropic particles allows them to separate out of solution when exposed to a magnetic field. Combined with the plasmonic properties of the NPs, it would not only be possible to detect the presence of a molecule, but to separate it out of the liquid in which it is contained. In the case of LPS, which are common byproducts of biopharmaceuticals, the functionalized magneto-plasmonic nano-stars could be used as a purification system. After having detected the presence of the endotoxin, the particles (along with the bound target analyte) could also be removed from the biopharmaceutical product, making it safe to use. Another benefit of magnetic separation is the possibility of recycling the particles for multiple reuses.

In order to synthesize magneto-plasmonic nano-biosensors for industrial use, the synthesis procedure should yield particles with identical magnetic and optical properties in every synthesis. Although this thesis examines the role of various reaction parameters involved in the seed-mediated synthesis of magneto-plasmonic NPs, a more systematic study is necessary before a such a protocol can be developed. Experiments studying the impact of the different seed properties, including their size, monodispersity, surface charge and capping agent, should be conducted. Optimizing the FeOl and the IO-OA synthesis to increase the M_S of the IO-OA seeds should be looked into as it could impact the superparamagnetic properties of the final anisotropic particles. The Fe@Au-CTAB NPs (see Appendix Fe@Au-CTAB NPs) were never used as seeds in the seed-mediated Au growth procedure. Given the effect seen from using Fe@Au-Cit seeds, and the effect of using CTAB capped instead of citrate capped IO seeds, the Fe@Au-CTAB NPs could be good seed candidates. In order to investigate how the Au is deposited on the IO-CTAB seeds, energy dispersive X-Ray spectroscopy (EDS) could be performed on the magneto-plasmonic particles. This technique can for instance be used on S(T)EM images of the populations where elemental mapping would provide information about the amount of iron that gets encapsulated in each of the anisotropic particles. Furthermore, experiments investigating the interplay between changes in pH and the corresponding change of the total reaction volume could also be beneficial.

Chapter 5

Conclusion

The aim of this work has been to tailor magneto-plasmonic nanoparticles (NPs), i.e. optimize their physico-chemical properties, so that they are suitable for biosensing applications. In order to do so, a seed-mediated Au growth protocol was followed using a variety of seed NPs. In order to improve properties of the seed-mediated particles, several of the reaction parameters involved in the synthesis were varied.

Five different types of seed NPs have been synthesized and characterized: Jana Au-Cit, Turkevich Au-Cit, IO-Cit NPs, IO-CTAB NPs, and Fe@-Au-Cit NPs. This collection of seeds consist of NPs of different material, different plasmonic and magnetic properties, different surface coating and charge, and different size distributions. And, they were all used as seeds in the seed-mediated Au growth towards anisotropic nanostructures. In these experiments, both the different types and amount of seed were tested. The seed that gave the most promising anisotropic magneto-plasmonic nanostructures was the IO-CTAB NPs. This population had the most monodispersed particles, combined with a defined local surface plasmon resonance (LSPR) peak. Both the experiments using 224 μl, and the ones in which 480 μl of the IO-CTAB NPs seeds were added resulted in such anisotropic particles.

Next, also the added volume of $AgNO_3$ and the pH of the growth solution was varied. It was found that the particles synthesized at high pH had the plasmonic properties most suited for biosensing applications. Increasing the pH of the solution, also increases the reduction potential of the reducing agent, leading to a fast build up of the solution's supersaturation. This in turn, leads to a reaction controlled deposition of gold on the seed particles resulting in the observed star-shape morphology. For the synthesis taking place at this pH, it was the samples in which the lowest amount of $AgNO_3$ was added that resulted in the most promising nanostructures. $AgNO_3$ is a reaction parameter that has been shown to induce shape control in NP synthesis, restricting growth at preferential crystal facets. Thus, it is possible that the high volumes of $AgNO_3$ reduces the number of "spikes" on the particle's surface leading to particles with smaller surface areas.

Finally, the magnetic properties of one population of anisotropic nanostructures (synthesized at $pH = 10$, using 480 μl IO-CTAB NP seeds and with 375 μl $AgNO_3$) were examined. It was found that for increasing time in the presence of a magnetic field, more of the anisotropic particles separated out of solution. These particles proved to exhibit both a characteristic LSPR and superparamagnetic behavior. Furthermore, this population showed the highest yield of monodispersed particles with large surface areas. All of the aforementioned properties contributes to making these anisotropic magneto-plasmonic nanoparticles suitable for biosensing applications.

Further systematic studies should be performed in order to develop a synthesis procedure that will guarantee the yield of magneto-plasmonic NPs exhibiting identical magnetic and optical properties.

Bibliography

[1] Sepúlveda, B.; Angelomé, P. C.; Lechuga, L. M.; Liz-Marzán, L. M. LSPR-based nanobiosensors. *Nano Today* **2009**, *4*, 244–251.

[2] Cao, J.; Sun, T.; Grattan, K. T. Gold nanorod-based localized surface plasmon resonance biosensors: A review. *Sensors and Actuators, B: Chemical* **2014**, *195*, 332–351.

[3] Clark, L. C.; Lyons, C. ELECTRODE SYSTEMS FOR CONTINUOUS MONITORING IN CARDIOVASCULAR SURGERY. *Annals of the New York Academy of Sciences* **1962**, *102*, 29–45.

[4] Petryayeva, E.; Krull, U. J. Localized surface plasmon resonance: Nanostructures, bioassays and biosensing-A review. *Analytica Chimica Acta* **2011**, *706*, 8–24.

[5] Tran, N.; Webster, T. J. Magnetic nanoparticles: Biomedical applications and challenges. *Journal of Materials Chemistry* **2010**, *20*, 8760–8767.

[6] Bhalla, N.; Jolly, P.; Formisano, N.; Estrela, P. Introduction to biosensors. *Essays in Biochemistry* **2016**, 60–61.

[7] Ocvirk, G.; Buck, H.; DuVall, S. H. *(2016) Electrochemical Glucose Biosensors for Diabetes Care. In: Matysik FM. (eds) Trends in Bioelectroanalysis. Bioanalytical Reviews, vol 6. Springer, Cham*.

[8] World Health Organization (WHO), Date accessed: 11/02/2021. `https://www.who.int/news-room/fact-sheets/detail/diabetes`.

[9] Davis, F.; Higson, S. P. *Micro Fuel Cells*; Elsevier Inc., 2009; pp 243–292.

[10] Castillo-Henríquez, L.; Brenes-Acuña, M.; Castro-Rojas, A.; Cordero-Salmerón, R.; Lopretti-Correa, M.; Vega-Baudrit, J. R. Biosensors for the detection of bacterial and viral clinical pathogens. *Sensors (Switzerland)* **2020**, *20*, 1–26.

[11] Darbha, G. K.; Rai, U. S.; Singh, A. K.; Ray, P. C. Gold-nanorod-based sensing of sequence specific HIV-1 virus DNA by using hyper-rayleigh scattering spectroscopy. *Chemistry - A European Journal* **2008**, *14*, 3896–3903.

[12] Lu, X.; Dong, X.; Zhang, K.; Han, X.; Fang, X.; Zhang, Y. A gold nanorods-based fluorescent biosensor for the detection of hepatitis B virus DNA based on fluorescence resonance energy transfer. *The Analyst* **2013**, *138*.

[13] Mayall, R. M.; Smith, C. A.; Hyla, A. S.; Lee, D. S.; Crudden, C. M.; Birss, V. I. Ultrasensitive and Label-Free Detection of the Measles Virus Using an N-Heterocyclic Carbene-Based Electrochemical Biosensor. *ACS Sens.* **2020**, *5*, 2747–2752.

[14] World Health Organization (WHO), Date accessed: 11/02/2021. `https://covid19.who.int/`.

[15] Abadeer, N. S.; Fülöp, G.; Chen, S.; Käll, M.; Murphy, C. J. Interactions of Bacterial Lipopolysaccharides with Gold Nanorod Surfaces Investigated by Refractometric Sensing. *ACS Applied Materials and Interfaces* **2015**, *7*, 24915–24925.

[16] Mamat, U.; Wilke, K.; Bramhill, D.; Schromm, A. B.; Lindner, B.; Kohl, T. A.; Corchero, J. L.; Villaverde, A.; Schaffer, L.; Head, S. R.; Souvignier, C.; Meredith, T. C.; Woodard, R. W. Detoxifying Escherichia coli for endotoxin-free production of recombinant proteins. *Microbial Cell Factories* **2015**, *14*.

[17] Lei, C.; Qiao, Z.; Fu, Y.; Li, Y. Colorimetric detection of lipopolysaccharides based on a lipopolysaccharide-binding peptide and AuNPs. *Analytical Methods* **2016**, *8*, 8079–8083.

[18] Ahn, G.; Sekhon, S. S.; Jeon, Y. E.; Kim, M. S.; Won, K.; Kim, Y. H.; Ahn, J. Y. Detection of endotoxins using nanomaterials. *Toxicology and Environmental Health Sciences* **2017**, *9*, 259–268.

[19] Ramsvik, H. Synthesis and Functionalization of Heterodimeric Nanoparticles for Biomedical Applications. *Norwegian University of Science and Technology (NTNU)* **2020**,

[20] Kwizera, E. A.; Chaffin, E.; Wang, Y.; Huang, X. Synthesis and properties of magnetic-optical core-shell nanoparticles. *RSC Advances* **2017**, *7*, 17137–17153.

[21] Krylova, G.; Giovanetti, L. J.; Requejo, F. G.; Dimitrijevic, N. M.; Prakapenka, A.; Shevchenko, E. V. Study of nucleation and growth mechanism of the metallic nanodumbbells. *Journal of the American Chemical Society* **2012**, *134*, 4384–4392.

[22] Young, H. D.; Freedman, R. A. *university physics with modern physics*, 14th ed.; 2015; Vol. 2.

[23] Marghussian, V. *Nano-Glass Ceramics*; Elsevier, 2015; pp 181–223.

[24] Chokprasombat, K. Synthesis of Patterned Media by self-assembly of magnetic nanoparticles. *Walailak J Sci & Tech* **2011**, *8*, 87–96.

[25] Xiao-Li, L.; Yong, Y.; Jian-Peng, W.; Yi-Fan, Z.; Hai-Ming, F.; Jun, D. Chinese Physics B Novel magnetic vortex nanorings/nanodiscs: Synthesis and theranostic applications . *Chin. Phys. B* **2015**, *24*, 127510.

[26] Hu, H.; Yuan, Y.; Lim, S.; Wang, C. H. Phase structure dependence of magnetic behaviour in iron oxide nanorods. *Materials & Design* **2020**, *185*.

[27] Singh, G.; Kumar, P. A.; Lundgren, C.; Van Helvoort, A. T.; Mathieu, R.; Wahlström, E.; Glomm, W. R. Tunability in crystallinity and magnetic properties of core-shell Fe nanoparticles. *Particle and Particle Systems Characterization* **2014**, *31*, 1054–1059.

[28] Willets, K. A.; Van Duyne, R. P. Localized Surface Plasmon Resonance Spectroscopy and Sensing. *Annu. Rev. Phys. Chem.* **2007**, *58*, 267–297.

[29] Hadilou, N.; Souri, S.; Navid, H. A.; Bonabi, R. S.; Anvari, A.; Palpant, B. An optimal architecture of magneto-plasmonic core–shell nanoparticles for potential photothermal applications. *Phys. Chem. Chem. Phys* **2020**, *22*, 14318.

[30] Kim, M.; Lee, J. H.; Nam, J. M. Plasmonic Photothermal Nanoparticles for Biomedical Applications. *Advanced Science* **2019**, *6*.

[31] Riley, R. S.; Day, E. S. Gold nanoparticle-mediated photothermal therapy: applications and opportunities for multimodal cancer treatment. *WIREs Nanomed Nanobiotechnol* **2017**, *9*.

[32] Bhatia, P.; Verma, S. S.; Sinha, M. M. Optical Properties Simulation of Magneto-Plasmonic Alloys Nanostructures. *Plasmonics* **2019**, *14*, 611–622.

[33] Ee Fong, K.; Lanry Yung, L.-Y. Localized surface plasmon resonance: a unique property of plasmonic nanoparticles for nucleic acid detection. *Nanoscale* **2013**, *5*.

[34] Liz-Marzán, L. M. Tailoring Surface Plasmons through the Morphology and Assembly of Metal Nanoparticles. *Langmuir* **2006**, *22*, 32–41.

[35] Zhou, Z.; Zhu, X.; Wu, D.; Chen, Q.; Huang, D.; Sun, C.; Xin, J.; Ni, K.; Gao, J. Anisotropic Shaped Iron Oxide Nanostructures: Controlled Synthesis and Proton Relaxation Shortening Effects. *Chem. Mater* **2015**, *19*, 19.

[36] Sun, Y. Interfaced heterogeneous nanodimers. *National Science Review* **2015**, *2*, 329–348.

[37] Gutierrez, R. M. P.; Mendez, J. V. M.; Vazquez, I. A. *Nanostructures for Oral Medicine*; Elsevier Inc., 2017; pp 27–59.

[38] Sajanlal, P. R.; Sreeprasad, T. S.; Samal, A. K.; Pradeep, T. Anisotropic nanomaterials: structure, growth, assembly, and functions. *Nano Reviews* **2011**, *2*.

[39] Wang, C.; Xu, C.; Zeng, H.; Sun, S. Recent Progress in Syntheses and Applications of Dumbbell-like Nanoparticles **. *Adv Mater* **2009**, *21*, 3045–3052.

[40] Ajinkya, N.; Yu, X.; Kaithal, P.; Luo, H.; Somani, P.; Ramakrishna, S. materials Magnetic Iron Oxide Nanoparticle (IONP) Synthesis to Applications: Present and Future. *Materials* **2020**, *13*, 4644.

[41] Cotin, G.; Kiefer, C.; Perton, F.; Ihiawakrim, D.; Blanco-Andujar, C.; Moldovan, S.; Lefevre, C.; Ersen, O.; Pichon, B.; Mertz, D.; Bégin-Colin, S. Unravelling the Thermal Decomposition Parameters for The Synthesis of Anisotropic Iron Oxide Nanoparticles. *Nanomaterials* **2018**, *8*.

[42] Drmota, A.; Drofenik, M.; Koselj, J.; nidari, A. *Microemulsions - An Introduction to Properties and Applications*; InTech, 2012.

[43] Cabrera, L.; Gutierrez, S.; Menendez, N.; Morales, M.; Herrasti, P. Magnetite nanoparticles: Electrochemical synthesis and characterization. *Electrochimica Acta* **2008**, *53*.

[44] Velusamy, P.; Chia-Hung, S.; Shritama, A.; Kumar, G. V.; Jeyanthi, V.; Pandian, K. Synthesis of oleic acid coated iron oxide nanoparticles and its role in anti-biofilm activity against clinical isolates of bacterial pathogens. *Journal of the Taiwan Institute of Chemical Engineers* **2016**, *59*.

[45] Kayani, Z. N.; Arshad, S.; Riaz, S.; Naseem, S. Synthesis of Iron Oxide Nanoparticles by Sol–Gel Technique and Their Characterization. *IEEE Transactions on Magnetics* **2014**, *50*.

[46] Hassanjani-Roshan, A.; Vaezi, M. R.; Shokuhfar, A.; Rajabali, Z. Synthesis of iron oxide nanoparticles via sonochemical method and their characterization. *Particuology* **2011**, *9*.

[47] Liu, S.; Ma, C.; Ma, M. G.; Xu, F. *Composite Nanoadsorbents*; Elsevier, 2018; pp 295–316.

[48] Wu, S.; Sun, A.; Zhai, F.; Wang, J.; Xu, W.; Zhang, Q.; Volinsky, A. A. Fe3O4 magnetic nanoparticles synthesis from tailings by ultrasonic chemical co-precipitation. *Materials Letters* **2011**, *65*, 1882–1884.

[49] Li, L.; Jiang, W.; Luo, K.; Song, H.; Lan, F.; Wu, Y.; Gu, Z. Superparamagnetic Iron Oxide Nanoparticles as MRI contrast agents for Non-invasive Stem Cell Labeling and Tracking. *Theranostics* **2013**, *3*, 595–615.

[50] Rahmawati, R.; Taufiq, A.; Sunaryono, S.; Fuad, A.; Yuliarto, B.; Suyatman, S.; Kurniadi, D. Synthesis of Magnetite (Fe3O4) Nanoparticles from Iron sands by Co-precipitation-Ultrasonic Irradiation Methods. *JMES* **2018**, *9*, 155–160.

[51] Hariani, P. L.; Faizal, M.; Ridwan, R.; Marsi, M.; Setiabudidaya, D. Synthesis and Properties of Fe3O4 Nanoparticles by Co-precipitation Method to Removal Procion Dye. *International Journal of Environmental Science and Development* **2013**,

[52] Frey, N. A.; Peng, S.; Cheng, K.; Sun, S. Magnetic nanoparticles: synthesis, functionalization, and applications in bioimaging and magnetic energy storage. *Chem. Soc. Rev.* **2009**, *38*, 2532–2542.

[53] Campos, E. A.; Villela, D.; Stockler Pinto, B.; Sampaio De Oliveira, J. I.; Da Costa Mattos, E.; De Cássia, R.; Dutra, L. Synthesis, Characterization and Applications of Iron Oxide Nanoparticles-a Short Review. *J. Aerosp. Technol. Manag., São José dos Campos 7*, 267–276.

[54] Palma, S. I.; Marciello, M.; Carvalho, A.; Veintemillas-Verdaguer, S.; Morales, M. d. P.; Roque, A. C. Effects of phase transfer ligands on monodisperse iron oxide magnetic nanoparticles. *Journal of Colloid and Interface Science* **2015**, *437*, 147–155.

[55] Zou, C.; Yang, B.; Bin, D.; Wang, J.; Li, S.; Yang, P.; Wang, C.; Shiraishi, Y.; Du, Y. Electrochemical synthesis of gold nanoparticles decorated flower-like graphene for high sensitivity detection of nitrite. *Journal of Colloid and Interface Science* **2017**, *488*, 135–141.

[56] Okitsu, K.; Ashokkumar, M.; Grieser, F. Sonochemical Synthesis of Gold Nanoparticles: Effects of Ultrasound Frequency. *J. Phys. Chem. B* **2005**, *109*.

[57] Krzysztof Jeszka, J.; Chaudret, B.; Wostek-wojciechowska, D.; Jeszka, J. K.; Uznanski, P.; Amiens, C.; Lecante, P. *Synthesis of gold nanoparticles in solid state by thermal decomposition of an organometallic precursor*; 2004; Vol. 22.

[58] Dong, S.-A.; Zhou, S.-P. Photochemical synthesis of colloidal gold nanoparticles. *Materials Science and Engineering: B* **2007**, *140*.

[59] Daruich De Souza, C.; Ribeiro Nogueira, B.; Rostelato, M. E. C. Review of the methodologies used in the synthesis gold nanoparticles by chemical reduction. *Journal of Alloys and Compounds* **2019**, *798*, 714–740.

[60] Herizchi, R.; Abbasi, E.; Milani, M.; Akbarzadeh, A. Current methods for synthesis of gold nanoparticles Current methods for synthesis of gold nanoparticles. *Artificial Cells, Nanomedicine, and Biotechnology* **2014**,

[61] Liu, M.; Guyot-Sionnest, P. Mechanism of Silver(I)-Assisted Growth of Gold Nanorods and Bipyramids. *J. Phys. Chem. B* **1997**, *6661*, 101.

[62] Grzelczak, M.; Pérez-Juste, J.; Mulvaney, P.; Liz-Marzán, L. M. Shape control in gold nanoparticle synthesis. *Chemical Society Reviews* **2008**, *37*, 1783–1791.

[63] Tancredi, P.; da Costa, L. S.; Calderon, S.; Moscoso-Londoño, O.; Socolovsky, L. M.; Ferreira, P. J.; Muraca, D.; Zanchet, D.; Knobel, M. Exploring the synthesis conditions to control the morphology of gold-iron oxide heterostructures. *Nano Research* **2019**, *12*, 1781–1788.

[64] Okolieocha, C.; Raps, D.; Subramaniam, K.; Altstädt, V. Microcellular to nanocellular polymer foams: Progress (2004–2015) and future directions – A review. *European Polymer Journal* **2015**, *73*.

[65] Thanh, N. T.; Maclean, N.; Mahiddine, S. Mechanisms of nucleation and growth of nanoparticles in solution. *Chemical Reviews* **2014**, *114*, 7610–7630.

[66] McGinty, J.; Yazdanpanah, N.; Price, C.; ter Horst, J. H.; Sefcik, J. *The Handbook of Continuous Crystallization*; Royal Society of Chemistry: Cambridge, 2020.

[67] Karthika, S.; Radhakrishnan, T. K.; Kalaichelvi, P. A Review of Classical and Nonclassical Nucleation Theories. *Cryst. Growth* **2016**, *16*, 6663–6681.

[68] Shea, T. Bubble nucleation in magmas: A dominantly heterogeneous process? *Journal of Volcanology and Geothermal Research* **2017**, *343*, 155–170.

[69] Lamer, V. K.; Dinegar, R. H. Theory, Production and Mechanism of Formation of Monodispersed Hydrosols. *Ind. Eng. Chem.* **1942**, *34*.

[70] González-Rubio, G.; Kumar, V.; Llombart, P.; Díaz-Núñez, P.; Bladt, E.; Altantzis, T.; Bals, S.; Peña-Rodríguez, O.; Noya, E. G.; Macdowell, L. G.; Guerrero-Martínez, A.; Liz-Marzán, L. M. Disconnecting Symmetry Breaking from Seeded Growth for the Reproducible Synthesis of High Quality Gold Nanorods. *ACS Nano* **2019**, *13*, 4424–4435.

[71] Lohse, S. E.; Murphy, C. J. The Quest for Shape Control: A History of Gold Nanorod Synthesis. *Chem. Mater.* **2013**, *25*, 1250–1261.

[72] Khoshnevisan, K.; Barkhi, M.; Zare, D.; Davoodi, D.; Tabatabaei, M. Preparation and Characterization of CTAB-Coated Fe3O4 Nanoparticles. *Synthesis and Reactivity in Inorganic, Metal-Organic, and Nano-Metal Chemistry* **2012**, *42*, 644–648.

[73] Bandyopadhyay, S.; Kee Andersen, M.; Awais Ashfaq Alvi, M.; Sharma, A.; McDonagh, B. H.; Robert Glomm, W. Incorporation of Fe@Au nanoparticles into multiresponsive pNIPAM-AAc colloidal gels modulates drug uptake and release. *Colloid and Polymer Science* **2016**, *294*, 1929–1942.

[74] Noqta, O. A.; Aziz, A. A.; Usman, I. A.; Bououdina, M. Recent Advances in Iron Oxide Nanoparticles (IONPs): Synthesis and Surface Modification for Biomedical Applications. *J Supercond Nov Magn* **2019**, *32*, 779–795.

[75] Kim, J. et al. Imaging Agents Multifunctional Uniform Nanoparticles Composed of a Magnetite Nanocrystal Core and a Mesoporous Silica Shell for Magnetic Resonance and Fluorescence Imaging and for Drug Delivery**. *Angew. Chem. Int. Ed* **2008**, *47*, 8438–8441.

[76] Chambers, J. P.; Arulanandam, B. P.; Matta, L. L.; Weis, A.; Valdes, J. J. Biological recognition elements. *Curr Issues Mol. Biol.* **2008**, *10*, 1–12.

[77] Unser, S.; Bruzas, I.; He, J.; Sagle, L. Localized Surface Plasmon Resonance Biosensing: Current Challenges and Approaches. *Sensors* **2015**, *15*.

[78] McFarland, A. D.; Van Duyne, R. P. Single Silver Nanoparticles as Real-Time Optical Sensors with Zeptomole Sensitivity. *Nano Letters* **2003**, *3*.

[79] Sharifi, M.; Hasan, A.; Haghighat, S.; Taghizadeh, A.; Attar, F.; Haj Bloukh, S.; Edis, Z.; Xue, M.; Khan, S.; Falahati, M. Rapid diagnostics of coronavirus disease 2019 in early stages using nanobiosensors: Challenges and opportunities. *Talanta* **2021**, *223*, 121704.

[80] Zhou, J.; Wang, Y.; Zhang, L.; Li, X. Plasmonic biosensing based on non-noble-metal materials. *Chinese Chemical Letters* **2018**, *29*, 54–60.

[81] Samson, R.; Navale, G. R.; Dharne, M. S. Biosensors: frontiers in rapid detection of COVID-19. *3 Biotech* **2020**, *10*.

[82] Ding, X.; Su, W.; Ding, X. Methods of Endotoxin Detection. *Journal of Laboratory Automation* **2015**, *20*, 354–364.

[83] Zhou, H.; Lee, J.; Park, T. J.; Lee, S. J.; Park, J. Y.; Lee, J. Ultrasensitive DNA monitoring by Au-Fe3O4 nanocomplex. *Sensors and Actuators, B: Chemical* **2012**, *163*, 224–232.

[84] Momtazi, L.; Bagherifam, S.; Singh, G.; Hofgaard, A.; Hakkarainen, M.; Glomm, W. R.; Roos, N.; Mælandsmo, G. M.; Griffiths, G.; Nyström, B. Synthesis, characterization, and cellular uptake of magnetic nanocarriers for cancer drug delivery. *Journal of Colloid and Interface Science* **2014**, *433*, 76–85.

[85] Ridelman, Y.; Singh, G.; Popovitz-Biro, R.; Wolf, S. G.; Das, S.; Klajn, R. Metallic nanobowls by galvanic replacement reaction on heterodimeric nanoparticles. *Small* **2012**, *8*, 654–660.

[86] Bandyopadhyay, S.; Mcdonagh, B. H.; Singh, G.; Raghunathan, K.; Sandvig, A.; Sandvig, I.; Andreassen, J.-P.; Glomm, W. R. Growing gold nanostructures for shape-selective cellular uptake. *Nanoscale Research Letters* **2018**, *13*.

[87] Jimenezjimenez-Lamana, J.; Marigliano, L.; Allouche, J.; Grassl, B.; Szpunar, J.; Reynaud, S. S. A Novel Strategy for the Detection and Quantification of Nanoplastics by Single Particle Inductively Coupled Plasma Mass Spectrometry (ICP-MS). *Anal. Chem.* **2020**, *92*, 11664–11672.

[88] Wuithschick, M.; Birnbaum, A.; Witte, S.; Sztucki, M.; Vainio, U.; Pinna, N.; Rademann, K.; Emmerling, F.; Kraehnert, R.; Polte, J. Turkevich in New Robes: Key Questions Answered for the Most Common Gold Nanoparticle Synthesis. *ACS Nano* **2015**, *9*.

[89] Jana, N. R.; Gearheart, L.; Murphy, C. J. Wet Chemical Synthesis of High Aspect Ratio Cylindrical Gold Nanorods. *J. Phys. Chem. B* **2001**, *105*, 4065–4067.

[90] Lim, J.; Lee, N.-E.; Lee, E.; Yoon, S. Surface Modification of Citrate-Capped Gold Nanoparticles Using CTAB Micelles. *Notes Bull. Korean Chem. Soc* **2014**, *35*, 2567.

[91] Akash, M. S. H.; Rehman, K. *Essentials of Pharmaceutical Analysis*; Springer Singapore: Singapore, 2020.

[92] Swineharf, D. F. *The Beer-Lambert Law*.

[93] Nellist, P. D. *Scanning Transmission Electron Microscopy*; 2019.

[94] Adeyeye, A.; Shimon, G. *Growth and Characterization of Magnetic Thin Film and Nanostructures*; 2015.

[95] Sears, F. W. Faraday's Law and Ampere's Law. *American Journal of Physics* **1963**, *31*.

[96] Foner, S. Versatile and Sensitive Vibrating-Sample Magnetometer. *Review of Scientific Instruments* **1959**, *30*.

[97] Kumar, A.; Dixit, C. K. *Advances in Nanomedicine for the Delivery of Therapeutic Nucleic Acids*; Elsevier, 2017.

[98] Ravikumar, C.; Bandyopadhyaya, R. Mechanistic Study on Magnetite Nanoparticle Formation by Thermal Decomposition and Coprecipitation Routes. *J. Phys. Chem. C* **2011**, *115*, 1380–1387.

[99] Bilal, M. Synthesis and Functionalization of Gold and Iron-Gold Core Shell Nanoparticles for Biosensing Applications. *Norwegian University of Science and Technology (NTNU)* **2021**,

[100] Petcharoen, K.; Sirivat, A. Synthesis and characterization of magnetite nanoparticles via the chemical co-precipitation method. *Materials Science and Engineering: B* **2012**, *177*.

[101] Pieretti, J. C.; Rolim, W. R.; Ferreira, F. F.; Lombello, C. B.; Mô, Nascimento, H. M.; Seabra, A. B.; Nascimento, M. H. M. Synthesis, Characterization, and Cytotoxicity of Fe3O4@Ag Hybrid Nanoparticles: Promising Applications in Cancer Treatment. *Journal of Cluster Science* **2020**, *31*, 535–547.

[102] Sharma, A.; Foppen, J. W.; Banerjee, A.; Sawssen, S.; Bachhar, N.; Peddis, D.; Bandyopadhyay, S. Magnetic Nanoparticles to Unique DNA Tracers: Effect of Functionalization on Physico-chemical Properties. *Nanoscale Res Lett* **2021**, *16*, 24.

[103] Sánchez-Cabezas, S.; Montes-Robles, R.; Gallo, J.; Sancenón, F.; Martínez-Máñez, R. Combining magnetic hyperthermia and dual T1/ T2 MR imaging using highly versatile iron oxide nanoparticles. *Dalton Transactions* **2019**, *48*.

[104] Bandyopadhyay, S.; Singh, G.; Sandvig, I.; Sandvig, A.; Mathieu, R.; Anil Kumar, P.; Glomm, W. R. Synthesis and in vitro cellular interactions of superparamagnetic iron nanoparticles with a crystalline gold shell. *Applied Surface Science* **2014**, *316*.

[105] Raghunathan, K.; Antony, J.; Munir, S.; Andreassen, J.-P.; Bandyopadhyay, S. Tuning and tracking the growth of gold nanoparticles synthesized using binary surfactant mixtures †. *Nanoscale Adv.* **2020**, *2*.

[106] Scarabelli, L.; Sánchez-Iglesias, A.; Pérez-Juste, J.; Liz-Marzán, L. M. A “Tips and Tricks” Practical Guide to the Synthesis of Gold Nanorods. *The Journal of Physical Chemistry Letters* **2015**, *6*.

[107] Yamashita, S.; Kikkawa, J.; Yanagisawa, K.; Nagai, T.; Ishizuka, K.; Kimoto, K. Atomic number dependence of Z contrast in scanning transmission electron microscopy. *Scientific Reports* **2018**, *8*.

[108] Tamer, U.; Gündoğdu, Y.; Boyaci, I. H.; Pekmez, K. Synthesis of magnetic core-shell Fe3O4-Au nanoparticle for biomolecule immobilization and detection. *Journal of Nanoparticle Research* **2010**, *12*, 1187–1196.

Appendix

Fe@Au-CTAB NPs

CTAB capped core shell Fe@Au-CTAB NPs were synthesized following a modified procedure from Tamer et al[108]. Briefly, 910 μl of aqueous IO-CTAB NPs and 90 μl 1.0 M $HAuCl_4$ was added to a glass vial mixed by ultra sonication for 2 min. Next, 160 μl ice cold ($\sim$ 4°C) 0.01 M $NaBH_4$ was added, and the mixture was sonicated for another 5 min. The resulting NP solution had a dark brown-redish color. No cleaning procedure was performed, before measuring their UV-vis absorption spectra given in Figure 1.50.

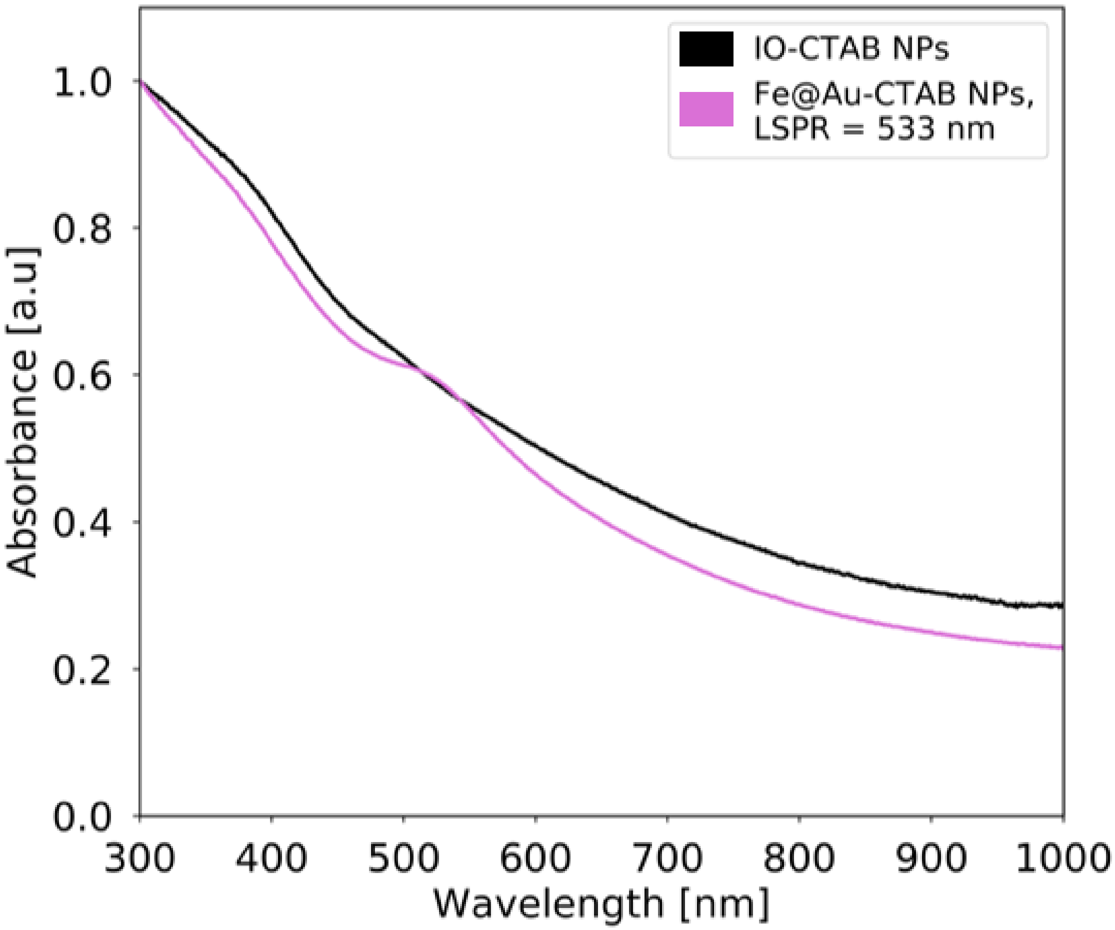

Figure 1.50: UV-vis absorbance spectra of the IO-CTAB NPs with and without Au coating.